PREDICTING BUCKLING FROM VIBRATION: AN ANALYTICAL, NUMERICAL, AND EXPERIMENTAL VERIFICATION FOR CYLINDRICAL SHELLS

Vom Fachbereich Produktionstechnik
der
UNIVERSITÄT BREMEN

zur Erlangung des Grades
Doktor-Ingenieur (Dr.-Ing.)
genehmigte

Dissertation

von
M.Sc. Felipe Franzoni
aus Nova Esperança, Brasilien

Gutachter: Prof. Dr.-Ing. Richard Degenhardt, Universität Bremen
Prof. Dr.-Ing. habil. Christian Mittelstedt, Technische Universität Darmstadt

Tag der mündlichen Prüfung: 29. Januar 2020

To Di.

“There is pleasure in recognizing old things
from a new viewpoint.”
Richard P. Feynman

Acknowledgments

I developed my doctorate in the Department of Structural Mechanics at the DLR Institute of Composite Structures and Adaptive Systems in Braunschweig, cooperating with the Faserinstitut Bremen e.V. located at the Universität Bremen. Funding was also granted by the ESA NPI program, contract No. 4000119184/17/NL/MH/GM. All the support, financial or otherwise, is gratefully acknowledged.

Like all students who dared to follow this path, I am not solely responsible for achieving such a distinctive accomplishment. Many others helped and inspired me to go further with my numerous tasks, just as many others gave me emotional support to endure the journey. Altogether, I had three productive and amusing years, and in the next paragraphs, I will externalize my gratitude to everyone involved.

Firstly, I would like to thank my Doktorvater Professor Dr.-Ing. Richard Degenhardt for accepting me as a Ph.D. student and these three years of guidance and friendship. Richard helped me continuously here in Germany, regardless of what I needed. I always felt motivated and, since day one, our working collaboration was running smoothly. I cannot thank him enough for this unique opportunity — it was an honor.

Professor Dr. Mariano Andrés Arbelo deserves special recognition. Mariano is the main person behind the methodology investigated within the scope of this thesis; besides, he also indicated to me this Ph.D. position and participated actively in technical discussions and all publications during the development of the doctoral thesis.

Dr.-Ing. Jochen Albus from ArianeGroup also deserves special recognition for sharing his unique expertise and suggesting the study that became the most prominent contribution of this doctoral thesis. The presence in the doctoral committee and the collaboration in our scientific papers are also highly appreciated.

I am grateful to all other members of the doctoral committee, Professor Dr.-Ing. Axel Siegfried Herrmann, Professor Dr.-Ing. habil. Christian Mittelstedt, Dipl.-Ing. Christoph Hoffmeister, and Mareike Wöstmann, for participating in the colloquium and providing valuable comments on my doctoral thesis.

My special thanks go to Professor Dr. Chiara Bisagni and Dr. Edgars Labans from TU Delft and Falk Odermann from DLR for performing one of the VCT test campaigns of this thesis and the collaboration in our scientific paper.

I am also grateful to all DLR staff for assistance during these years, especially to Falk Odermann, Dr.-Ing. Dirk Wilckens, and Markus Kepke for helping me with the experimental campaigns and the related publications. Our supervisor Dr.-Ing. Tobias Wille also deserves a special acknowledgment for allowing a symbiosis between this doctoral research and other buckling projects, which expanded the test program to three experimental campaigns.

During these three years, I spent one month per year at ESTEC in the Netherlands. The friendly environment of the Structures, Mechanisms, and Materials Division combined with an overview of many space projects and visits to fascinating testing facilities made of these periods the most remarkable experience related to the doctorate. My very special thanks go to Hermann Fischer and Julie Rocks, who always welcomed me there and ensured that I could participate in all activities happening at ESTEC.

Of particular help in reviewing this thesis, the following colleagues deserve my gratitude: Dirk, Gustavo, Rafael, and Rubens, and Ms. Doris Andrea Kobelt from DLR.

For the shared moments of joy that secured me some work-life balance, the following friends deserve to be mentioned: Anna, Carol, Domingos, Gustavo, Hitham, Larissa, Leonardo, Luciana, Juliana, Nazaré, Rafael, Renata, Soleane, and Thaís.

For the lasting impact they left on my life, which certainly brought me to this point, the following professors deserve to be remembered: Dr. Samuel da Silva, Dr. Geraldo Carvalho Brito Junior, Dr. Eduardo Moreira, Dr. Sérgio Frascino Müller de Almeida, and Dr. Maurício Vicente Donadon.

My deepest gratitude goes to my parents for encouraging me over the years. I am fortunate to have such a supportive family that made numerous sacrifices, always prioritizing a good education for my sister and me. I am very proud of being somehow like you both.

Finally, I would most of all like to thank my wife Diany for sharing this adventure in Germany with me. Undoubtedly, of everyone involved, she made the most considerable sacrifices. I will always be indebted to her for the support, love, and patience during these years.

Felipe Franzoni
Braunschweig, August 2019

Abstract

This thesis explores an empirical vibration correlation technique for predicting the buckling load of imperfection-sensitive cylindrical shells. As the title implies, the research addresses analytical, numerical, and experimental aspects of the mentioned methodology.

Within the scope of the analytical work, the emphasis is given to provide an analytical foundation for the referred technique. Firstly, the equations describing the free vibrations of an axially loaded cylinder are revisited through a linearized theory of shells. Subsequently, the reviewed equations are rearranged, expressing a parametric form of the applied load as a quadratic function of a parametric form of the loaded natural frequency. Afterward, the typical static behavior of an imperfection-sensitive structure is evaluated, establishing the link between the minimum magnitude of the parametric form of the applied load and the effective knockdown factor of the experiment.

Towards a numerical verification based on finite element models, two theoretical cylindrical shells are defined. At first, the critical buckling load and the fundamental natural frequency for different load levels are determined and compared to the analytical results for verifying the numerical models. The finite element models are then extended contemplating geometric nonlinearities, more realistic boundary conditions, and three magnitudes of a measured mid-surface imperfection. These numerical results are considered for analyzing the variation of the natural frequency in the surroundings of buckling and verifying the vibration correlation technique.

Finally, the applicability and the robustness of the methodology are further validated through three experimental campaigns. Five cylindrical shells, being three of them nominally equal, were tested. The test program covered different buckling test facilities, internal pressure levels, and in-plane imperfections. Besides, each specimen was tested for buckling for comparing the corresponding estimated and experimental buckling loads. The experimental work corroborates that the evaluated vibration correlation technique provides appropriate and conservative estimations for imperfection-sensitive cylindrical shells considering different design details and test conditions.

Zusammenfassung

In der vorliegenden Dissertation wird mit der Vibration Correlation Technique eine Methode verifiziert, durch deren Anwendung die Beullast einer imperfektionssensitiven Kreiszylinderschale zerstörungsfrei bestimmt werden kann. Diese Arbeit diskutiert analytische, numerische sowie experimentelle Aspekte der genannten Methode.

Im Rahmen der analytischen Betrachtungen liegt der Schwerpunkt auf der analytischen Bestätigung der genannten Technik. Zunächst werden die Gleichungen, die die freien Schwingungen eines axial belasteten Zylinders beschreiben, durch eine linearisierte Schalentheorie hergeleitet. Anschließend werden die Gleichungen neu geordnet, um eine parametrische Form der aufgebrachten Last als quadratische Funktion der Eigenfrequenz, ebenfalls parametrisch dargestellt, auszudrücken. Nachfolgend wird das typische statische Verhalten einer imperfektionssensitiven Struktur ausgewertet, um einen Zusammenhang zwischen der minimalen Größe der parametrischen Form der aufgebrachten Last und dem effektiven Knockdown-Faktor des Experiments herzustellen.

Die numerische Verifikation erfolgt anhand von Finite-Elemente-Modellen zweier zuvor definierter theoretischer Kreiszylinderschalen. Dazu werden die kritische Beullast und die erste Eigenfrequenz für verschiedene Lastniveaus bestimmt und mit den analytischen Ergebnissen zur Verifizierung der numerischen Modelle verglichen. Diese werden dann unter Berücksichtigung von geometrischen Nichtlinearitäten, realistischeren Randbedingungen und drei Werten der radialen Abweichungen der Schalenhaut von ihrer Mittelfläche weiter untersucht. Die numerischen Ergebnisse bilden eine Grundlage zur Analyse der Änderung der Eigenfrequenz in der Umgebung des Beulens und zur Überprüfung der in dieser Arbeit betrachteten Methodik.

Schließlich werden die Anwendbarkeit und die Robustheit der Methodik durch drei experimentelle Kampagnen validiert. Es werden Testergebnisse von fünf zylindrischen Schalen, von denen drei nominal gleich sind, diskutiert. Die Tests werden in unterschiedlichen Versuchseinrichtungen durchgeführt. Die experimentell ermittelte Beullast der Schalen dient als Referenz für den Vergleich mit der entsprechenden Abschätzung. Die Diskussion umfasst ferner verschiedene Innendruckniveaus und extern aufgebrachte axiale Imperfektionen in der Schalenmittelfläche. Die experimentellen Ergebnisse bestätigen, dass die diskutierte Technik realistische und konservative Abschätzungen für verschiedene Schalenkonfigurationen und Testrandbedingungen liefert.

Contents

Acknowledgments **vii**

Abstract **ix**

Zusammenfassung **xi**

Contents **xv**

List of Tables **xviii**

List of Figures **xxi**

List of Symbols **xxiii**

List of Abbreviations **xxvii**

1 Introduction **1**

2 State of the art **5**

2.1 The Southwell plot 5

2.2 VCT for columns and plates 8

2.3 VCT for imperfection-sensitive structures 11

2.4 The probing technique 16

2.5 Numerical assessment of existing VCTs 18

2.6 Summary and conclusions 20

3 Scope and outline of the thesis **23**

3.1 Scope 23

3.2 Outline of the thesis 24

4 Analytical verification **27**

4.1 Free vibration of an axially loaded cylinder 27

4.2 An analytical equation for $(1-p)^2$ 31

4.3 Experimental estimation of the KDF 32

4.4 VCT implementation 33
4.5 Summary and conclusions 34
5 Numerical assessment 37
5.1 Overview of the cylindrical shells 37
5.2 Finite element analyses 38
5.3 Analytical versus numerical results 42
5.4 Nonlinear numerical assessment 44
5.5 VCT applied to the numerical results 50
5.6 Summary and conclusions 53
6 Experimental validation 55
6.1 Overview of the cylindrical shells 55
6.1.1 Cylinder Z38 56
6.1.2 Cylinders ZD27, ZD28, and ZD29 58
6.1.3 Cylinder Z42 61
6.2 Linear numerical analyses 64
6.3 Test facilities and test set-ups 67
6.3.1 DLR static buckling test facility 67
6.3.2 DLR dynamic buckling test facility 69
6.3.3 TU Delft buckling test facility 71
6.4 Experimental campaigns 73
6.4.1 Z38 experimental campaign 73
6.4.2 DLR/TU Delft experimental campaign 75
6.4.3 Z42 experimental campaign 78
6.5 VCT applied to the experimental results 79
6.6 Summary and conclusions 83
7 Final remarks 85
7.1 Main conclusions 85

7.2 Critical assessment 87
7.3 Future works 87
Appendix A **89**
References **91**

List of Tables

5.1 Geometric characteristics of ZAL1 and ZAL2. 37
5.2 Mechanical material properties of AL7075-T7351 [107]. 38
5.3 First linear buckling loads of ZAL1 and ZAL2 considering SS4. 41
5.4 Numerical and analytical results of ZAL1 and ZAL2 considering SS3. . 43
5.5 Solver parameters for the nonlinear static analysis. 45
5.6 Nonlinear buckling loads and effective KDFs of ZAL1 and ZAL2. . . . 46
5.7 First natural frequency at the unloaded condition, P_{NL}, and P_{PB}. . . . 49
5.8 Summary of the VCT predictions of the numerical assessment. 52

6.1 Geometric characteristics of Z38 [95]. 56
6.2 Geometric characteristics of ZD27, ZD28, and ZD29 [97]. 58
6.3 Mechanical material properties of IM7/8552 [111, 112]. 59
6.4 Modified mechanical material properties of IM7/8552. 61
6.5 Geometric characteristics of Z42 [117]. 62
6.6 Mechanical material properties of 135/HS40/67g [117]. 62
6.7 Modified mechanical material properties of 135/HS40/67g. 62
6.8 First linear buckling load of the cylindrical shells. 67
6.9 Results of the buckling tests of Z38 [95]. 73
6.10 Results of the vibration tests of Z38 [95]. 74
6.11 Results of the DLR buckling tests of ZD27, ZD28, and ZD29 [97]. . . . 75
6.12 Results of the vibration tests of ZD28 and ZD29 [97]. 76
6.13 Results of the TU Delft buckling test of ZD27 [97]. 76
6.14 Results of the vibration tests of ZD27 [97]. 77
6.15 Results of the buckling tests of Z42 [117]. 78

6.16 Results of the vibration tests of Z42. 79

6.17 Summary of the VCT predictions of the experimental campaigns. 82

List of Figures

1.1 Typical load-shortening curve of a cylindrical shell. 1

1.2 Preparation of a full-scale cylinder for a buckling test [30]. 3

1.3 Cutaway view of the upcoming Ariane 6 [31]. 3

2.1 Schematic view of the Southwell plot. 6

2.2 Comparison between simply supported and clamped columns. 9

2.3 Schematic view of the characteristic chart zones, as classified in [76]. . 10

2.4 Comparison between perfect and imperfect shell structures. 12

2.5 Schematic view of the VCT established in [87]. 13

2.6 Schematic view of the VCT established in [35]. 15

2.7 Schematic diagram of the probing technique evaluated in [45]. 17

2.8 First vibration mode at different load levels for Z15U500 [46]. 18

2.9 Numerical assessment of existing VCTs. 19

4.1 Geometry of a conventional cylindrical shell. 27

4.2 Typical load-shortening curve of an unstiffened cylindrical shell. 32

4.3 Illustration of a typical VCT experiment. 33

5.1 Measured mid-surface imperfection of SST-1, available in [108]. 38

5.2 Implementation of the boundary conditions in the FE models. 39

5.3 Convergence of the first axis-symmetrical buckling load of ZAL1. . . . 40

5.4 FE meshes of ZAL1 and ZAL2. 40

5.5 Initial mid-surface imperfection applied in the FE models. 42

5.6 Natural frequencies for different magnitudes of m and n. 42

5.7 First unloaded vibration mode of ZAL1 and ZAL2 considering SS3. . . 43

5.8 First buckling mode and first unloaded vibration mode for SS3. 44

5.9 First buckling mode and first unloaded vibration mode for SS4. 45
5.10 Load-shortening curves as related to the initial imperfections. 46
5.11 Load steps followed by frequency analyses. 47
5.12 MAC index variation for the first vibration mode. 48
5.13 First vibration mode at different load levels for ZAL1M050. 49
5.14 First natural frequency variation of ZAL1 and ZAL2. 50
5.15 Convergence of the deviation for the VCT predictions. 51
5.16 VCT implementation for the numerical assessment. 52

6.1 Isometric and detailed views of Z38 with design details [95]. 56
6.2 Z38 potted into the metallic end plates [95]. 57
6.3 Measured mid-surface imperfection of Z38. 57
6.4 Specimens ZD27, ZD28, and ZD29 [97]. 58
6.5 Measured mid-surface imperfection of ZD27, ZD28, and ZD29. 59
6.6 Measured thickness variation of ZD27, ZD28, and ZD29. 60
6.7 Specimen Z42 [117]. 61
6.8 Measured thickness variation of Z42. 63
6.9 Schematic view of the upper ring. 63
6.10 Top view of the shim. 63
6.11 Implemented in-plane imperfection of Z42 [117]. 64
6.12 Measured mid-surface imperfection of Z42. 64
6.13 Convergence of the first buckling load of Z38. 65
6.14 FE mesh and cross-section area of the shell elements of Z38. 65
6.15 Convergence of the first buckling load of the CFRP cylinders. 66
6.16 FE meshes of the CFRP cylinders. 66
6.17 Z38 and Z42 positioned in the DLR static buckling test facility. 68
6.18 Schematic representation of the pressure control system [95]. 68
6.19 Grids of the measured vibration points of Z38 and Z42. 69

6.20 ZD28 positioned in the DLR dynamic buckling test facility. 70
6.21 Grids of the measured vibration points of ZD28 and ZD29. 71
6.22 ZD27 positioned in the TU Delft buckling test facility. 72
6.23 Grid of the measured vibration points of ZD27. 72
6.24 First vibration mode at the first load step for Z38. 74
6.25 First vibration mode at the first load step for ZD28 and ZD29. 75
6.26 First vibration mode at 5 and 6 kN for ZD27. 77
6.27 First vibration mode at the first load step for Z42. 79
6.28 VCT implementation for the experimental campaigns. 81

List of Symbols

A	Fitting coefficient
A_{mn}	Amplitude coefficient associated with u
B	Fitting coefficient
B_{mn}	Amplitude coefficient associated with v
b	Distance between stiffeners
C	Fitting coefficient
C_{mn}	Amplitude coefficient associated with w
C_{N}	Constant of Equation (4.2)
D_{T}	Prescribed transverse displacement
E	Elastic modulus
E_{11}	Elastic modulus in the longitudinal direction
E_{22}	Elastic modulus in the transverse direction
F_1	First unloaded natural frequency (in Hz)
F_{IN}	Inertial force
F_{mn}	Natural frequency (in Hz)
$\bar{F}_1$	First loaded natural frequency (in Hz)
f	Frequency ratio
G_{12}	Shear modulus in the 1-2 plane
G_{13}	Shear modulus in the 1-3 plane
G_{23}	Shear modulus in the 2-3 plane
G_m	Constant of Equation (4.26)
H_{ij}	Variables of Equation (4.11), where i and j are equal to 1, 2, and 3
H_{ST}	Height of the stiffener
h	Thickness of the cylinder
h_{NOM}	Nominal thickness of the laminate
h_{ST}	Thickness of the stiffener

k	Constant of Equation (4.2)
L	Axial length of the cylinder
$[L]$	Matrix differential operator
$[L_{\mathrm{D}}]$	Terms of $[L]$ associated with Donnell's shell theory
$[L_{\mathrm{F}}]$	Terms of $[L]$ extending Donnell's to Flügge-Lurie[1]-Byrne's shell theory
$[L_{\mathrm{I}}]$	Terms of $[L]$ associated with the initial stress state
M_x	Moment resultant at x-direction
m	Number of axial half-waves
N_x	Stress resultant at x-direction
$\bar{N}_x$	Uniform axial membrane force
n	Number of circumferential waves
P	Axially applied load
P_{CR}	Theoretical buckling load
P_{D}	Design buckling load
P_{EXP}	Experimental buckling load
P_i	Stepwise axially applied load
P_{MAX}	Maximum load level considered in the VCT estimation
P_{NL}	Nonlinear buckling load
P_{PB}	First stable increment in the postbuckling regime
P_{PROB}	Probing technique estimated buckling load
P_{T}	Transverse reaction load
$P_{\mathrm{T,MAX}}$	Maximum transverse reaction load
P_{VCT}	VCT estimated buckling load
p	Axially applied load ratio
p_{INT}	Level of internal pressure
q	Frequency exponent
q_{OPT}	Optimal frequency exponent

---

[1] Anatolii Isakovich Lurie (★ 1901–✝ 1980), in Russian: Анато́лий Исаа́кович Лурье́, was an outstanding Russian professor in the field of solid mechanics. The reader may find the transcription of his last name as Lurye, Lur'ye, Lur'e, or Luré.

R	Middle surface radius of the cylinder
R_{S}^2	Coefficient of determination
T_i	Coefficients of Equation (4.19), where i is equal to 0, 1, and 2
t	Time variable
u	Displacement of the middle surface in the axial direction
u_{a}	Axial shortening
u_i	Displacement vector defined by $\{u \;\; v \;\; w\}^{\mathrm{T}}$
v	Displacement of the middle surface in the circumferential direction
W	Maximum lateral deflection
W_0	Initial maximum lateral deflection
w	Displacement of the middle surface in the radial direction
X_{C}	Given material property of the composite material
$X_{\mathrm{C,NOM}}$	Nominal magnitude of a given material property of the composite material
X_{M}	Given material property of the matrix
x	Axial coordinate
z	Radial coordinate

Greek letters

α	Slope of the classic Southwell plot
γ	NASA's knockdown factor
γ_{EXP}	Effective knockdown factor of the experimental buckling load
γ_{NL}	Effective knockdown factor of the nonlinear buckling load
δ_{ANA}	Deviation between numerical and analytical results
δ_{CR}	Deviation between the first and n^{th} buckling loads
δ_{DLR}	Deviation between DLR and TU Delft test results
δ_{EXP}	Deviation of the VCT prediction for the experimental results
δ_{NL}	Deviation of the VCT prediction for the numerical results
θ	Circumferential coordinate

λ_m	Variable in the assumed displacement components
$\bar{\lambda}_m$	Represents the variable λ_m multiplied by R
ν	Poisson's ratio
ν_{12}	Poisson's ratio of the unidirectional lamina
ξ^2	Square of the drop of the loading-carrying capacity
ρ	Mass density
$\bar{\Omega}_{mn}$	Frequency parameter
ω_{mn}	Natural frequency (in rad/s)
$\bar{\omega}_{mn}$	Loaded natural frequency (in rad/s)

List of Abbreviations

CFRP	Carbon fiber-reinforced polymer
DIC	Digital image correlation
ESA	European Space Agency
FE	Finite element
KDF	Knockdown factor
MAC	Modal assurance criterion
NASA	National Aeronautics and Space Administration
VCT	Vibration correlation technique

1 Introduction

The “perplexing” behavior of thin-walled cylindrical shells under axial compression has driven a considerable effort in many fields of applied mechanics since the beginning of the 20th century [1]. From the first formulations [2–4], the scientists noticed that the inherent imperfections of the specimens could lead to a high discrepancy between the theoretical buckling load P_{CR}, calculated for the perfect cylinder, and the experimental buckling load P_{EXP}, as illustrated in Figure 1.1.

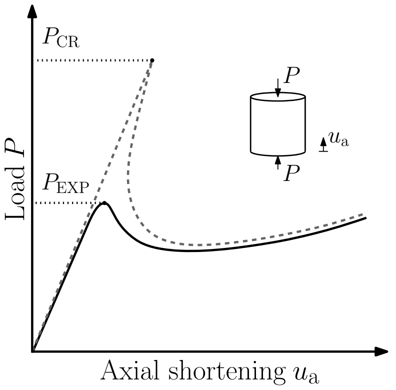

Figure 1.1: Typical load-shortening curve of a cylindrical shell.

Different shell theories were proposed accounting for the initial imperfections, for example, see [5, 6]. However, the first appropriate one, representing the imperfection-sensitive behavior from the experiments, was developed by Koiter in his pioneering doctoral thesis [7]. In summary, Koiter’s general theory of stability proposes an asymptotic formula for the initial postbuckling predictions of elastic systems under conservative loading being accurate enough only for sufficiently small imperfections amplitudes [8].

At the same time, a reliable methodology was needed for sizing cylindrical shell structures taking into account the imperfection-sensitive aspect [9]. Nevertheless, there were limitations for measuring and representing the effects of the initial imperfections into the developed shell theories leading to “dramatic disagreements” [10]. Koiter [11] summarized that, in the period between the beginning of the 20th century and the 1970s, “the buckling theory and experiments have not co-existed in harmony”.

In this scenario, the empirical lower-bound method based on extensive experimental campaigns, known as NASA SP-8007 [12], was consolidated as the main reference for sizing imperfection-sensitive cylindrical shells during the 1960s. This guideline expresses the design buckling load P_D as γP_CR, where γ is the knockdown factor (KDF) covering the worst-case scenario of the load-bearing capacity. For an isotropic unstiffened cylinder, it is calculated as [12]:

$$\gamma = 1 - 0.901\left[1 - \exp\left(-\frac{1}{16}\sqrt{\frac{R}{h}}\right)\right] \tag{1.1}$$

where R and h are the middle surface radius and the thickness of the isotropic unstiffened cylindrical shell, respectively. This lower-bound approach provided successful shell designs for several generations of aerospace projects [9] being intensively employed up to the present (2019).

Nowadays, the consensus is that the NASA guideline [12] is overly conservative for most of the well-constructed cylindrical shells [13]. Consequently, there is a worldwide effort for the development of novel approaches exploring the current status of computing capabilities and experimental techniques, for instance, see [14−19]. The energy barrier against buckling, as introduced in [20, 21] and recapitulated in [22], is gaining more attention being explored for the same purpose in [13, 23−26].

Nevertheless, even considering the present computing capabilities and the effectiveness of the mentioned methodologies, the reasons for performing a buckling test in the computational era enumerated by Singer [27] in the 1980s are still coherent. This is true, especially for certification tests of full-scale shell structures, where the final design, including complicated stiffening and load diffusion elements, is verified, providing a better understanding of the buckling behavior and the primary factors affecting it [28].

As an example of the relevance of such experiments, the ongoing NASA's Shell Buckling Knockdown Factor project is performing buckling tests of real-scale specimens. The project intends to investigate the effects of the scale on the buckling of large launch vehicle barrel components and to correlate the data obtained from sub-scale test specimens to full-scale ones [29]. Figure 1.2 shows the preparation of a full-scale cylindrical shell for one of the buckling tests performed in the course of the referred project [30].

Noticeably, thin-walled cylindrical shells dominate the design of launch vehicles. Figure 1.3 presents a cutaway view of the upcoming Ariane 6 developed and manufactured by ArianeGroup under the authority of ESA, in which the shell-dominant design is illustrated [31]. In such applications, the operational load envelope, combined with the simultaneous lightweight and high-performance requirements, recurrently leads to a buckling-critical shell design [9].

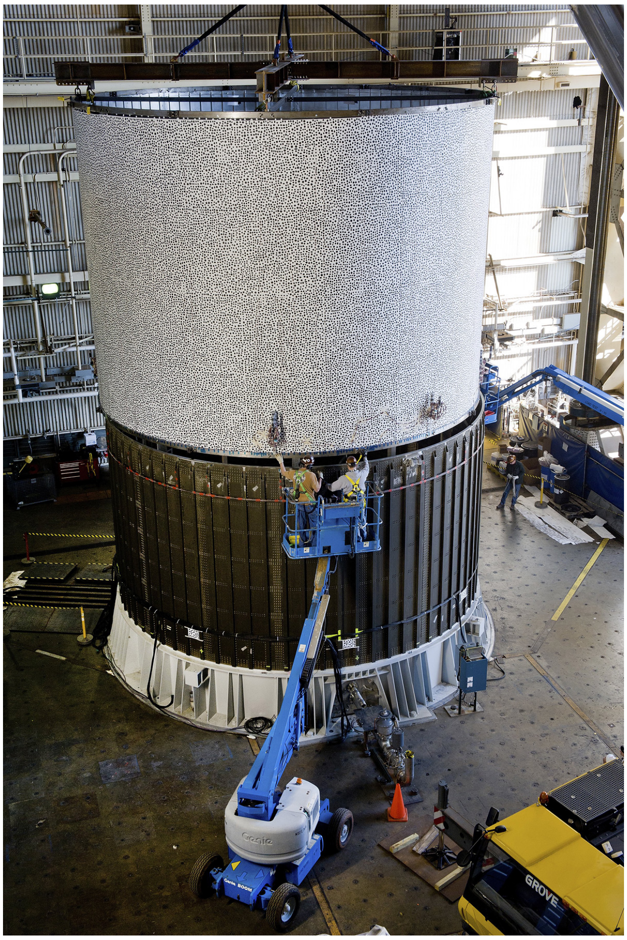

Figure 1.2: Preparation of a full-scale cylinder for a buckling test [30].

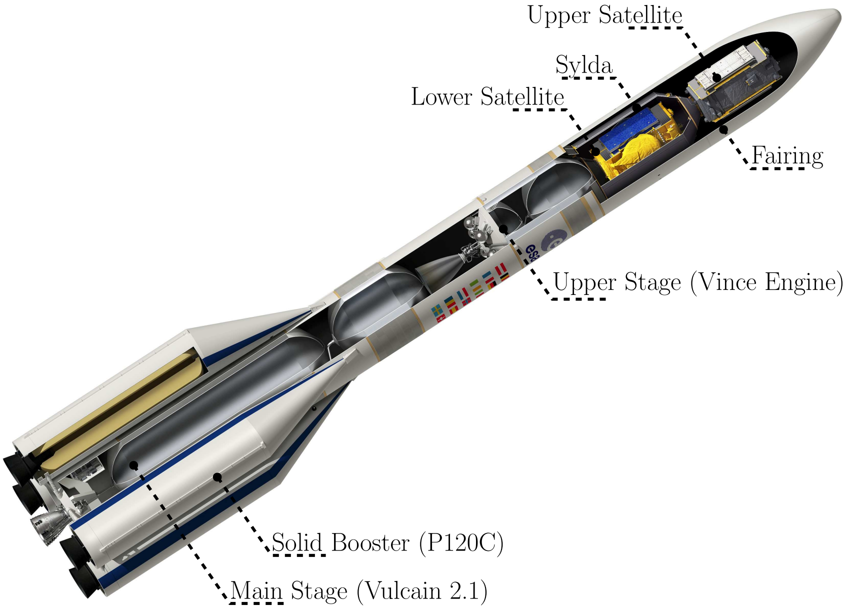
Upper Satellite
Sylda
Lower Satellite
Fairing
Upper Stage (Vince Engine)
Solid Booster (P120C)
Main Stage (Vulcain 2.1)

Figure 1.3: Cutaway view of the upcoming Ariane 6 [31].

Considering the destructive or terminal nature of the buckling experiment [32], including also the long production and test preparation cycles of barrel components, a specimen exclusively allocated to the static qualification test is required. Hence, there are inherent financial and time-consuming interests in the development and validation of nondestructive methods to obtain the *in-situ* buckling load from the prebuckling stage, permitting the use of the same specimen in another qualification test.

Typically, these methods consist of tracking the response of the structure at different axially applied load levels for extrapolating the instability point from the measured data. A consolidated methodology is the Southwell plot [33]; however, for structures exhibiting a complex buckling behavior, like curved panels and cylindrical shells, alternative approaches are preferable as the vibration correlation technique (VCT) [32] and the lately published probing technique [34].

In this thesis, the focus will be given to the VCT applied to cylindrical shells. Firstly, the research will present analytical support, based on a linearized theory of shells, for an empirical methodology addressing such structures [35]. Afterward, a numerical assessment of two theoretical isotropic cylinders will take geometric nonlinearities and more realistic boundary conditions into account; besides, this assessment also lays the foundation for a systematic approach for defining a VCT experiment.

Furthermore, the *status quo* of the applicability and robustness of the mentioned technique will be further validated through three experimental campaigns. The experiments, conducted utilizing state-of-the-art techniques, considered five specimens and three buckling test facilities. The analytical, numerical, and experimental results will be employed to verify the VCT as a reliable nondestructive experimental procedure for estimating the buckling load of imperfection-sensitive cylindrical shells.

2 State of the art

During the first half of the past century, several researchers were addressing the “apparently different” problems of vibration and elastic stability simultaneously [36–39]. Many investigations studied both phenomena for understanding the effects on the vibration response triggered by the local or global instabilities, as revisited in [32, 40–42]. In this chapter, an overview of a relevant part of this literature, dedicated to estimating the buckling load from the vibration measurements, is provided.

Nondestructive experimental procedures for estimating the buckling load from the prebuckling stage are under development from the 1930s until the present. Over the years, different techniques were proposed built on indirect measurements as, e.g., the Southwell plot established on the static response [33], the VCT based on the vibration response [32, 39], and the probing technique [34, 43], which experimentally quantifies the landscape of the energy barrier against buckling [21, 22].

The review starts with a brief discussion of the Southwell plot [33] in Section 2.1. After that, focusing on the VCT, Section 2.2 gives historical background and the recent developments on columns and plates. Subsequently, Section 2.3 revisits the state-of-the-art techniques concerning imperfection-sensitive structures. Although part of the VCTs assesses the actual boundary conditions for improving an initial model [32, 44], this review contemplates the direct methods, as classified in [32].

Section 2.4 sums up the probing technique, which was formulated recently in [34, 43] and verified numerically in [45]. Closing the chapter, Section 2.5 explores the main results of the work published in [46]. The recapitulated study consists of a numerical assessment of three existing VCTs based on ten unstiffened composite laminated cylinders tested for buckling in [15]. In this section, the emphasis is given on the dynamic behavior in the surroundings of buckling and the applicability of the evaluated VCTs.

2.1 The Southwell plot

The Southwell plot is a nondestructive method for predicting the buckling load based on measurements of the lateral deflection of the structure. The original methodology establishes that the inverse slope of the plot W/P versus W, where W is the maximum deflection, yields the buckling load expressed as $P_{\mathrm{CR}} = \cot\alpha$. The derivation of the method and most of its extensions are available in [28]; additionally, Figure 2.1 illustrates the simplest form of the Southwell plot, where W_0 is the initial deflection.

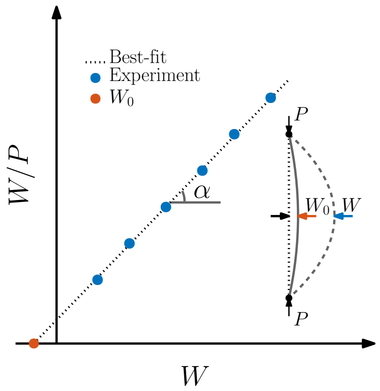

Figure 2.1: Schematic view of the Southwell plot.

The practicality of the method was promptly verified by Southwell considering the columns tested in [47] substantiating since then its effectiveness as a nondestructive experimental procedure to predict the buckling load of real structural components [28, 48]. For instance, Fisher [49] experimentally validated the technique for solid rectangular spars under combined axial and transverse loading, which is typically found in aeronautical applications.

Ramberg et al. [50] experimentally investigated axially loaded stiffened panels obtaining good results for the stringers attached to the panels regardless of their failure mode. Donnell [48] considerably extended the Southwell plot addressing columns on an elastic foundation and a flat panel with one free edge and three hinged edges (including the two loaded ones); moreover, the author demonstrated that the method is valid for any n^{th} theoretical buckling load.

Lundquist [51] proposed a generalized form of the Southwell plot based on incremental deflections due to incremental loads, in which the main issue of the original work, i.e., measuring the initial deflection W_0, was overcome. A small initial curvature causes the deflections to remain relatively small with the load; therefore, another important extension was made in [52], where the author derived the equations considering an intentional eccentricity to compensate for the initial curvatures.

In 1989, Singer [53] readdressed the extended Southwell plot for inelastic buckling available in [54]. The author recapitulated the experimental results and the errors of the new predictions were below 9%. Concerning lateral-torsional buckling of columns, Stratford et al. [55, 56] suggested that a modified form of the Southwell plot was needed. Nevertheless, Mandal and Calladine [57] demonstrated that the classic form is appropriate, being the modified method suitable only for unrealistic cases.

Concerning plates, Donnell confirmed in [48] that the Southwell plot could not be exactly applied because of the nonlinear extensional strains. Analyzing the demonstrated equations, also available in [28], the method is applicable only if the deflections are considerably smaller when compared to the thickness of the plate, or if the bent surface is a developable surface as obtained for a plate simply supported on three borders (including the two loaded ones) and free on the fourth [48].

During the 1960s and 1970s, several authors extensively investigated the applicability of the Southwell plot, *vide* [58–62]. Walker [58] performed theoretical and experimental investigations considering eccentrically loaded plates and thin-walled sections validating the method successfully. Horton et al. [59] broadly reviewed the application for columns and plates, concluding that the methodology should be valid for plates with deflections less than one-half of its thickness.

Datta and Carlson [60] achieved a good correlation for rectangular aluminum plates with aspect ratio 0.2 and 0.4; however, for specimens with aspect ratio 0.6 and 0.8, the deviations were around 15%. Spencer and Walker [61] validated a variation of the method based on a defined pivotal point obtaining straight-line plots for examples that the Southwell plot had exhibited nonlinear curves. Likewise, Datta [62] successfully tested a rectangular plate under partial edge loading and mixed boundary conditions.

The suitability of the method was also broadly explored considering stiffened cylindrical and conical shells. For example, several experimental campaigns were conducted at Technion during the 1960s and at the beginning of the 1970s [63, 64], where the slope and the intercept methods, as applied for spherical shells in [65], were used. The results endorsed that the method is more appropriate for structures whose postbuckling behavior is not far from the neutral stability [32].

Craig and Duggan [66] introduced a stiffness criterion, which is equivalent to the Southwell plot, for evaluating unstiffened cylindrical shells. The authors combined the axially applied load with lateral forces applied perpendicularly to the surface of the specimen. This procedure triggered the effects of initial imperfections at lower load levels improving the estimations, for which the errors were below 1% for an axial load level equal to 76% of the actual buckling load.

Among other specimens, Horton et al. [67] also investigated unstiffened circular and elliptic cylindrical shells obtaining reliable estimations through the stiffness criterion as the deviations were 1.1% and -3.0%, respectively. In recent years, the Southwell plot and its derivatives are still being explored for determining the buckling load of shell-like structures; for example, Ghazijahani and Zirakian [68] evaluated ten conical shell structures obtaining reliable estimations.

2.2 VCT for columns and plates

The concept of relating the axially applied load to natural frequencies for identifying the buckling load, to the best of the author's knowledge, appeared at the beginning of the 20th century being accredited to Sommerfeld [36]. In this experimental work, the author verified that the first natural frequency of a clamped-free column with a variable mass at the free end decreases approaching zero as the mass was increased up to the amount required to buckle the structure.

In the following decades, the analytical formulation between the applied load and the squared natural frequency was established for several structures. Among others, the work developed by Massonnet [37, 38] is considered the foundation of the VCT [32]. The author demonstrated that the linear relationship between the applied load and the squared loaded natural frequency holds for simply supported beams, plates, and cylindrical shells, for which the vibration and buckling modes are identical [32]:

$$f^2 + p = 1 \tag{2.1}$$

where $f = \bar{\omega}_{mn}/\omega_{mn}$, being $\bar{\omega}_{mn}$ the loaded natural frequency and ω_{mn} the unloaded natural frequency, both associated with the same vibration mode specified by m axial half-waves and n circumferential waves (for cylindrical shells), and $p = P/P_{\mathrm{CR}}$, being P the axially applied load.

In the early 1950s, the above-defined equation was considered at the California Institute of Technology for direct estimations of the buckling load, establishing the classic VCT [39, 69–71]. The technique consists of plotting the experimental data in the classic characteristic chart, i.e., f^2 versus p, and adjusting a linear best-fit relationship. Afterward, from this relationship, the buckling load is extrapolated as the load level where the loaded natural frequency is equal to zero.

The described procedure is straightforward for evaluating column structures. In such applications, when considering different boundary conditions, the first vibration modes are still similar to the corresponding buckling modes. As a consequence, the relationship between f^2 and p becomes a shallow curve that slightly deviates from the linearity, like illustrated in Figure 2.2, allowing the VCT based on the linear best fit to be successfully applied for different boundary conditions [72].

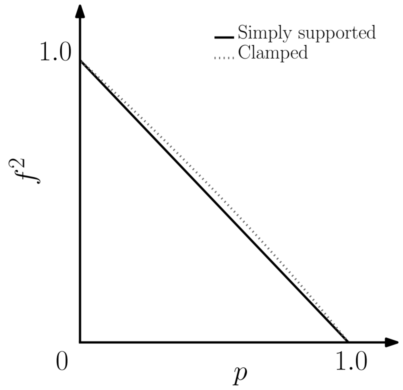

Figure 2.2: Comparison between simply supported and clamped columns.

Lurie investigated in his doctoral thesis [39] elastically restrained columns in the form of rigid-joint frames (also published in [71]). The experimental results corroborated the estimation based on the linear relationship between f^2 and p when two conditions are kept: (1) the column member of the frame must be long enough for ensuring an elastic buckling phenomenon, and (2) the boundary conditions should not change with the axial loading.

Johnson and Goldhammer [73] performed VCT experiments for predicting the buckling load of a panel-column, in fact a built-up long stiffened panel supported only on the top and bottom edges. Within this study, the classic VCT was employed for investigating the influence of different stiffener configurations on the effective length of the panel. The authors proved the applicability of the methodology and recommended it for measuring the *in-situ* effective length of panels.

Burgreen [74] studied the effect of arbitrary boundary conditions in columns. The author reconfirmed that the error on assuming a linear relationship between the squared frequency and the axially applied load is negligible (less than 2% for equal end-fixities). In the 1960s, the VCT became an accepted practice in the industry for determining the buckling load and end-fixity coefficients of columns [32], e.g., Jacobson and Wenner [75] described the procedures adopted in the Northrop Corporation.

Chailleux et al. [76] tested composite and sandwich columns with rectangular cross-sections and various boundary conditions. The specimens were designed with a span-to-depth ratio of approximately 100 and were made of epoxy resin reinforced by boron and glass fibers or aluminum reinforced by boron fibers. The authors split the characteristic chart into three zones and correlated the size of these zones with the applicability of the VCT. Figure 2.3 illustrates the described procedure [76].

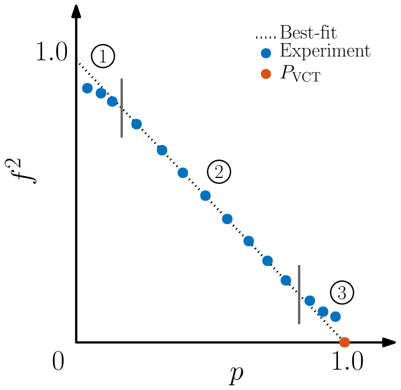

Figure 2.3: Schematic view of the characteristic chart zones, as classified in [76].

In Figure 2.3, zone 1 is the region where the clearances have not entirely disappeared; zone 2 is the region characterized by the linear relationship, for which the VCT is applicable; and zone 3 is the region where the nonlinear effects dominate causing unsymmetrical vibrations. The authors correlated the accuracy of the VCT with the size of zone 2, recommending that this zone should extend for about three-quarters of the characteristic chart for good predictions of the buckling load.

As stated before, the linear relationship between f^2 and p is available for simply supported flat plates; however, its applicability for predicting the buckling load of such structures is not straightforward. As an example, in the discussed doctoral thesis [39], the author investigated flat plates with simply supported boundary conditions. In this study, the inherent initial curvatures of the specimens led the relationship to deviate from linearity resulting in poor estimations of the buckling load.

In the 1970s, Chailleux et al. [76] also tested flat plates made of aluminum reinforced with boron fibers considering several boundary conditions. The specimens were manufactured with small imperfections permitting a good correlation between the buckling loads estimated using the VCT and the calculated ones. Moreover, the practicality of the method was correlated to the size of the linear zone of the characteristic chart, and the same criterion defined for columns, see Figure 2.3, was verified for flat plates.

Jubb et al. [77] tested square box-columns (1.225 m x 305 mm); the specimens consist of four rectangular (1.225 m x 305 mm) thick (4.8 mm) plates made of mild steel welded together along their long edges. The authors monitored the first four natural frequencies and all of them decrease as the axial load was applied. However, only the fourth natural frequency, for which the associated vibration mode is similar to the first buckling mode of the box-column, tends to zero as the axial load approaches the buckling load.

Mandal [78] studied simply supported plates with different aspect ratios. The author demonstrated that the first vibration mode changes its shape resembling the buckling mode when P approaches P_{CR}. Hence, following its frequency yields a convex curve to the origin bounded by a coherent number of straight lines, i.e., two and three lines for aspect ratios 2 and 3, respectively. The author concluded that the prediction is non-conservative for low magnitudes of P and almost exact as P tends to P_{CR}.

Chaves-Vargas et al. [79] conducted experimental and numerical investigations for flat stiffened carbon fiber-reinforced polymer (CFRP) plates. The study is based on three identical specimens with a total length of 550 mm, a total width of 430 mm, and stiffened by two blade stringers and two blade caps as inner and outer stiffeners, respectively. The authors predicted the buckling loads through the classic VCT with deviations to the experimental buckling loads between 5% and 6%.

The accuracy of the VCT to predict the shear buckling load of simply supported unstiffened and stiffened plates was numerically evaluated in [80]. The authors verified that the first vibration mode presents a smooth transition to the critical buckling mode as the shear load was increased. Besides, the relationship between f^2 and p is nonlinear being in this study represented by high-order polynomials. The adjusted curves extrapolated to f^2 equal to zero led to appropriate estimations for low load levels.

Shahgholian-Ghahfarokhi et al. [81] applied the method from [35] — described in the next section — to composite sandwich plates with isogrid cores. The authors manufactured four specimens and tested all of them for buckling and one of them for VCT. In this study, load levels up to 96% of the average experimental buckling load were considered; however, the best prediction, which is associated with a deviation of -1.5%, was achieved for a maximum load level of 87% of the average buckling load.

2.3 VCT for imperfection-sensitive structures

Imperfection-sensitive structures like curved panels and spherical and cylindrical shells present an unstable buckling behavior. For such structures, when following the vibration mode similar to the buckling mode, the relationship between f^2 and p for the imperfect structure is characterized by a sharp bend close to the buckling load, as illustrated in Figure 2.4. Therefore, the linear VCT is not applicable, and there is no consensus on a mature technique suitable for practical scenarios up to the present [82].

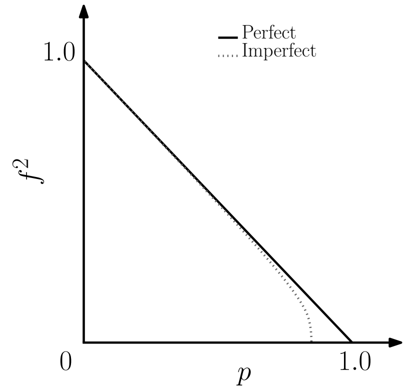

Figure 2.4: Comparison between perfect and imperfect shell structures.

In this context, different VCTs were proposed specifically addressing such structures over the years. Okubo and Whittier [83] tested six nominally identical shallow spherical shells under static external pneumatic pressure. The authors tracked the vibration mode similar to the fundamental buckling mode. The study showed that extrapolating the nonlinear relationship between f^2 and p to the abscissa would lead to appropriate estimations of the buckling load.

Radhakrishnan [84] presented an experimental campaign for cylindrical shells with an R/h of roughly 400 made of Hostaphan® under axial compression, external pressure, or both. In this study, the final linear path of the f^2 versus p chart for the vibration mode similar to the experimental buckling mode (verified through quasi-static experiments) is extrapolated to the applied load axis for estimating the buckling load. The results substantiated the suggested technique as the deviations were below 1%.

Particularly for stiffened cylindrical shells, the natural frequency and the buckling load are similarly affected by the boundary conditions when the corresponding vibration and buckling modes are close in shape [32]. Moreover, these structures are usually characterized by unique buckling modes. Thus, a multitude of experimental campaigns was performed at Technion in the 1970s, investigating the correlation between the two phenomena for assessing the boundary conditions nondestructively [27, 44].

Concerning the classic characteristic chart, such structures typically present a sharp bend close to the buckling load, *vide* Figure 2.4. Since the first attempts of applying the VCT for direct estimations, the researchers noticed that the methodology is essentially a curve fitting of the experimental data. Therefore, a convenient form for rewriting

Equation (2.1) was proposed at Technion, in which the frequency ratio f is raised to an exponent q resulting in a linear relationship to the load ratio p [32]:

$$f^q = A - Bp \tag{2.2}$$

where A and B are fitting constants and q, adjusted to its optimal magnitude q_{OPT}, leads the extrapolated load level to match exactly the experimental buckling load.

Exploring Equation (2.2), Segal [85] performed a parametric study taking into account the results of 35 stiffened cylinders. For each cylindrical shell, the author calculated q_{OPT} and investigated the influence of the dominant geometric characteristics on it. The study proposed an equation for q_{OPT} in terms of such characteristics obtaining a substantial reduction in the scatter of the VCT estimated KDF when compared to the indirect VCT method based on Equation (2.1) [32].

Plaut and Virgin [86] further explored Equation (2.2) through an analytical model of a shallow elastic arch with pinned ends. The authors verified that the pattern of the curve relating the frequency ratio f to the load ratio p changes from concave to convex as q increases. From this observation, a methodology was recommended for determining upper and lower bounds for the optimal exponent q_{OPT} and, consequently, for the estimated buckling load P_{VCT}.

Souza et al. [87] scrutinized a simplified model for large deflections representative of structures characterized by unstable instability like skin-dominated stiffened cylindrical shells. The authors defined a semi-analytical approach based on a modified characteristic chart in terms of the parametric forms $(1-p)^2$ and $1-f^4$. In such a representation, a linear relationship between these variables should be obtained, as illustrated in Figure 2.5, which presents a schematic view of the VCT delineated in [87].

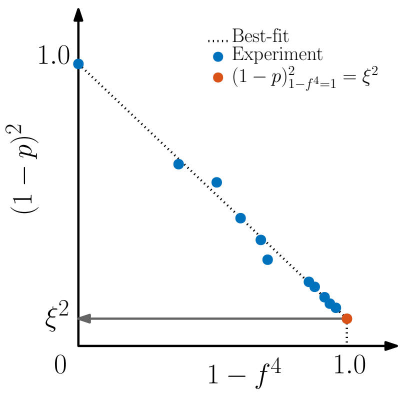

Figure 2.5: Schematic view of the VCT established in [87].

The referred linear relationship is identified through a best-fit procedure of the experimental results. Note that the parametric form $(1-p)^2$ contains the ratio between the load level and the linear buckling load; consequently, the load level in which the structure is unstable is obtained by evaluating the linear equation for the loaded natural frequency equal to zero (equivalent to the parametric form $1-f^4$ equal to one) leading to the following relationship:

$$(1-p)^2 + (1-\xi^2)(1-f^4) = 1 \tag{2.3}$$

where ξ^2 is the square of the drop of the buckling load due to initial imperfections.

Accordingly, the VCT estimation of the buckling load P_{VCT} is expressed in terms of the positive square root of ξ^2:

$$P_{\mathrm{VCT}} = P_{\mathrm{CR}}(1-\xi) \tag{2.4}$$

being $1-\xi$ comparable to the KDF γ as defined in [12].

Souza and Assaid [88] represented the classic characteristic chart through a cubic parametric curve. The authors employed the Hermite form to define the parametric equations. In this technique, the appropriate natural frequency should be measured at the unloaded condition and considering a small amount of axial load (15% of P_{CR}). Both methods established by Souza and his colleagues [87, 88] were validated based on the experimental results of stiffened cylindrical shells tested at Technion in [89].

Abramovich et al. [82] proposed a second-order equation to represent the classic characteristic chart. The authors tested aluminum and composite laminated stringer stiffened curved panels confirming that the predictions of the experimental buckling load using the VCT for load levels up to 50% of P_{CR} were reasonable. However, for improving the accuracy of the VCT estimation, load levels near the sharp bend of the characteristic chart, *vide* Figure 2.4, should be included.

In 2014, Arbelo et al. [35] established an empirical VCT addressing unstiffened composite laminated cylindrical shells. The authors modified the work done in [87] by assuming the applied load in the parametric form $(1-p)^2$ as a quadratic function of the loaded natural frequency represented as $1-f^2$. Such a second-order equation is adjusted through a best-fit procedure, from which ξ^2 is extrapolated as its minimum. Figure 2.6 presents a schematic view of the described VCT [35].

The authors estimated the buckling load from the positive value of ξ as stipulated in [87] and previously shown in Equation (2.4). Furthermore, this method is grounded on the effects of the initial imperfections in the vibration response of the structure, and typically the first two or three natural frequencies are evaluated for estimating the buckling load [90]. Until this point, this methodology was validated by different scientists in nine experimental campaigns published in [81, 90–97].

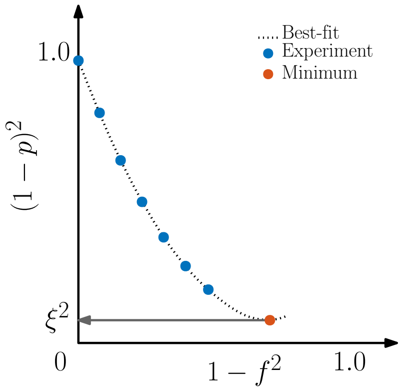

Figure 2.6: Schematic view of the VCT established in [35].

The above-described method was first time experimentally validated in [91], where three nominally identical CFRP unstiffened cylindrical shells, named R07, R08, and R09, were tested. The variation of the first natural frequency was measured for several load steps up to 80.0%, 92.2%, and 93.9% of the corresponding buckling loads for R07, R08, and R09, respectively. The predictions were in good agreement with the experimental buckling loads as the absolute errors were between 2.3% and 7.0%.

Kalnins et al. [90] conducted experiments for two CFRP and two metallic unstiffened cylindrical shells named R15, Z37, SST-1, and SST-2, respectively. The first two natural frequencies for load levels up to the onset of buckling were measured and used for the VCT predictions. The estimations coming from the first natural frequency for R15, Z37, and SST-1 and from the second natural frequency for SST-2 were associated with a deviation from the respective experimental buckling loads between 0% and 10%.

Skukis et al. [92] performed a statistical evaluation of the buckling load estimated through the VCT established in [35]. The authors investigated two identical CFRP unstiffened cylindrical shells for the VCT and obtained estimations with a deviation from the respective experimental buckling loads between 4.8% and 8.4%. Additionally, they concluded that using load levels up to 65% of the experimental buckling load gives a fidelity close to 90% in the VCT estimations.

Skukis et al. [93] executed an experimental campaign for unstiffened cylindrical shells made of aluminum with and without circular cutouts. For specimens governed by a global failure mode—cylinders without cutout and with reinforced cutout—the authors obtained reliable estimations when load levels greater than 60% of the experimental buckling load were considered. Conversely, they conclude that the VCT from [35] was not applicable when a local failure mode governs.

Recently, Shahgholian-Ghahfarokhi and Rahimi [94] further validated the aforementioned method addressing composite cylindrical shells stiffened with lozenge grid-cores. Three specimens were tested for buckling, and the VCT was applied to one of them. The authors included load levels up to 90% of the average experimental buckling load, for which the deviation was 3.1%; moreover, appropriate estimations were obtained for load levels above 68% of the average experimental buckling load.

Labans et al. [96] investigated classical and variable angle tow composite cylindrical shells. The authors measured the first four vibration modes, being the most accurate predictions based on the lowest natural frequency. For the classical laminated shell, considering load levels up to 65.48% of the theoretical buckling load led to an error of 4.0%; likewise, for the variable angle tow cylinder, considering load levels up to 69.23% of the theoretical buckling load led to an error of 1.4%.

2.4 The probing technique

As explored today, the energy barrier that must be overcome for the shell to snap through to a postbuckling path was introduced in [20, 21]. For example, the authors compared calculated and experimental results for an axially loaded cylinder disturbed by a local transverse force in [21]. The comparison indicated satisfactory quantitative and qualitative agreement for the energy barrier parameter. Since the 1970s, Evkin continues to develop the topic, and more applications are found in [26, 98–102].

Horák et al. [22] further extended the energy barrier parameter by demonstrating numerically the existence of a mountain pass point in the form of ‘‘the most localized solution that is possible—a single dimple’’. Recently, Thompson et al. [34] scrutinized these results and formulated a new nondestructive experimental procedure for estimating the buckling load, which is based on applying a lateral displacement to determine the shock sensitivity of an axially loaded cylinder.

Figure 2.7 exemplifies the probing technique following the schematic flowchart outlined in [45]. Consider a cylinder under an axial load P_i, in which a transverse displacement D_{T} is prescribed through a rigid probe. During this event, P_i is almost constant while the reaction load P_{T} varies, as illustrated in the chart emphasized by □ in Figure 2.7. The transverse load increases reaching the maximum magnitude $P_{\mathrm{T,MAX}}$, and then decreases to the initial level when simultaneously the cylindrical shell buckles.

The energy calculated through this transverse force consists of a "barrier" to be overcome for triggering the buckling of the cylinder. If the axial load level P_i is increased, the maximum transverse load $P_{\mathrm{T,MAX}}$ and the barrier required to buckle the specimen are smaller, as illustrated in the stability landscape highlighted by □ in Figure 2.7. Extrapolating this behavior, the prescribed axial load associated with $P_{\mathrm{T,MAX}}$ reaching zero would buckle the cylindrical shell without any energy barrier to be overcome.

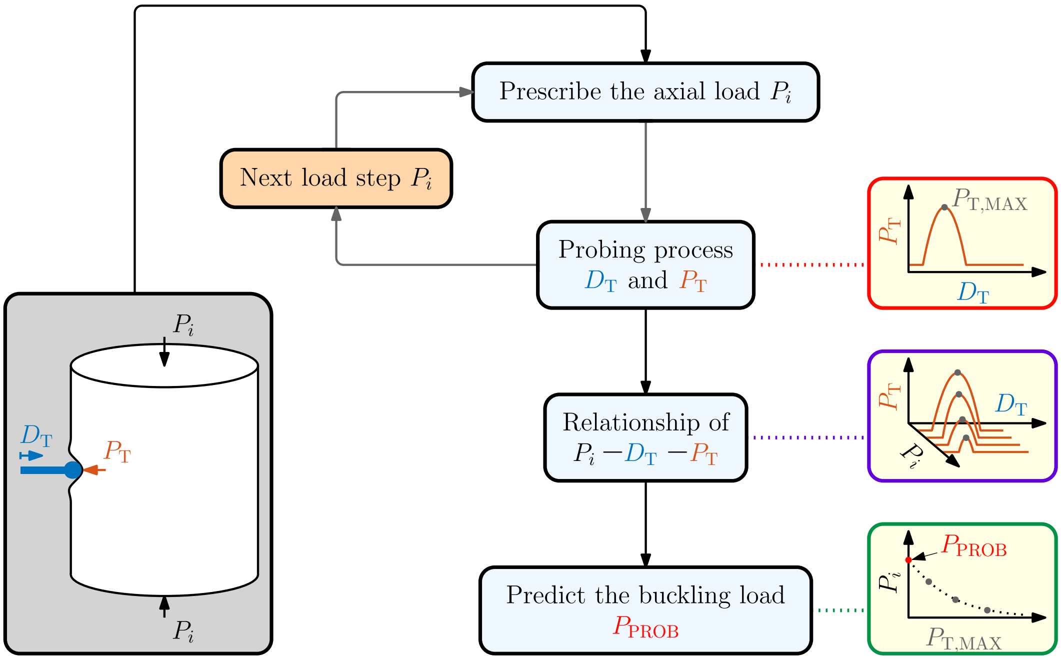
Prescribe the axial load P_i
Next load step P_i
Probing process
D_{T} and P_{T}
Relationship of
$P_i - D_{\mathrm{T}} - P_{\mathrm{T}}$
Predict the buckling load
P_{PROB}
P_i
D_{T}
P_{T}
P_i
P_{T}
$P_{\mathrm{T,MAX}}$
D_{T}
P_{T}
D_{T}
P_i
P_i
P_{PROB}
$P_{\mathrm{T,MAX}}$

Figure 2.7: Schematic diagram of the probing technique evaluated in [45].

Following the scheme of Figure 2.7, Fan [45] performed the first systematic numerical assessment of the probing technique. The probe was modeled as an analytical rigid body, which was in contact with the surface of the cylinder. The radial displacement D_{T} was prescribed through the rigid probe, and P_{T} was evaluated at the nodes within the region of influence at nine axial load steps. The buckling load was predicted by extrapolating $P_{\mathrm{T,MAX}}$ to zero, as represented in the chart contoured by □ in Figure 2.7.

The study considered a cylinder with perfect geometry and disturbed by dimple-shaped imperfections or measured mid-surface imperfections. For all cases, the prediction P_{PROB} associated with the smallest deviation was obtained probing the model at the location with the greatest imperfection amplitude. The author concluded that the probe size has a small influence on the predictions and that the axial load must be carefully controlled for guaranteeing a truly nondestructive experiment.

2.5 Numerical assessment of existing VCTs

In this section, a part of the results published in [46] is discussed to expose some aspects of the dynamic behavior of imperfection-sensitive cylinders related to the applicability of existing VCTs. In the mentioned paper, a numerical assessment of three methodologies, which were revisited in Section 2.3, was performed. The study involved ten nominally identical unstiffened composite cylindrical shells with the geometric and material properties presented in [15].

The detailed numerical models were validated based on buckling experiments published in [15] and employed to evaluate how the axially applied load influences the dynamic behavior. For each cylinder, 41 load steps were defined to calculate the frequency variation during the nonlinear static simulation being 40 load steps equally distributed from 2.5% to 100% of the nonlinear buckling load and the other load step at the first stable increment of the postbuckling regime.

Figure 2.8 reproduces the first vibration mode of the cylinder Z15U500, as named in [46], at the following load levels: (a) unloaded condition (204.8 Hz), (b) nonlinear buckling load (118.6 Hz), and (c) first stable increment in the postbuckling regime (26.6 Hz). From these results, there is no vibration mode associated with zero magnitude of the natural frequency at the buckling load, which is the foundation of most of the VCTs, for instance, see the methodologies published in [82, 85–88].

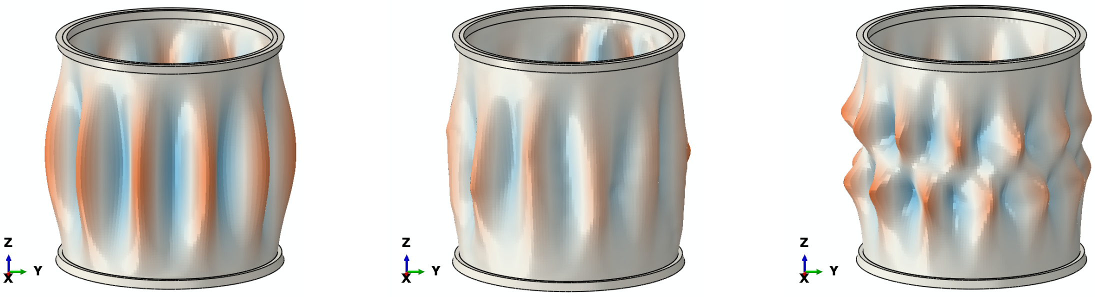

(a) Unloaded condition (204.8 Hz).

(b) Nonlinear buckling load (118.6 Hz).

(c) Postbuckling regime (26.6 Hz).

Figure 2.8: First vibration mode at different load levels for Z15U500 [46].

Considering Figure 2.8(a) and (b), the first vibration mode of Z15U500 is significantly affected by the nonlinear static state in the prebuckling regime, presenting a reduction of 42.1% in the frequency magnitude. Moreover, from Figure 2.8(c), the number of half-waves in the axial direction has changed in the postbuckling regime, which does not allow following the first unloaded vibration mode beyond buckling. Note in [46] that similar results were found for the other cylinders.

The first natural frequency variation is plotted up to the nonlinear buckling load in Figure 2.9 for all evaluated cylindrical shells, for reference, see [46]. Three VCTs were assessed: (a) f^2 versus p, (b) $(1-p)^2$ versus $1-f^4$, and (c) $(1-p)^2$ versus $1-f^2$. Besides, in Figure 2.9(a) and (c), the reference solutions are based on Equation (2.1)—as demonstrated in Chapter 4 of this thesis; similarly, in Figure 2.9(b), the reference solution is based on Equation (2.3).

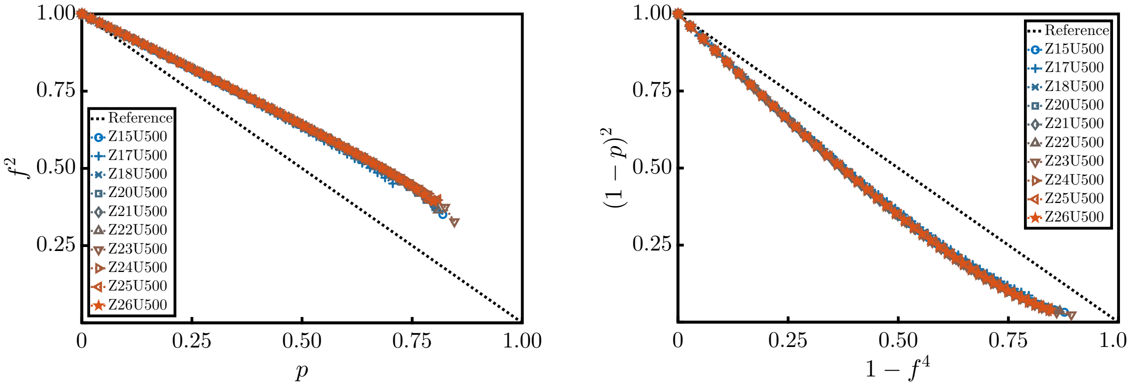

(a) Classic characteristic chart. **(b)** Modified characteristic chart [87].

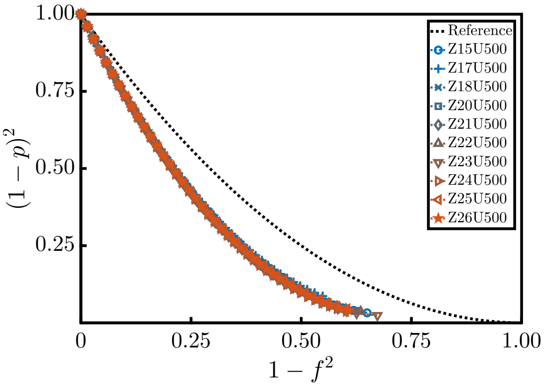

(c) Modified characteristic chart [35].

Figure 2.9: Numerical assessment of existing VCTs.

Analyzing Figure 2.9(a), a linear extrapolation of the numerical data to the abscissa would overestimate the buckling load for all cylindrical shells. Likewise, from Figure 2.9(b), a linear best fit evaluated at $1-f^4$ equal to one would result in negative values of ξ^2, which has no physical meaning. In the study, the authors attempted to estimate the buckling loads based on the classic [32] and semi-analytical [87] VCTs corroborating these remarks.

On the other hand, the results represented in the characteristic chart from [35], see Figure 2.9(c), are following the suggested second-order relationship between $(1-p)^2$ and $1-f^2$. As classified by the authors, the associated VCT provided proper estimations for eight out of the ten investigated unstiffened CFRP cylinders. For that reason, the mentioned VCT was considered in [46] the most appropriate technique for estimating the buckling load of the therein-evaluated cylindrical shells.

2.6 Summary and conclusions

This chapter focused on the state-of-the-art techniques for predicting the buckling load from the prebuckling stage applied to different types of structures. In this review, the main developments of three methodologies were examined: the Southwell plot, the VCT, and the probing technique. Furthermore, Section 2.5 provided a summary of the numerical study published in [46], which investigated the applicability of three existing VCTs to imperfection-sensitive composite cylindrical shells.

Throughout the years, the applicability of the Southwell plot was extensively confirmed to several types of structures under different types of loading. Nevertheless, for structures characterized by a complex buckling phenomenon, such as local instabilities, the method depends on the location where the deformations are measured. Hence, for the cases where the measurements do not culminate in a discernible slope, the accuracy of the estimated buckling load is compromised.

About the VCTs, the method is straightforward when applied to columns, for which the experimental buckling load is close to the theoretical one associated with the perfect structure. Additionally, the similarity between corresponding vibration and buckling modes holds even for boundary conditions different from simply supported. The mentioned aspects substantiate the classic linear VCT as one of the prevailing methods for such structures.

For plate-like structures, there is a commitment between the magnitude of the initial imperfections and the applicability of the VCT based on a linear extrapolation in the chart f^2 versus p. Concerning shells, the mentioned chart is characterized by a sharp bend close to the buckling load; therefore, the linear best-fit relationship does not provide appropriate estimations. As revisited for these cases, modified methods were implemented, requiring further investigation for practical industrial applications.

The probing technique established on the basis of the energy barrier against buckling is a promising method for estimating the buckling load of cylindrical shells. The methodology depends on probing representative locations of the specimen, which must be carefully addressed in a practical application ensuring a conservative estimation. The control of the axially applied load is another aspect to be taken into account to avoid permanent damage in the tested cylinder.

Concerning the numerical assessment published in [46], the fundamental natural frequency evaluated at the nonlinear buckling load is not equal to zero. Moreover, the classic [32] and the semi-analytical [87] methods fail to provide a proper estimation for the buckling load of the investigated unstiffened composite cylinders. In the conclusion of the study, the authors stated that the VCT empirically deduced in [35] is the most promising method for the evaluated structures.

Furthermore, different from other methods assessed in [46] and revisited within this chapter, the VCT introduced in [35] is established on the extrapolation of an extreme point; therefore, it does not rely on the assumption that the natural frequency will drop to zero at the buckling load. Additionally, the aforementioned approach was validated through nine experimental campaigns [81, 90−97] being two of them described as part of the experimental work of this thesis.

3 Scope and outline of the thesis

This chapter contextualizes the research of the thesis. The research hypothesis and the scope of the thesis are presented in Section 3.1. Subsequently, Section 3.2 shows the outline of each chapter and a summary of its respective contents.

3.1 Scope

Section 2.1 evidenced that the Southwell plot depends on the location where the deflections are evaluated being not directly suitable to imperfection-sensitive cylindrical shells [32]. Analogously, the recently conceived probing technique also demands an evaluation of representative locations of the specimen; besides, it imposes additional experimental difficulties for applying the transverse displacement and measuring the shock sensitivity nondestructively [34, 45].

On the other hand, the first vibration modes are representative of the global stiffness of the structure and measured independently of the assessed location [95]. Despite this advantage, the current scenario places the VCT applied to imperfection-sensitive cylindrical shells as not mature enough for industrial applications [82]; basically, the majority of the validated methods consist of empirical curve fitting procedures of the experimental data, for instance, see [35, 82, 84, 85, 87, 88].

Nonetheless, observe that among the mentioned VCTs, two methods based on the parametric form $(1-p)^2$, available in [35, 87], achieved notable results, being validated by several experimental campaigns, *vide* [81, 89−97]. The first one of them, defined in [87], depends on the dropping to zero of the appropriate natural frequency, and its modified version, suggested in [35], depends on an empirical second-order relationship between $(1-p)^2$ and $1-f^2$ evaluated for the first natural frequencies.

From this viewpoint, there is interest in revisiting the analytical formulation of the free vibration of axially loaded unstiffened cylindrical shells for representing the parametric form $(1-p)^2$ in terms of the loaded natural frequency. Furthermore, bearing in mind that the first buckling modes and the first vibration modes hardly coincide for such structures, the load-shortening curve of imperfection-sensitive cylindrical shells in terms of $(1-p)^2$ should be investigated towards a novel VCT definition.

Given these points, the research hypothesis of this thesis was delineated as:

"It is possible to predict the buckling load of imperfection-sensitive cylindrical shells through an analytically verified vibration correlation technique that does not depend on the similarity between the buckling and vibration modes."

Additionally, the following working hypotheses were formulated to investigate analytically, numerically, and experimentally the research hypothesis:

- It is possible to rearrange the well-known linear relationship between f^2 and p, corroborating the second-order relationship between $(1-p)^2$ and $1-f^2$ empirically introduced in [35].
- It is possible to evaluate the typical load-shortening response of an imperfect unstiffened cylindrical shell towards establishing a VCT based on the minimum of an adjusted equation for $(1-p)^2$.
- It is possible to verify numerically that the demonstrated relationship holds in the presence of initial imperfections and more realistic boundary conditions paving the path for practical applications.
- It is possible to validate experimentally the VCT for a metallic orthotropic skin-dominated cylinder with internal pressure, an unstiffened thin-ply composite laminated cylinder with internal pressure and in-plane imperfections, and three equivalent unstiffened composite cylinders tested at different facilities.

Furthermore, during the development of this doctoral thesis, two articles in conferences [46, 103] and three articles in peer-reviewed scientific journals [95, 97, 104] were published as listed in Appendix A.

3.2 Outline of the thesis

The present thesis is organized into seven chapters:

- **Chapter 1 — Introduction:** gives the motivation of the thesis.
- **Chapter 2 — State of the art:** revisits the state-of-the-art nondestructive experimental procedures to determine the *in-situ* buckling load; moreover, some

aspects of the dynamic behavior of imperfection-sensitive composite cylinders are discussed.

- **Chapter 3 — Scope and outline of the thesis:** delineates the scope, the research hypothesis, and the outline of the thesis.
- **Chapter 4 — Analytical verification:** revises the free vibration of an axially loaded isotropic cylindrical shell. After that, the steps for the rearrangement of the linear relationship between f^2 and p to a second-order equation between $(1-p)^2$ and $1-f^2$ are presented. Afterward, the typical load-shortening response of an unstiffened cylindrical shell is evaluated for a VCT definition, which does not depend on the similarity between the buckling and vibration modes. At the end of the chapter, the VCT implementation is readdressed.
- **Chapter 5 — Numerical assessment:** proposes two theoretical cylindrical shells for a numerical assessment. At first, the numerical and analytical results are compared, verifying the finite element (FE) models. The models are then extended for investigating nonlinear effects associated with initial imperfections and more realistic boundary conditions on the methodology verified in Chapter 4. Finally, the VCT is evaluated through a systematic study that could be reproduced during the definition phase of the experiment.
- **Chapter 6 — Experimental validation:** describes the three experimental campaigns, based on five cylindrical shells, performed within the scope of this doctoral thesis. Fully descriptions of the test facilities and test set-ups are given. The experimental results are presented and, subsequently, employed for predicting the buckling load of the test specimens through the VCT demonstrated analytically herein.
- **Chapter 7 — Final remarks:** presents the main conclusions of the thesis; moreover, limits of the VCT applied to cylindrical shells are discussed, and proposals for further developments in this research area are listed.

4 Analytical verification

As revisited in Chapter 2, most of the VCTs are established on the similarity between the buckling and vibration modes; thus, based on the drop to zero of the natural frequency. The first methodology not relying on such similarity, to the best of the author's knowledge, was developed empirically in [35]. This method consists of an important step in the context of imperfection-sensitive unstiffened cylindrical shells, and in this chapter, its analytical foundation is deduced.

Firstly, Section 4.1 reviews the free vibration of an axially loaded unstiffened isotropic cylindrical shell. Following this, Section 4.2 proposes a rearrangement of the reviewed equations towards evaluating $(1-p)^2$ in terms of the loaded natural frequency. Afterward, Section 4.3 devises a VCT definition from the typical behavior of imperfection-sensitive cylindrical shells, closing the loop of the analytical verification; finally, the implementation of the VCT is outlined in Section 4.4.

4.1 Free vibration of an axially loaded cylinder

Consider the conventional cylindrical shell structure depicted in Figure 4.1, which has an axial length L, a constant thickness h, and a middle surface radius R. An orthogonal cylindrical coordinate system (x, θ, z) is defined in the middle surface of the shell as a reference, where x, θ, and z are the axial, circumferential, and radial directions, respectively, being u, v, and w their corresponding displacement components of the middle surface of the shell.

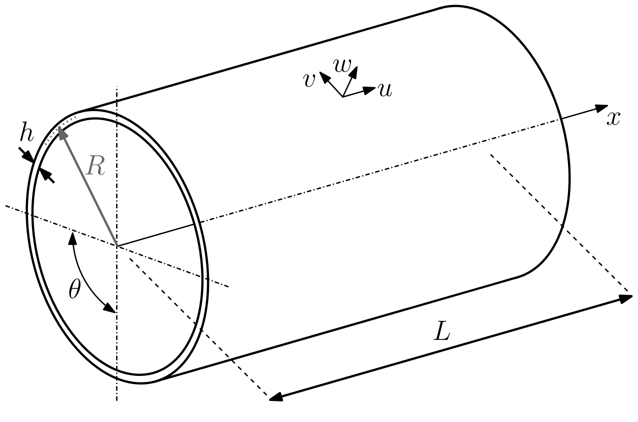

Figure 4.1: Geometry of a conventional cylindrical shell.

The differential equations of motion are expressed in matrix notation as formulated in [105, 106]:

$$[L]\{u_i\} = \{0\} \tag{4.1}$$

where $\{u_i\}$ is the displacement vector $\{u \quad v \quad w\}^{\mathrm{T}}$ and $[L]$ is a matrix differential operator.

Considering the linearized Flügge-Lurie-Byrne's shell theory taking into account the prestress effects due to the uniform axial membrane force $\bar{N}_x$, which the magnitude is positive for tension loads, the matrix differential operator $[L]$ is expressed as [105]:

$$[L] = [L_{\mathrm{D}}] + k\,[L_{\mathrm{F}}] + \frac{1}{C_{\mathrm{N}}}\,[L_{\mathrm{I}}] \tag{4.2}$$

where k is given by $h^2/12R^2$, C_{N} is given by $Eh/(1-\nu^2)$, $[L_{\mathrm{D}}]$ contains the terms associated with Donnell's theory of shells, $[L_{\mathrm{F}}]$ contains the terms for extending Donnell's to Flügge-Lurie-Byrne's shell theory, and $[L_{\mathrm{I}}]$ contains the additional terms related to the initial stress state. The three operators are given by [105]:

$$[L_{\mathrm{D}}]=\begin{bmatrix} R^2\dfrac{\partial^2}{\partial x^2}+\dfrac{(1-\nu)}{2}\dfrac{\partial^2}{\partial\theta^2}-F_{\mathrm{IN}} & \dfrac{(1+\nu)}{2}R\dfrac{\partial^2}{\partial x\partial\theta} & \nu R\dfrac{\partial}{\partial x} \\ \dfrac{(1+\nu)}{2}R\dfrac{\partial^2}{\partial x\partial\theta} & \dfrac{(1-\nu)}{2}R^2\dfrac{\partial^2}{\partial x^2}+\dfrac{\partial^2}{\partial\theta^2}-F_{\mathrm{IN}} & \dfrac{\partial}{\partial\theta} \\ -\nu R\dfrac{\partial}{\partial x} & -\dfrac{\partial}{\partial\theta} & -(1+k\nabla^4)-F_{\mathrm{IN}} \end{bmatrix} \tag{4.3}$$

$$[L_{\mathrm{F}}]=\begin{bmatrix} \dfrac{(1-\nu)}{2}\dfrac{\partial^2}{\partial\theta^2} & 0 & -R^3\dfrac{\partial^3}{\partial x^3}+\dfrac{(1-\nu)}{2}R\dfrac{\partial^3}{\partial x\partial\theta^2} \\ 0 & \dfrac{3(1-\nu)}{2}R^2\dfrac{\partial^2}{\partial x^2} & -\dfrac{(3-\nu)}{2}R^2\dfrac{\partial^3}{\partial x^2\partial\theta} \\ R^3\dfrac{\partial^3}{\partial x^3}-\dfrac{(1-\nu)}{2}R\dfrac{\partial^3}{\partial x\partial\theta^2} & \dfrac{(3-\nu)}{2}R^2\dfrac{\partial^3}{\partial x^2\partial\theta} & -\left(1+2\dfrac{\partial^2}{\partial\theta^2}\right) \end{bmatrix} \tag{4.4}$$

$$[L_{\mathrm{I}}]=\begin{bmatrix} \bar{N}_x R^2\dfrac{\partial^2}{\partial x^2} & 0 & 0 \\ 0 & \bar{N}_x R^2\dfrac{\partial^2}{\partial x^2} & 0 \\ 0 & 0 & \bar{N}_x R^2\dfrac{\partial^2}{\partial x^2} \end{bmatrix} \tag{4.5}$$

where ν is the Poisson's ratio, and F_{IN} and ∇^4 are defined as:

$$F_{\mathrm{IN}} = \rho \frac{(1-\nu^2)}{E} R^2 \frac{\partial^2}{\partial t^2} \tag{4.6}$$

$$\nabla^4 = R^4 \frac{\partial^4}{\partial x^4} + 2R^2 \frac{\partial^4}{\partial x^2 \partial \theta^2} + \frac{\partial^4}{\partial \theta^4} \tag{4.7}$$

being ρ the mass density, t the time variable, and E Young's modulus.

Assuming a circular cylindrical shell with two simply supported SS3 edges, where $w = v = N_x = M_x = 0$, the solution of the differential equations is straightforward being the displacement components:

$$u(x, \theta, t) = A_{mn} \cos(\lambda_m x) \cos(n\theta) \cos(\omega_{mn} t) \tag{4.8}$$

$$v(x, \theta, t) = B_{mn} \sin(\lambda_m x) \sin(n\theta) \cos(\omega_{mn} t) \tag{4.9}$$

$$w(x, \theta, t) = C_{mn} \sin(\lambda_m x) \cos(n\theta) \cos(\omega_{mn} t) \tag{4.10}$$

where A_{mn}, B_{mn}, and C_{mn} are the amplitude coefficients, and λ_m is given by $m\pi/L$. Moreover, the range of axial half-waves m and the range of circumferential waves n are 1, 2, ..., and 0, 1, 2, ..., respectively.

Substituting the displacement functions into Equation (4.1), the following system of algebraic equations is obtained in terms of A_{mn}, B_{mn}, and C_{mn}:

$$\begin{bmatrix} \bar{\Omega}_{mn} - H_{11} & H_{12} & H_{13} \\ H_{12} & \bar{\Omega}_{mn} - H_{22} & H_{23} \\ H_{13} & H_{23} & \bar{\Omega}_{mn} - H_{33} \end{bmatrix} \begin{Bmatrix} A_{mn} \\ B_{mn} \\ C_{mn} \end{Bmatrix} = \begin{Bmatrix} 0 \\ 0 \\ 0 \end{Bmatrix} \tag{4.11}$$

being the terms H_{ij} (where i and j are equal to 1, 2, and 3, and $ij = ji$), which depend on m, n, and some mechanical and geometric properties of the cylindrical shell, and the frequency parameter $\bar{\Omega}_{mn}$ given by:

$$H_{11} = \bar{\lambda}_m^2 + \frac{(1-\nu)}{2} n^2 (1+k) \tag{4.12}$$

$$H_{12} = \frac{(1+\nu)}{2} \bar{\lambda}_m n \tag{4.13}$$

$$H_{13} = \nu \bar{\lambda}_m + k \left[\bar{\lambda}_m^3 - \frac{(1-\nu)}{2} \bar{\lambda}_m n^2 \right] \tag{4.14}$$

$$H_{22} = \frac{(1-\nu)}{2}\bar{\lambda}_m^2 + n^2 + k\frac{3(1-\nu)}{2}\bar{\lambda}_m^2 \tag{4.15}$$

$$H_{23} = -n - k\frac{3(1-\nu)}{2}\bar{\lambda}_m^2 n \tag{4.16}$$

$$H_{33} = 1 + k\left(\bar{\lambda}_m^2 + n^2\right)^2 + k\left(1 - 2n^2\right) \tag{4.17}$$

$$\bar{\Omega}_{mn} = \frac{(1-\nu^2)}{E}\rho R^2 \bar{\omega}_{mn}^2 - \frac{\bar{N}_x \bar{\lambda}_m^2}{C_{\mathrm{N}}} \tag{4.18}$$

where $\bar{\lambda}_m = \lambda_m R$.

The determinant of the left-hand side matrix of Equation (4.11) must be equal to zero for a nontrivial solution resulting in the following cubic characteristic equation for a pair of m and n:

$$\bar{\Omega}_{mn}^3 - T_2\bar{\Omega}_{mn}^2 + T_1\bar{\Omega}_{mn} - T_0 = 0 \tag{4.19}$$

where T_2, T_1, and T_0 are coefficients depending on H_{ij} from Equations (4.12)–(4.17):

$$T_2 = H_{11} + H_{22} + H_{33} \tag{4.20}$$

$$T_1 = H_{11}H_{22} + H_{11}H_{33} + H_{22}H_{33} - H_{12}^2 - H_{13}^2 - H_{23}^2 \tag{4.21}$$

$$T_0 = H_{11}H_{22}H_{33} - 2H_{12}H_{13}H_{23} - H_{11}H_{23}^2 - H_{22}H_{13}^2 - H_{33}H_{12}^2 \tag{4.22}$$

The three roots of Equation (4.19) are always real for any pair of m and n [105, 106] and by substituting them into Equation (4.18), the natural frequencies of the axially loaded cylindrical shell $\bar{\omega}_{mn}$ are calculated as:

$$\bar{\omega}_{mn}^2 = \frac{E}{(1-\nu^2)\rho R^2}\left(\bar{\Omega}_{mn} + \frac{\bar{N}_x \bar{\lambda}_m^2}{C_{\mathrm{N}}}\right) \tag{4.23}$$

The negative values from Equation (4.23) have no physical meaning being, therefore, neglected. The three positive values correspond to three natural frequencies, where each one is prevalently associated with one of the three displacement components. Finally, Equation (4.23) is expressed in a more convenient form:

$$\bar{\omega}_{mn}^2 = \omega_{mn}^2 + \frac{\bar{N}_x \bar{\lambda}_m^2}{\rho h R^2} \tag{4.24}$$

where ω_{mn}^2 is the corresponding squared unloaded natural frequency. Typically, the evaluated cylindrical shells have their fundamental natural frequency associated with the vibration mode mainly characterized by radial displacement.

The vibration modes are calculated through two linear-dependent equations determined from Equation (4.11). For example, returning to Equation (4.11) and dividing the first two equations by C_{mn} gives the following two linear-dependent equations in terms of the ratios between the amplitude coefficients:

$$\begin{bmatrix} \bar{\Omega}_{mn} - H_{11} & H_{12} \\ H_{12} & \bar{\Omega}_{mn} - H_{22} \end{bmatrix} \begin{Bmatrix} A_{mn}/C_{mn} \\ B_{mn}/C_{mn} \end{Bmatrix} = \begin{Bmatrix} -H_{13} \\ -H_{23} \end{Bmatrix} \tag{4.25}$$

The ratios between amplitude coefficients, i.e., A_{mn}/C_{mn} and B_{mn}/C_{mn}, define the vibration mode. The third coefficient C_{mn}, which is undetermined by Equation (4.25), is a scaling factor of the amplitude calculated through the initial conditions or a normalization criterion [106].

4.2 An analytical equation for $(1-p)^2$

Through Equation (4.24), the total applied load P, defined as $2\pi R\bar{N}_x$, is expressed in terms of the squared loaded natural frequency as:

$$P = G_m(\bar{\omega}_{mn}^2 - \omega_{mn}^2) \tag{4.26}$$

where $G_m = 2\pi\rho h R^3/\bar{\lambda}_m^2$.

Referencing [40, 105], the natural frequency dropping to zero is sufficient to obtain the associated buckling load of the perfect cylinder with SS3 boundary conditions:

$$P_{\mathrm{CR}} = G_m(\bar{\omega}_{mn}^2 - \omega_{mn}^2)|_{\bar{\omega}_{mn}^2=0} = -G_m\omega_{mn}^2 \tag{4.27}$$

Finally, the load ratio p from Equation (2.1) is found dividing Equation (4.26) by Equation (4.27):

$$p = 1 - f^2 \tag{4.28}$$

where $f = \bar{\omega}_{mn}/\omega_{mn}$.

The resultant equation, which is also presented in Equation (2.1), is rearranged to express the parametric form of the squared applied load $(1-p)^2$ in terms of the parametric form of the squared loaded natural frequency $1 - f^2$:

$$(1-p)^2 = \left[1 - \left(1 - f^2\right)\right]^2 \tag{4.29}$$

Equation (4.29) analytically demonstrates that the parametric form $(1-p)^2$ is related to $1 - f^2$ through a second-order equation, as empirically suggested in [35].

4.3 Experimental estimation of the KDF

Isotropic unstiffened cylindrical shells are highly imperfection-sensitive; as a consequence, a substantial drop in the experimental buckling load P_{EXP} is expected when compared to the theoretical buckling load calculated for the perfect structure P_{CR}. Figure 4.2 presents the typical load-shortening curve for an unstiffened cylindrical shell in terms of the load ratio $p = P/P_{\mathrm{CR}}$; besides, the chart depicts the parametric form $(1-p)^2$ and the KDF γ as defined in [12] and as related to ξ.

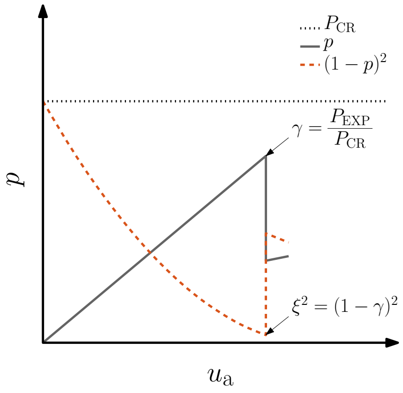

Figure 4.2: Typical load-shortening curve of an unstiffened cylindrical shell.

According to its definition, the parametric form $(1-p)^2$ has a nonlinear variation within the prebuckling regime, and its minimum magnitude occurs exactly at the instability point. At this point, the square root of $(1-p)^2$ is equal to ξ from Equation (2.4), as illustrated in Figure 4.2. This interpretation is grounded on the behavior of $(1-p)^2$, supporting the definition of a VCT that does not rely on the drop to zero of the natural frequency, but the extrapolation of the minimum magnitude of $(1-p)^2$.

Given that Equation (4.29) provides an analytical foundation for a second-order relationship between $(1-p)^2$ and $1 - f^2$, a VCT considering the defined statement is obtained by minimizing the referred equation with respect to $1 - f^2$ to estimate ξ^2.

For example, the minimization of Equation (4.29) results in $(1-p)^2 = 0$ at $1 - f^2 = 1$, where the second derivative is 2, which is constant and greater than zero, indicating that this result is the minimum point of Equation (4.29).

The described result was expected because the equations revisited throughout this chapter are deduced from the linearized Flügge-Lurie-Byrne's shell theory applied to a perfect cylinder. Accordingly, there is no drop in the load-carrying capacity due to initial imperfections. Moreover, for the prescribed SS3 boundary conditions, in which the buckling and vibration modes exactly match [40, 105], the first natural frequency of the loaded structure is equal to zero at the buckling load.

4.4 VCT implementation

During a VCT experimental campaign of an unstiffened cylindrical shell, the dynamic behavior is characterized for different axial load levels in the prebuckling regime, as illustrated in Figure 4.3. The measurements inherently take into account the imperfections, boundary conditions, and anisotropy of a specific set composed by the cylinder and the test set-up. For such an experimental set, ξ^2 is not zero, and usually, none of the first vibration modes matches the first buckling mode.

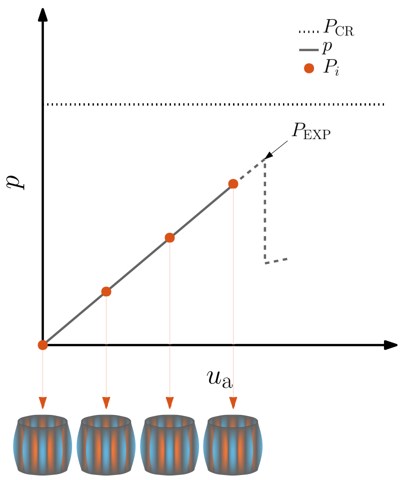

Figure 4.3: Illustration of a typical VCT experiment.

Under the described circumstances and towards a straightforward VCT, the study assumes that, within the prebuckling regime, the nonlinear behavior of the parametric form $(1-p)^2$ is still represented by a second-order equation in terms of $1-f^2$. Following this assumption, the modified characteristic chart empirically recommended in [35] is applicable, from which a fitted version of Equation (4.29) based on measured data from practical scenarios is obtained:

$$(1-p)^2 = A(1-f^2)^2 + B(1-f^2) + C \tag{4.30}$$

where A, B, and C are the coefficients determined through the best-fit procedure of the experimental data.

As illustrated in Figure 4.2, the minimum value of the parametric form $(1-p)^2$ is related to the square of the drop of the load-carrying capacity. Section 4.3 explored this interpretation, defining a direct VCT by extrapolating the minimum of $(1-p)^2$, represented as a second-order equation in terms of $1-f^2$, for estimating ξ^2. Thus, applying this observation on Equation (4.30), the estimated ξ^2 is expressed in terms of the fitting coefficients as:

$$\min(1-p)^2 = \xi^2 = -\frac{B^2}{4A} + C \tag{4.31}$$

where the positive square root evaluated as $1-\xi$ represents an estimation of the effective KDF γ of the experiment.

Taken together, Sections 4.2, 4.3, and 4.4 verify analytically the VCT defined in [35] and on scrutinizing the experimental campaigns [81, 90−97], its steps are restated as:

1. Calculate the first linear buckling load of the perfect structure.
2. Track the first vibration mode and corresponding natural frequency from the unloaded condition until an appropriate load level.
3. Plot the experimental data into the characteristic chart $(1-p)^2$ versus $1-f^2$.
4. Identify the second-order best-fit relationship between $(1-p)^2$ and $1-f^2$ and minimize the quadratic equation for evaluating ξ^2, as proposed in Equation (4.31).
5. Use the estimated ξ^2 and the linear buckling load P_{CR} into Equation (2.4) to assess the *in-situ* buckling load of the structure.

4.5 Summary and conclusions

This chapter analytically demonstrated the VCT empirically developed in [35] and experimentally validated in nine scientific papers, see [81, 90−97]. Initially, the anticipated second-order relationship between the parametric forms $(1-p)^2$ and $1-f^2$ is corroborated through the rearrangement of the classic linear relationship between the applied load and the squared loaded natural frequency for an isotropic unstiffened cylindrical shell, for which the formulation was revisited in Section 4.1.

Afterward, the relationship between the minimum magnitude of $(1-p)^2$ and the KDF γ is established from the typical load-shortening curve of an imperfection-sensitive cylinder. This interpretation, solely based on the static behavior evaluated as $(1-p)^2$, can be applied to a nonlinear equation of this parametric form and does not depend on the drop to zero of the natural frequency, but whether the assumed equation for $(1-p)^2$ is correctly representing its nonlinear behavior below buckling.

Finally, the VCT implementation is exemplified for practical scenarios assuming that a second-order equation also represents the relationship between $(1-p)^2$ and $1-f^2$ in the presence of different boundary conditions, initial imperfections, and other degrees of anisotropy. In conclusion, the given verification through existing linear equations enhances the understanding of the VCT conceived in [35] and paves the path for its consolidation in the context of imperfection-sensitive cylindrical shells.

5 Numerical assessment

This chapter describes the numerical work performed in this thesis being the main objective to assess the effects of different boundary conditions and realistic initial imperfections on the functional relationship of Equation (4.29). In Section 5.1, two theoretical isotropic cylindrical shells are specified, and an existing mid-surface imperfection pattern is chosen. After that, Section 5.2 defines the numerical models representing the nominal and the disturbed geometry of each cylinder.

Following this, Section 5.3 verifies the reference models considering SS3 boundary conditions based on the analytical equations revisited in Section 4.1. Subsequently, Section 5.4 extends the verified FE models assessing the effects of different boundary conditions (SS4) and mid-surface imperfections. At the end of the chapter, Section 5.5 examines the numerical results for a systematic evaluation of the VCT, which could be reproduced during the planning phase of the experiment, helping with its definition.

5.1 Overview of the cylindrical shells

The nonlinear numerical assessment considers two theoretical isotropic unstiffened cylinders that would fit DLR test facilities, named ZAL1 and ZAL2. Table 5.1 presents the geometric characteristics defining both structures. The study assumes the aluminum alloy AL7075-T7351, which is typically employed in aerospace designs. Concerning the material properties reproduced in Table 5.2, they were obtained from the Metallic Materials Properties Development and Standardization (MMPDS) [107].

Table 5.1: Geometric characteristics of ZAL1 and ZAL2.

Property	**ZAL1**	**ZAL2**
Free length [mm]	500	800
Middle surface radius [mm]	250	400
Shell thickness [mm]	0.50	0.50
Radius over thickness ratio	500	800
Radius over length ratio	0.50	0.50

Table 5.2: Mechanical material properties of AL7075-T7351 [107].

Property	**Magnitude**
Compressive elastic modulus [MPa]	73,084
Poisson's ratio	0.33
Mass density [kg/m^3]	2,796

The influence of real geometric imperfections is investigated employing the measured imperfection signature of a stainless steel laser-welded unstiffened cylinder tested in [90], identified there as SST-1. The measured data of SST-1 are available in the DESICOS plug-in [108], considering its original magnitude as related to the middle surface best-fit radius of the cylinder (approximately 250 mm). Figure 5.1 depicts the described measured imperfection pattern (in mm).

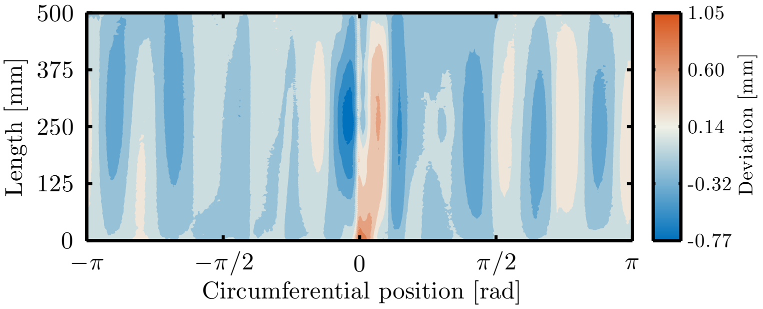

Figure 5.1: Measured mid-surface imperfection of SST-1, available in [108].

5.2 Finite element analyses

The FE models of this chapter are dedicated to the linear buckling, nonlinear static, and linear frequency solutions. The linear buckling analysis provides the theoretical buckling load. The nonlinear static solution followed by linear frequency steps at chosen axial load levels yields the nonlinear static response and the variation of the natural frequencies. The study uses the commercial FE solver Abaqus Standard 6.16® for pre- and postprocessing of the numerical models hereafter described.

The Newton-Raphson iterative procedure with artificial damping stabilization is used as the nonlinear solver for the axial loading step. For the eigenvalue problems, i.e., linear buckling and free vibration analyses, the default Lanczos solver is employed.

Referencing the convergence study performed in [18], the FE models are defined with parabolic quadrilateral thin-shell elements with eight nodes, six degrees of freedom per node, and reduced integration (labeled S8R elements in Abaqus® library).

Two types of simply supported boundary conditions, i.e., SS3 and SS4, are simulated on both edges of the cylinders. The SS3, also known as shear diaphragm, is characterized by $w = v = N_x = M_x = 0$ and compatible with Equations (4.8)−(4.10); therefore, it is directly compared to the analytical equations from Section 4.1. The SS4 is defined by $w = v = u = M_x = 0$, being closer to the experimental boundary conditions and, consequently, more appropriate for the verification of the VCT.

For implementing the SS3 boundary conditions in Abaqus®, additional constraints along the edge lying in the middle of the length of the cylinder are defined, which keep the symmetry and avoid rigid body motions. Figure 5.2 depicts the details of the implemented SS3 and SS4 boundary conditions. Observe that the described constraints are related to a cylindrical coordinate system specified at the center of the circle defined by the bottom edge (also presented in the figure).

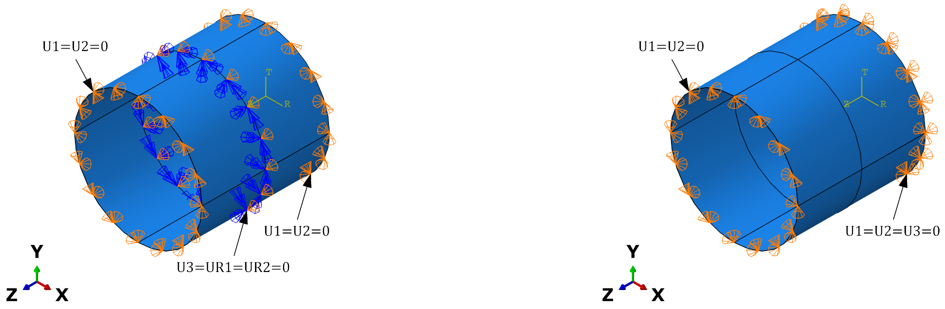

(a) SS3 boundary conditions. **(b)** SS4 boundary conditions.

Figure 5.2: Implementation of the boundary conditions in the FE models.

Shell edge forces are applied on both edges in the linear buckling FE models with SS3 boundary conditions for loading the structures. For the models considering SS4 boundary conditions, the nonlinear static problem uses enforced displacement, whereas the linear buckling problem considers a unitary force. Both described loads are applied at the center of the circle defined by the top edge and distributed through multipoint constraint equations to the nodes lying along the top edge of the cylinders.

A convergence analysis taking into account 35, 70, 140, 280, and 560 elements over the circumference with a consistent global element size, keeping square elements in other directions, is performed for ZAL1. The FE models consider SS4 boundary conditions being the main objective to obtain an appropriate theoretical buckling load, i.e., not necessarily associated with a converged first linear buckling mode. Furthermore, these results in terms of the element size will be extended to the geometry of ZAL2.

Considering the first linear buckling modes of a perfect isotropic cylinder with SS4 boundary conditions, the difference between the magnitudes of the corresponding eigenvalues is minor. As a consequence, the smallest perturbation, e.g., the element size, stimulates a different first buckling mode. For this reason, the first axis-symmetrical buckling mode is tracked. Figure 5.3 presents the convergence study, in which the deviation is related to the finest mesh, and a threshold of 1% is outlined.

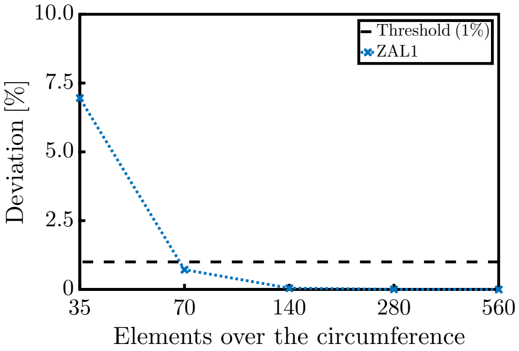

Figure 5.3: Convergence of the first axis-symmetrical buckling load of ZAL1.

From Figure 5.3, the FE mesh associated with 140 elements over the circumference, which corresponds to an element size of 11.22 mm, demonstrated an appropriate convergence (with a deviation to the finest mesh of roughly 0.05%). Based on the referred element size, the resulting FE models have 6,160 and 16,128 S8R shell elements associated with 18,760 and 48,832 nodes for ZAL1 and ZAL2 geometries, respectively. Figure 5.4 depicts an overview of the converged FE meshes of both models.

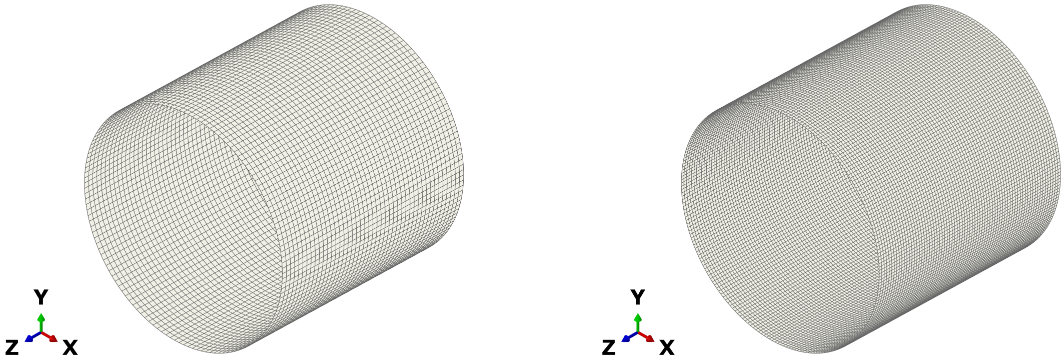

(a) Cylinder ZAL1. **(b)** Cylinder ZAL2.

Figure 5.4: FE meshes of ZAL1 and ZAL2.

The mentioned characteristic of the linear buckling solution of an isotropic cylinder with SS4 boundary conditions is exemplified in the comparison presented in Table 5.3, which contains the magnitudes of the 1^{st}, 10^{th}, 20^{th}, 50^{th}, and 100^{th} linear buckling loads for the converged FE models. Furthermore, in the mentioned table, the deviation δ_{CR} is calculated as related to the buckling load associated with the first buckling mode of the respective cylindrical shells.

Table 5.3: First linear buckling loads of ZAL1 and ZAL2 considering SS4.

	ZAL1		**ZAL2**	
Mode	$\boldsymbol{P}_{\mathrm{CR}}$ **[kN]**	$\boldsymbol{\delta}_{\mathrm{CR}}$ **[%]**	$\boldsymbol{P}_{\mathrm{CR}}$ **[kN]**	$\boldsymbol{\delta}_{\mathrm{CR}}$ **[%]**
1	70.18	-	70.18	-
10	70.19	0.02	70.19	0.01
20	70.27	0.13	70.21	0.04
50	70.58	0.57	70.28	0.14
100	71.03	1.21	70.40	0.31

Analyzing Table 5.3, the 100^{th} buckling load is 1.21% and 0.31% greater than the corresponding first buckling load for ZAL1 and ZAL2, respectively. The results corroborate a small deviation between the magnitudes of the first 100 buckling loads for an isotropic cylinder with SS4 boundary conditions. In practice, any of these modes could be stimulated by the real imperfections thus being eligible for a numerical assessment; nevertheless, in this thesis, the measurements from Figure 5.1 are taken into account.

Two main FE models are defined for each cylinder:

1. Reference model: considers the nominal geometry without initial geometric imperfection and both boundary conditions (SS3 and SS4), being employed in two types of eigenvalue problems: linear buckling and free vibration analyses.
2. Imperfect model: considers the geometry disturbed by the initial imperfection presented in Figure 5.1 and SS4 boundary conditions. For each cylindrical shell, the imperfection amplitude is downscaled to a maximum deviation of 50%, 75%, and 100% of the shell thickness. The initial positions of the nodes are disturbed using a python script based on the inverse-weighted interpolation and scaling rules from [18] employed here for the five closest measured points. Figure 5.5 shows the disturbed FE meshes of ZAL1 and ZAL2 considering the original

magnitude of Figure 5.1 (in mm) and the deformation amplified by 20. These models are employed for a nonlinear static analysis followed by free vibration analyses at different load levels.

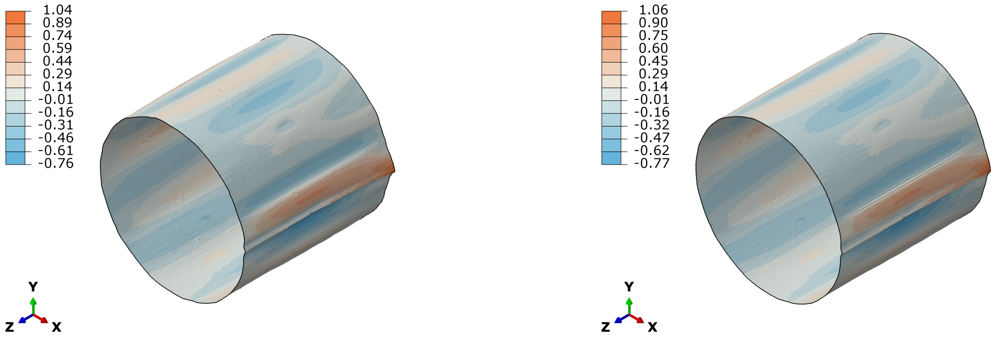

(a) Cylinder ZAL1. **(b)** Cylinder ZAL2.

Figure 5.5: Initial mid-surface imperfection applied in the FE models.

5.3 Analytical versus numerical results

The first vibration mode is associated with the minimum magnitude among the natural frequencies; moreover, the equations depend on the number of axial half-waves m and circumferential waves n. Thus, a Matlab® algorithm was written to calculate the natural frequencies based on Equation (4.24). Figure 5.6 depicts the natural frequencies for different magnitudes of m and n of both cylinders and highlights the first (minimum) natural frequency of each one.

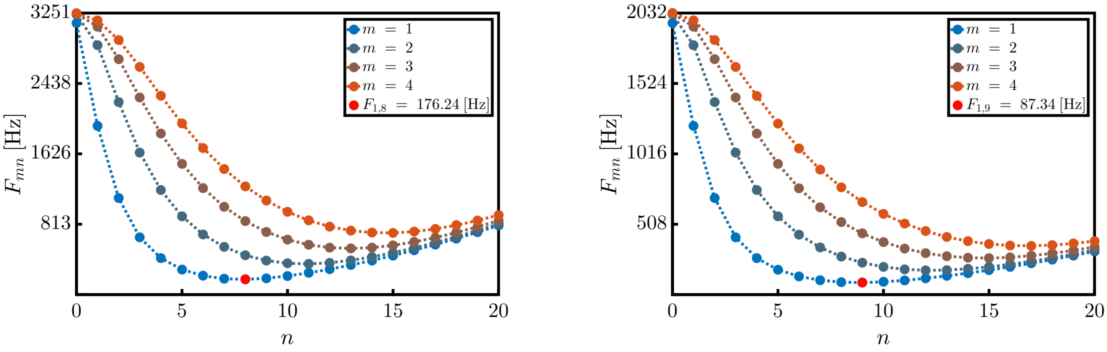

(a) Cylinder ZAL1. **(b)** Cylinder ZAL2.

Figure 5.6: Natural frequencies for different magnitudes of m and n.

From Figure 5.6, the first unloaded natural frequency F_1 of ZAL1 and ZAL2 is associated with the following pairs (m, n): (1, 8) and (1, 9), respectively. Additionally, Figure 5.7 shows the corresponding first unloaded vibration mode of each cylinder, which is calculated through Equation (4.25).

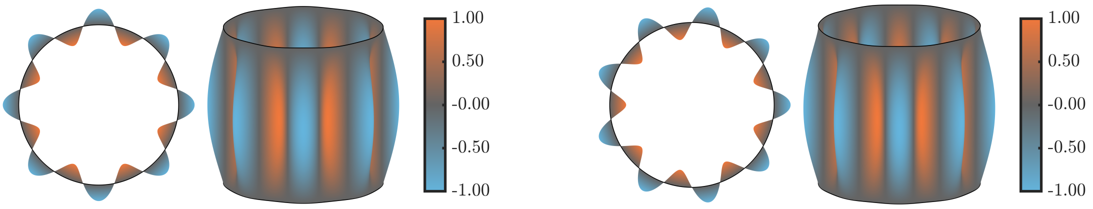

(a) Cylinder ZAL1. **(b)** Cylinder ZAL2.

Figure 5.7: First unloaded vibration mode of ZAL1 and ZAL2 considering SS3.

The analytical results constitute a reference for verifying the numerical models with SS3 boundary conditions. Table 5.4 presents the direct comparison with the buckling load from Equation (4.27) and the first natural frequency at different compressive load levels from Equation (4.24), where the deviation δ_{ANA} is calculated as related to the analytical results. Besides, the natural frequencies (both numerical and analytical) are associated with (m, n) equal to (1, 8) and (1, 9) for ZAL1 and ZAL2, respectively.

Table 5.4: Numerical and analytical results of ZAL1 and ZAL2 considering SS3.

	Analytical		**Numerical**		$\boldsymbol{\delta}_{\mathrm{ANA}}$ [%]	
Variable	**ZAL1**	**ZAL2**	**ZAL1**	**ZAL2**	**ZAL1**	**ZAL2**
P_{CR} [kN]	68.21	68.62	68.24	68.64	0.04	0.03
F_1 [Hz]	176.24	87.34	176.22	87.33	-0.01	-0.01
$\bar{F}_1$ at 25% of P_{CR} [Hz]	152.63	75.64	152.65	75.65	0.01	0.01
$\bar{F}_1$ at 50% of P_{CR} [Hz]	124.62	61.76	124.64	61.76	0.02	0.00
$\bar{F}_1$ at 75% of P_{CR} [Hz]	88.12	43.67	87.76	43.56	-0.41	-0.25

From Table 5.4, there is an excellent agreement between the analytical and numerical results being the maximum deviation magnitude of 0.41% for $\bar{F}_1$ at 75% of P_{CR} for ZAL1. Another important aspect is the comparison between the vibration and buckling modes for a cylinder with SS3 boundary conditions. Therefore, Figure 5.8 presents the numerical results for the first buckling mode and first unloaded vibration mode of ZAL1 and ZAL2 with the referred boundary conditions.

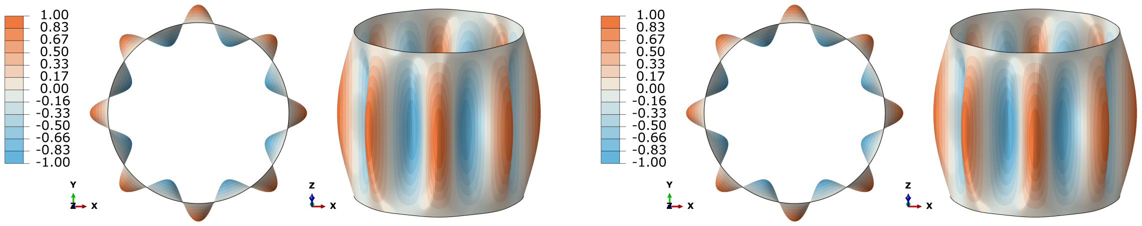
1.00
0.83
0.67
0.50
0.33
0.17
0.00
-0.16
-0.33
-0.50
-0.66
-0.83
-1.00
Y
X
Z
X
1.00
0.83
0.67
0.50
0.33
0.17
0.00
-0.16
-0.33
-0.50
-0.66
-0.83
-1.00
Y
X
Z
X

(a) First buckling mode (ZAL1). **(b)** First buckling mode (ZAL2).

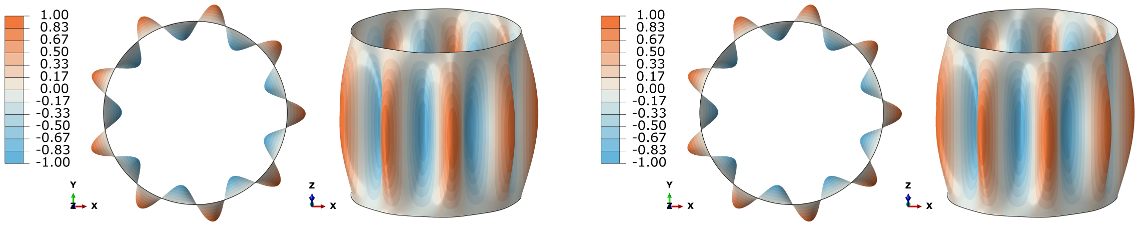
1.00
0.83
0.67
0.50
0.33
0.17
0.00
-0.17
-0.33
-0.50
-0.67
-0.83
-1.00
Y
X
Z
X
1.00
0.83
0.67
0.50
0.33
0.17
0.00
-0.17
-0.33
-0.50
-0.67
-0.83
-1.00
Y
X
Z
X

(c) First unloaded vibration mode (ZAL1). **(d)** First unloaded vibration mode (ZAL2).

Figure 5.8: First buckling mode and first unloaded vibration mode for SS3.

Evaluating Figure 5.8, the first unloaded vibration mode exactly matches the first buckling mode, which is expected for SS3 boundary conditions, for reference, see [40, 105]. Furthermore, Figure 5.8(c) exactly matches Figure 5.7(a); likewise, Figure 5.8(d) exactly matches Figure 5.7(b). This correspondence between vibration and buckling modes corroborates the equivalence between the reference models with SS3 boundary conditions and the recapitulated formulations of Chapter 4.

5.4 Nonlinear numerical assessment

In practical scenarios, SS3 boundary conditions are not realistic; besides, real structures have initial imperfections like the mid-surface deviations depicted in Figure 5.1. Given these points, this section proposes to extend the numerical analysis to assess the frequency variation considering geometric nonlinearities, initial geometric imperfections, and SS4 boundary conditions. This study is closer to an actual experimental campaign; thus, more appropriate for evaluating the VCT.

Firstly linear buckling and free vibration analyses are solved considering the reference model defined in Section 5.2 with SS4 boundary conditions. The first linear buckling load is 70.18 kN for both cylinders, and the first unloaded natural frequency is 250.65 and 126.43 Hz for ZAL1 and ZAL2, respectively. Furthermore, Figure 5.9 shows the corresponding first buckling mode and first unloaded vibration mode of ZAL1 and ZAL2, respectively.

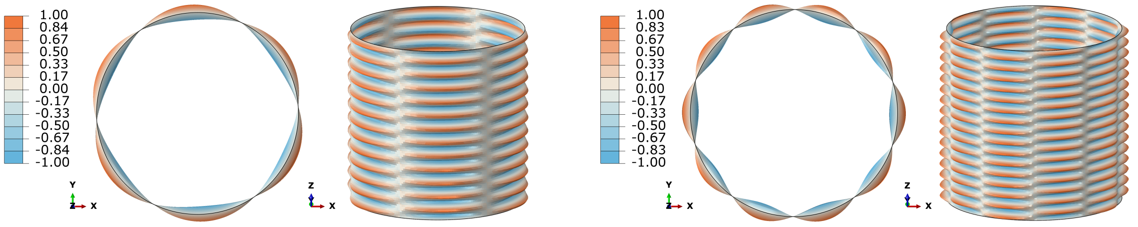
1.00
0.84
0.67
0.50
0.33
0.17
0.00
-0.17
-0.33
-0.50
-0.67
-0.84
-1.00
Y
X
Z
X
1.00
0.83
0.67
0.50
0.33
0.17
0.00
-0.17
-0.33
-0.50
-0.67
-0.83
-1.00
Y
X
Z
X

(a) First buckling mode (ZAL1). **(b)** First buckling mode (ZAL2).

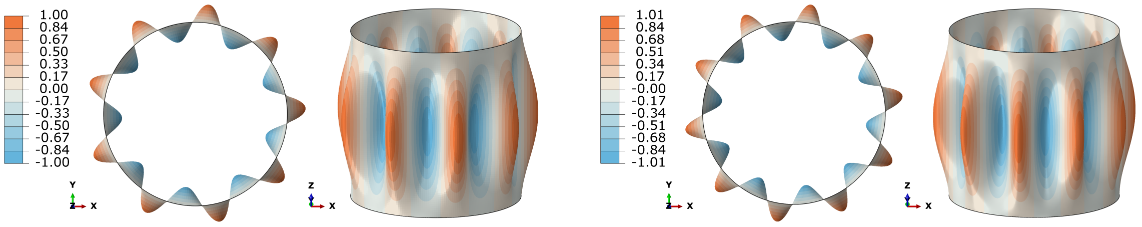
1.00
0.84
0.67
0.50
0.33
0.17
0.00
-0.17
-0.33
-0.50
-0.67
-0.84
-1.00
Y
X
Z
X
1.01
0.84
0.68
0.51
0.34
0.17
-0.00
-0.17
-0.34
-0.51
-0.68
-0.84
-1.01
Y
X
Z
X

(c) First unloaded vibration mode (ZAL1). **(d)** First unloaded vibration mode (ZAL2).

Figure 5.9: First buckling mode and first unloaded vibration mode for SS4.

Analyzing Figure 5.9, there is no similarity between the first buckling mode and the first unloaded vibration mode for both cylindrical shells. This scenario is recurrent in practical applications for unstiffened cylinders consisting of an obstacle for tracking an appropriate vibration mode (similar to a corresponding buckling mode in terms of m and n) during the experiments. This typical characteristic endorses the need for developing a VCT independent of the drop to zero of the natural frequency.

The nonlinear numerical assessment considers the imperfect model with SS4 boundary conditions focusing on evaluating the second-order relationship presented in Equation (4.29) against a more realistic application. Accordingly, Section 5.5 employs these results for verifying the VCT, providing a better understanding of the convergence of the method and some insight into planning the experiment. Table 5.5 shows the main solver parameters considered for the nonlinear static analysis.

Table 5.5: Solver parameters for the nonlinear static analysis.

Parameter	**Magnitude**
Damping factor	10^{-7}
Initial increment	0.001
Minimum increment	10^{-6}
Maximum increment	0.001

Figure 5.10 presents the load-shortening curves of ZAL1 and ZAL2 considering all initial imperfection magnitudes, while Table 5.6 summarizes the respective nonlinear buckling loads P_{NL} and effective KDFs γ_{NL} (calculated as $P_{\mathrm{NL}}/P_{\mathrm{CR}}$). Hereafter, three additional labels are defined for ZAL1 and ZAL2 by adding an "M" followed by three digits representing the maximum amplitude of the initial geometric imperfection: 050, 075, and 100 representing 50%, 75%, and 100% of the shell thickness, respectively.

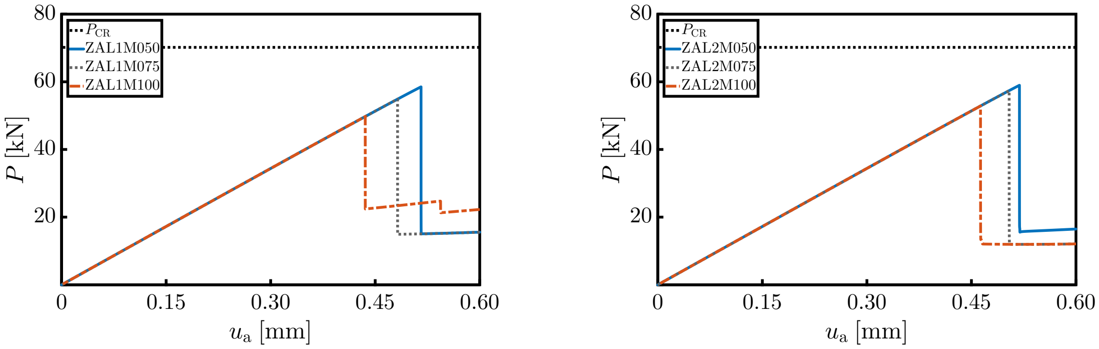

(a) Cylinder ZAL1. **(b)** Cylinder ZAL2.

Figure 5.10: Load-shortening curves as related to the initial imperfections.

Table 5.6: Nonlinear buckling loads and effective KDFs of ZAL1 and ZAL2.

Cylinder	P_{NL} **[kN]**	γ_{NL}
ZAL1M050	58.51	0.83
ZAL1M075	53.88	0.78
ZAL1M100	49.74	0.71
ZAL2M050	58.97	0.84
ZAL2M075	57.38	0.82
ZAL2M100	52.85	0.75

Analyzing Figure 5.10 and Table 5.6, the initial mid-surface imperfections significantly affect the nonlinear buckling load of the cylindrical shells. As expected, smaller KDFs are associated with greater amplitudes of the geometric imperfections. Furthermore, note that the downscaled amplitudes 50%, 75%, and 100% of the shell thickness result in two similar ranges of KDF for ZAL1 and ZAL2, respectively: from 0.71 to 0.83 and from 0.75 to 0.84.

In the following, the nonlinear static results from Figure 5.10 are divided into 41 load steps for a sequence of axially loaded free vibration analyses. These load steps are defined equally distributed from 2.5% up to 100% of the buckling load P_{NL} and at P_{PB}, which designates the first stable increment in the postbuckling regime. Figure 5.11 shows the load-shortening curves of the evaluated cylindrical shells, emphasizing the load steps followed by linear frequency analyses.

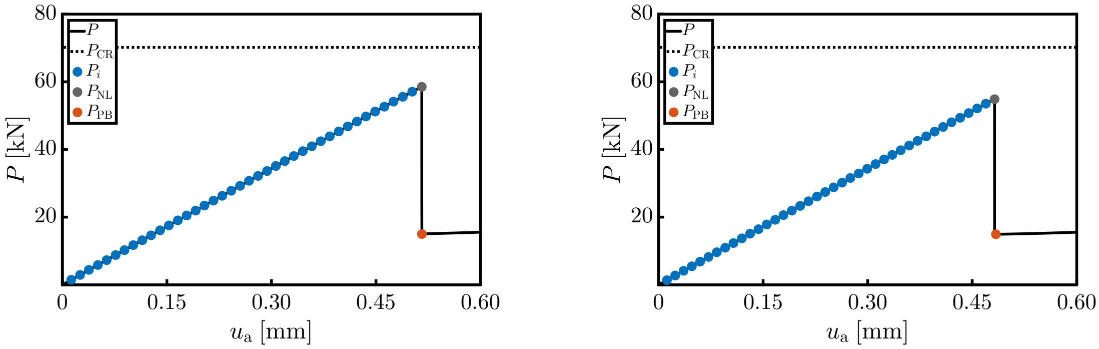

(a) Cylinder ZAL1M050. **(b)** Cylinder ZAL1M075.

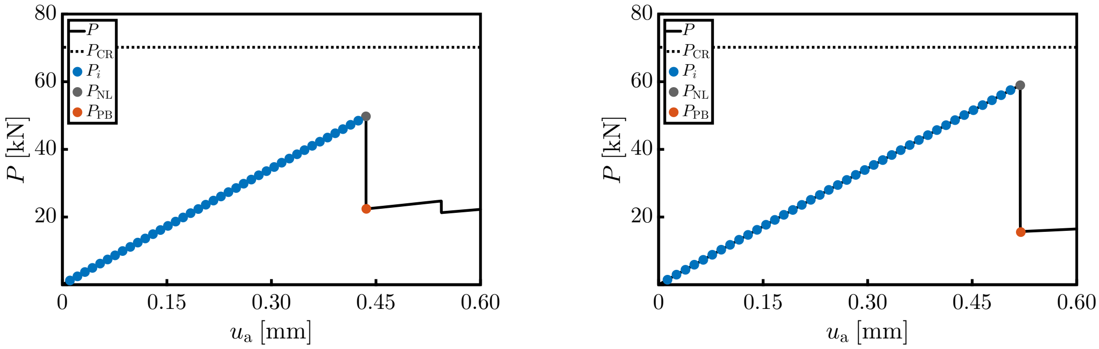

(c) Cylinder ZAL1M100. **(d)** Cylinder ZAL2M050.

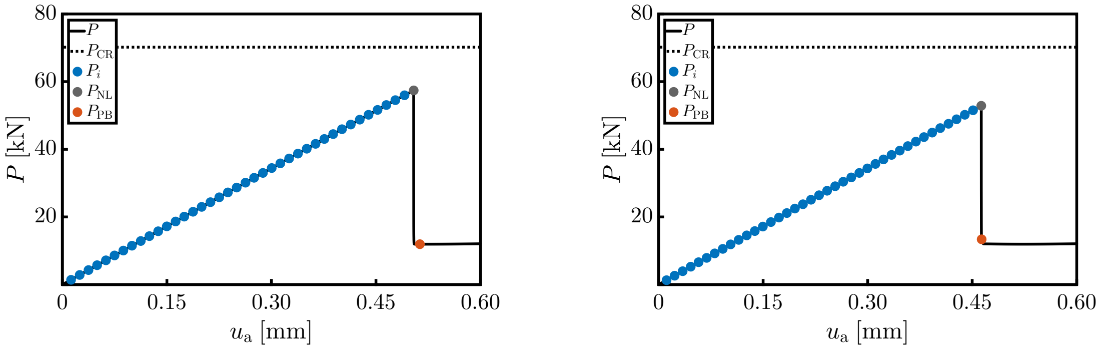

(e) Cylinder ZAL2M075. **(f)** Cylinder ZAL2M100.

Figure 5.11: Load steps followed by frequency analyses.

The numerical investigation covers the complete prebuckling path of the cylinders with a high number of load steps. Such a dense evaluation is important to comprehend the contrast between the behavior of the natural frequencies in a condition closer to a real application and the ideal case from Equation (4.29). Thus, it challenges the assumption made in Section 4.4, which establishes that a second-order relationship holds in practical scenarios.

The variation of each vibration mode during the axial loading is obtained through an algorithm based on the modal assurance criterion (MAC) implemented in Matlab®. The MAC index gives a comparison between two vectors of the same length being close to one if a linear relationship between the two vectors exists and close to zero if the vectors are linearly independent [109]. Besides automatic postprocessing, this algorithm allows a thorough evaluation of the vibration response.

In this script, the MAC index is calculated between each vibration mode in the current load step and all vibration modes in the next load step. Afterward, the maximum MAC index is assumed associated with the evaluated vibration mode in the next load level. The described process is repeated until the final load step is analyzed. Figure 5.12 presents the MAC index variation for the first vibration mode considering the evaluated theoretical cylindrical shells.

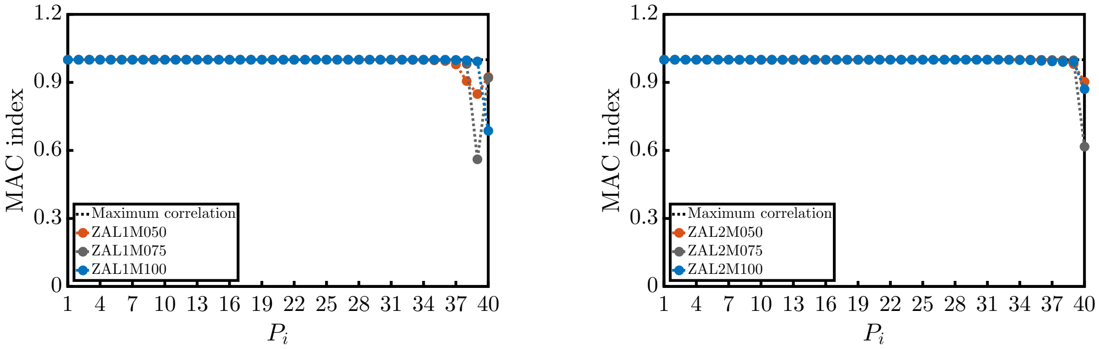

(a) Cylinder ZAL1.

(b) Cylinder ZAL2.

Figure 5.12: MAC index variation for the first vibration mode.

From Figure 5.12, the first vibration mode for all evaluated cylindrical shells is characterized by a smooth transition from one load step to the next until the vicinity of buckling. Between the load steps 37 and 39, which are corresponding to 92.5% and 97.5% of P_{NL}, respectively, the MAC index indicates a change in the shape of the vibration modes. These load levels are close to the buckling load coinciding with the region in which the geometric nonlinearities start to dominate the behavior of the cylinders.

Figure 5.13 shows a comparison between the first vibration mode of ZAL1M050 at the following load levels: (a) unloaded condition, (b) nonlinear buckling load P_{NL}, and (c) first stable increment in the postbuckling regime P_{PB}. Similar results were found for the other cylindrical shells; therefore, Table 5.7 presents the magnitudes of the first natural frequency for all simulated cylinders considering the aforementioned load steps.

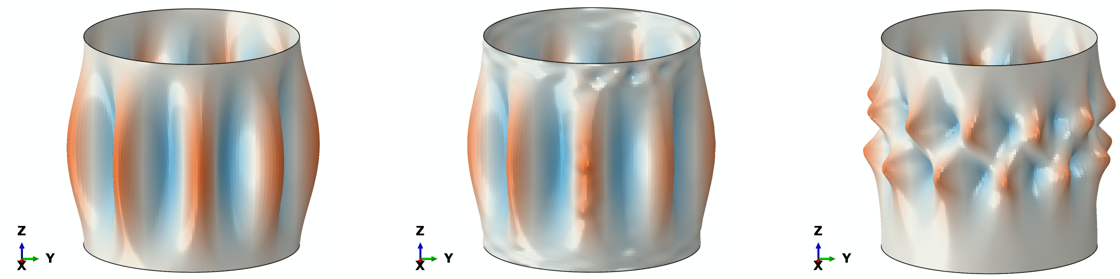

(a) Unloaded condition (250.65 Hz).
(b) Nonlinear buckling load (167.84 Hz).
(c) Postbuckling regime (53.84 Hz).

Figure 5.13: First vibration mode at different load levels for ZAL1M050.

Table 5.7: First natural frequency at the unloaded condition, P_{NL}, and P_{PB}.

Cylinder	$\boldsymbol{F_1}$ **[Hz]**	$\boldsymbol{\bar{F}_1}$ **at** $\boldsymbol{P_{\mathrm{NL}}}$ **[Hz]**	$\boldsymbol{\bar{F}_1}$ **at** $\boldsymbol{P_{\mathrm{PB}}}$ **[Hz]**
ZAL1M050	250.65	167.84	53.84
ZAL1M075	250.65	176.26	57.74
ZAL1M100	250.65	189.02	73.50
ZAL2M050	126.43	84.55	33.65
ZAL2M075	126.43	87.05	27.93
ZAL2M100	126.43	92.88	23.94

Evaluating Figure 5.13(a) and (b), a detectable variation on the first vibration mode, associated with a reduction of 32.97% in the frequency magnitude, is observed. In Figure 5.13(c), the number of half-waves in the axial direction has changed, which does not allow following the same vibration mode beyond buckling. From Table 5.7, the magnitude of the first natural frequency at P_{NL} increases as the KDF from Table 5.6 decreases being not zero for all investigated cylinders.

The postprocessed results for the first natural frequency are shown in Figure 5.14. The charts concern the frequency variation up to the load step associated with the buckling load P_{NL}. Moreover, they are presented considering the classic characteristic chart in Figure 5.14(a) and (c), and in the modified characteristic chart [35] in Figure 5.14(b) and (d), for ZAL1 and ZAL2, respectively. The analytical solutions are based on Equation (2.1), as demonstrated in Section 4.2.

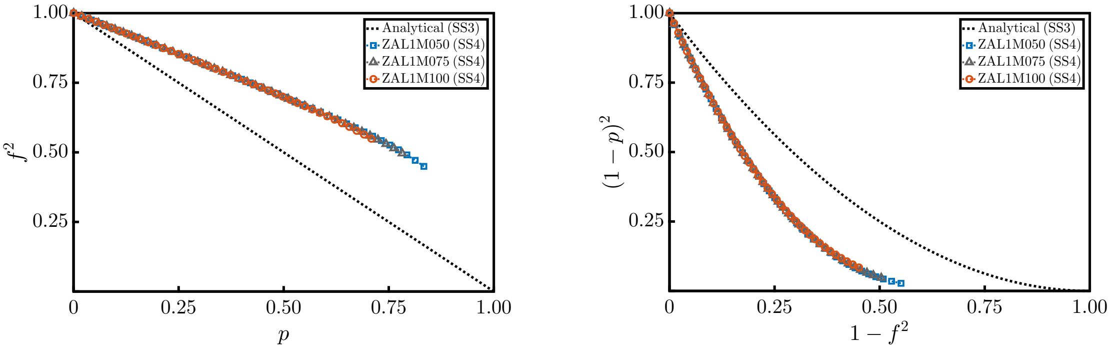

(a) Classic characteristic chart (ZAL1). **(b)** Modified characteristic chart (ZAL1).

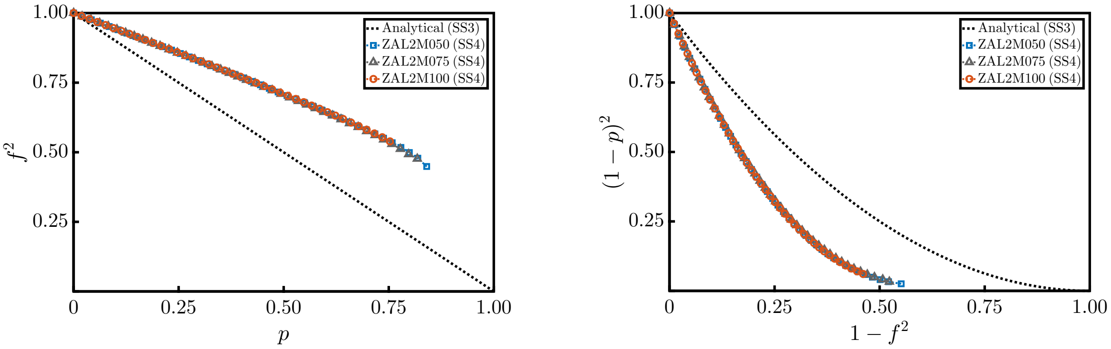

(c) Classic characteristic chart (ZAL2). **(d)** Modified characteristic chart (ZAL2).

Figure 5.14: First natural frequency variation of ZAL1 and ZAL2.

Analyzing Figure 5.14(a) and (c), which are based on the classic characteristic chart, an extrapolation of a linear best-fit equation to the abscissa would overestimate the buckling load. On the other hand, regarding the results presented in the modified characteristic chart [35], a nonlinear relationship that holds the second-order shape is observed, see Figure 5.14(b) and (d); additionally, the minimum magnitudes of $(1-p)^2$ are positive likely culminating in realistic estimations of ξ^2.

5.5 VCT applied to the numerical results

In Section 5.4, numerical models of ZAL1 and ZAL2 are simulated for three imperfection magnitudes up to their respective buckling loads P_{NL}. These results are taken into account up to a load level corresponding to 97.5% of P_{NL} for predicting the buckling load through the VCT. The method is applied following the steps described in Chapter 4, considering the load levels normalized by P_{CR} calculated for SS4 boundary conditions (70.18 kN as given in Table 5.3).

The VCT is evaluated in a convergence study, which simultaneously increases the maximum load level P_{MAX} and the number of load steps. This analysis indicates an appropriate P_{MAX} for the VCT experiment since P_{MAX} is more relevant than the number of load steps for the accuracy of the estimation [92]. Figure 5.15 shows the deviation δ_{NL} between the VCT predicted buckling load P_{VCT} and P_{NL} (as related to P_{NL}) in terms of P_{MAX} (as a percentage of P_{NL}); moreover, the charts highlight a tolerance of ±10%.

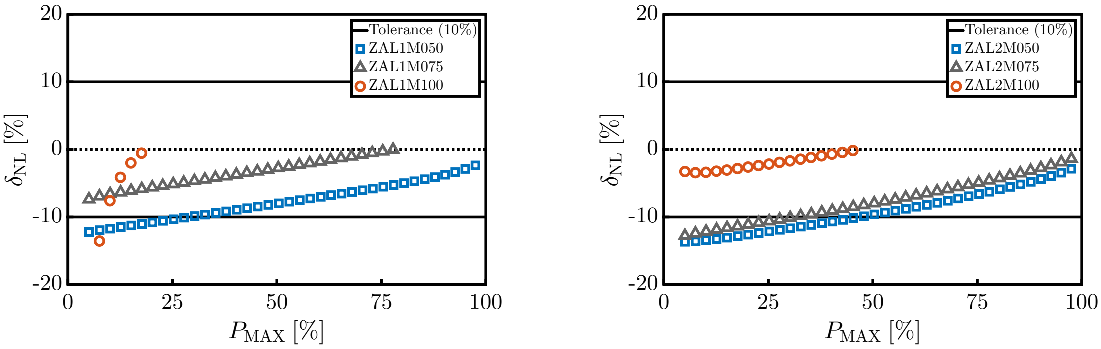

(a) Cylinder ZAL1.

(b) Cylinder ZAL2.

Figure 5.15: Convergence of the deviation for the VCT predictions.

From Figure 5.15, the VCT provides appropriate and conservative estimations for all cylindrical shells, i.e., characterized by δ_{NL} converging from negative values. This is true even when the VCT is evaluated for low maximum load levels far from the actual buckling load once the magnitudes of the deviations are below 10% for most of the estimations. Additionally, the methodology provides better estimations at lower maximum load levels for greater magnitudes of the initial imperfections.

Towards assessing the nondestructive nature and the applicability of the methodology, the results from Figure 5.15 are summarized in Table 5.8. Two approaches are considered: (1) including all load steps up to the maximum load level associated with the minimum δ_{NL}, and (2) including all load steps up to 50% of P_{NL}. For both cases, the maximum load level of the VCT estimations P_{MAX} (as a percentage of P_{NL}), the VCT estimations P_{VCT}, and deviations δ_{NL} (as related to P_{NL}), are presented.

Furthermore, Figure 5.16 shows the frequency variation up to the corresponding P_{MAX} with the respective best-fit curves for all cases of Table 5.8. Observe that the legend of the charts brings the associated coefficient of determination R^2_{S} and the estimated ξ^2. The high magnitudes obtained for R^2_{S} confirm the goodness of fit of the quadratic equation endorsing it as an appropriate model in the presence of SS4 boundary conditions and measured mid-surface imperfections with different magnitudes.

Table 5.8: Summary of the VCT predictions of the numerical assessment.

	Minimum deviation			**Up to 50% of P_{NL}**		
Cylinder	P_{MAX} [%]	P_{VCT} [kN]	δ_{NL} [%]	P_{MAX} [%]	P_{VCT} [kN]	δ_{NL} [%]
ZAL1M050	97.5	57.14	-2.4	50.0	53.70	-8.2
ZAL1M075	77.5	54.88	-0.0	50.0	53.24	-3.0
ZAL1M100	17.5	49.46	-0.6	-	-	-
ZAL2M050	97.5	57.28	-2.9	50.0	53.13	-9.9
ZAL2M075	97.5	56.59	-1.4	50.0	52.66	-8.2
ZAL2M100	45.0	52.76	-0.2	-	-	-

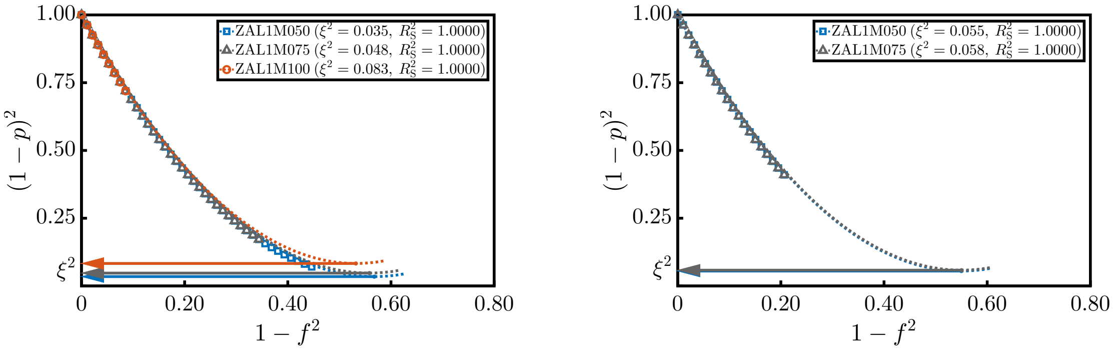

(a) Cylinder ZAL1 (minimum deviation). **(b)** Cylinder ZAL1 (up to 50% of P_{NL}).

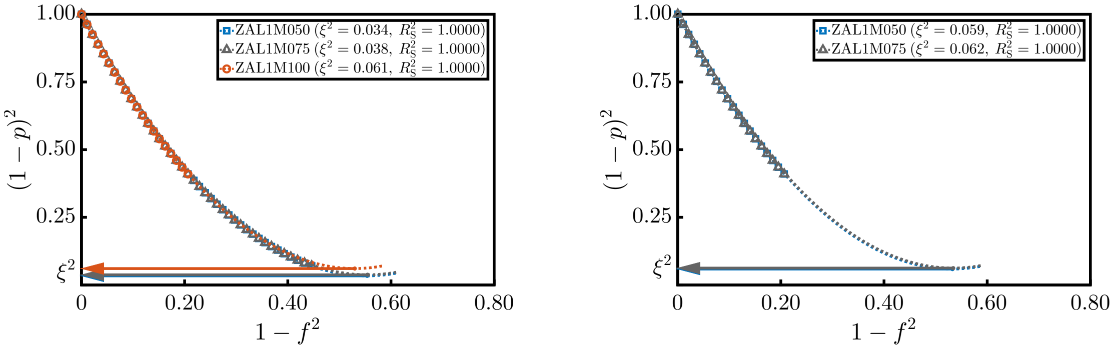

(c) Cylinder ZAL2 (minimum deviation). **(d)** Cylinder ZAL2 (up to 50% of P_{NL}).

Figure 5.16: VCT implementation for the numerical assessment.

Analyzing Table 5.8 for the first study, represented in Figure 5.16(a) and (c), the VCT estimations are conservative and in excellent agreement with the corresponding values from Table 5.6 being the greatest deviation magnitude of 2.9%. Nevertheless, a residual deviation is identified for cylindrical shells with smaller magnitudes of the initial imperfection even for 97.5% of P_{NL} as the maximum load level, for instance, see the results of ZAL1M050, ZAL2M050, and ZAL2M075.

Concerning the second study, note in Figure 5.16(b) and (d) that the estimated KDFs are similar for the different magnitudes of geometric imperfections. Yet, the results are conservative and in good agreement with deviation magnitudes in the range between 3.0% and 9.9%. This range of deviation for low maximum load levels supports the applicability of the method as a truly nondestructive experimental procedure for predicting the buckling load of the theoretical unstiffened cylindrical shells.

5.6 Summary and conclusions

This chapter assessed the effects of geometric nonlinearities and different boundary conditions on the methodology verified in Chapter 4 through a numerical study comprising two theoretical isotropic cylindrical shells. Firstly, the cylinders are represented by reference FE models considering the same boundary conditions of the analytical solution presented in the mentioned chapter. Subsequently, these models are verified by direct comparison with the analytical results.

The numerical models are then extended for SS4 boundary conditions and had their meshes disturbed by a measured mid-surface imperfection available in [108]. For a better understanding of the effects of the initial imperfections, the original measurement is downscaled, taking into account three maximum magnitudes: 50%, 75%, and 100% of the shell thickness for both cylinders. These models are employed to simulate the vibration response of the cylindrical shells under axial loading.

For the numerical assessment, 41 load steps, including the buckling load and the first stable increment in the postbuckling regime, are defined. The numerical vibration modes are analyzed through an algorithm based on the MAC. This procedure allows the evaluation of a high density of load steps resulting in a thorough analysis of the variation of the natural frequencies and vibration modes as related to the axial loading and inherent nonlinearities.

These results could be reproduced before a VCT test, helping to define the maximum axial load level and the number of load steps needed for a reliable prediction. Such a simulation would assess different combinations of the number of load steps and maximum load level addressing the feasibility of the VCT experiment. Hence, a sufficient number of load steps to be measured and a maximum load level would be determined, ensuring a truly nondestructive procedure within a reasonable time frame.

The numerical results are postprocessed to evaluate the VCT in two different approaches: (1) minimizing the deviation between the VCT estimation and the nonlinear buckling load, and (2) exploring load steps up to 50% of the nonlinear buckling load. Notably, the second approach meant to strengthen the practicality of the method verified in Chapter 4 as a nondestructive experimental procedure for predicting the buckling load of the simulated unstiffened cylindrical shells.

Within the proposed study, the predicted buckling loads P_{VCT} are in high-grade agreement when load levels up to 97.5% of P_{NL} are contemplated (the error is between -0.0% and -2.9%). All estimations for the entire range of load levels are conservative, i.e., associated with negative deviations. Considering load levels up to 50% of P_{NL}, the method is acceptable as the deviation magnitudes are below 9.9%; furthermore, the convergence is faster for smaller magnitudes of the KDF, as observed in Figure 5.15.

6 Experimental validation

This chapter presents the experimental work of this thesis, which is focused on extending the applicability and the robustness of the VCT empirically formulated in [35] and analytically verified in Chapter 4. Altogether, five cylindrical shells were tested, exploring different design details, test set-ups, and loading conditions. According to the test specimens, the work is split into three main test campaigns being each one composed of buckling and a sequence of vibration experiments.

Section 6.1 provides a complete overview of these specimens showing the geometric and material properties and the measurements for characterizing the cylindrical shells. The evaluation of the VCT approach requires the first linear buckling load P_{CR} as a reference for calculating the load ratio p. Therefore, Section 6.2 shows the convergence analyses and the first linear buckling load for the reference FE model based on the measured characteristics of each cylinder.

After that, Section 6.3 brings the description of the three buckling test facilities employed during the three experimental campaigns. Two of them are located at the DLR Institute of Composite Structures and Adaptive Systems and the other one at the TU Delft Faculty of Aerospace Engineering. Afterward, Section 6.4 summarizes the results of the buckling and vibration experiments for each one of the cylindrical shells under all tested configurations.

Finally, the mentioned experimental results are evaluated in Section 6.5, further validating the methodology discussed in this thesis. The variation of the first natural frequency for each cylinder is used for predicting its corresponding *in-situ* buckling load. Apart from this, additional aspects of the methodology were experimentally investigated, such as the number of load steps and the maximum load level considered for an appropriate estimation and the goodness of fit of the second-order equations.

6.1 Overview of the cylindrical shells

This study concerns five cylindrical shells with different geometric and material properties. The specimens, named Z38, ZD27, ZD28, ZD29, and Z42, are described in the following subsections.

6.1.1 Cylinder Z38

The specimen Z38 is a metallic orthotropic skin-dominated cylinder consisting of a milled panel with 126 closely spaced integral blade stiffeners bent to form the cylindrical shell. The structure is made of aluminum alloy AL7075-T7351 (characterized in Table 5.2), and the joint edge was welded using an electron beam based process [95]. Table 6.1 presents the geometric characteristics, and Figure 6.1 shows an isometric view of the structure and detailed views of the stiffeners and welding seam.

Table 6.1: Geometric characteristics of Z38 [95].

Description	**Magnitude [mm]**
Free length L (total length)	960 (1000)
Outer surface best-fit radius R	400.38
Thickness of the skin h	0.55
Height of the stiffener H_{ST}	5.20
Thickness of the stiffener h_{ST}	0.55
Distance between stiffeners b	19.97

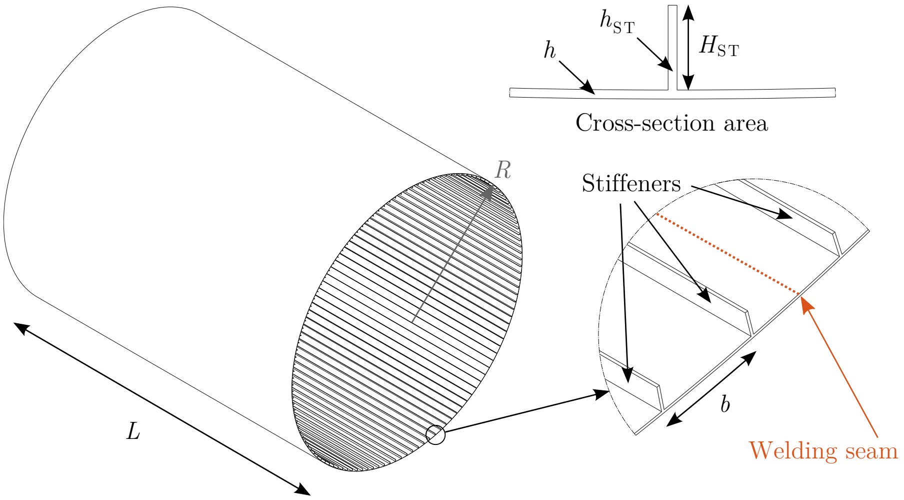

Figure 6.1: Isometric and detailed views of Z38 with design details [95].

Considering the boundary conditions, the cylindrical shell was potted into circular steel rings with 20 mm in height using an epoxy resin mixed with quartz powder. The end plates ensure circular cross-sections, and the hardening of this mixture with 20 mm depth ensures the bond between the structure and the metallic rings. Figure 6.2 shows (a) an overview of the cylinder potted into the steel rings and (b) a detailed view of the upper steel ring.

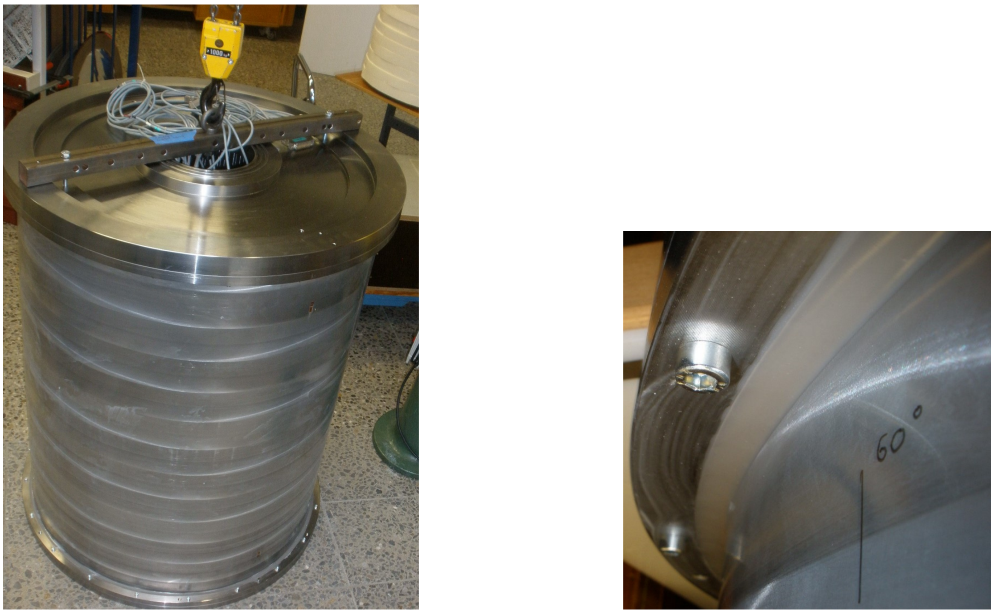

(a) Overview of the potted cylindrical shell. **(b)** Detailed view of the upper steel ring.

Figure 6.2: Z38 potted into the metallic end plates [95].

Before the experimental campaign, a digital image correlation (DIC) system based on photogrammetry, named ATOS® [15], was used for measuring the outer surface deviations of the potted cylindrical shell. These measurements allow an assessment of the quality of the specimen and the calculation of the ideal best-fit cylinder along with the corresponding outer surface best-fit radius of Table 6.1. Figure 6.3 presents the measured deviations as related to the calculated best-fit cylinder.

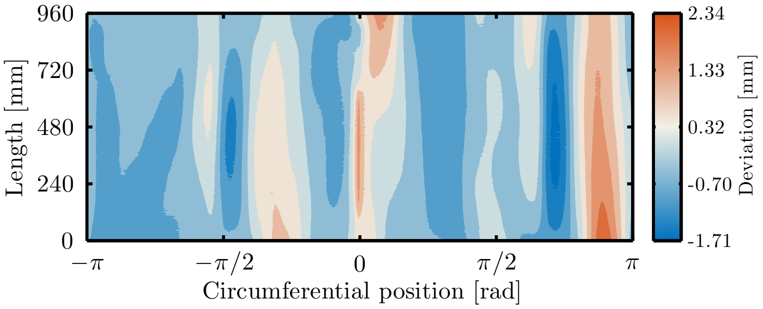

Figure 6.3: Measured mid-surface imperfection of Z38.

6.1.2 Cylinders ZD27, ZD28, and ZD29

The specimens ZD27, ZD28, and ZD29 concern three nominally equal unstiffened composite laminated cylindrical shells manufactured at the DLR Institute of Composite Structures and Adaptive Systems [97]. The cylinders were fabricated by hand-layup using four plies of the unidirectional prepreg IM7/8552 Hexcel® and the same mold. Figure 6.4 presents the described structures, and Table 6.2 shows the geometric characteristics (measured and nominal magnitudes).

(a) Cylinder ZD27. **(b)** Cylinder ZD28. **(c)** Cylinder ZD29.

Figure 6.4: Specimens ZD27, ZD28, and ZD29 [97].

Table 6.2: Geometric characteristics of ZD27, ZD28, and ZD29 [97].

Description	**Nominal**	**ZD27**	**ZD28**	**ZD29**
Free length (total length) [mm]	560 (600)	560 (600)	560 (600)	560 (600)
Middle surface best-fit radius [mm]	250.00	250.78	250.86	250.87
Average total thickness [mm]	0.50	0.58	0.48	0.52
Layup [°]	$[+45\ -45]_S$	$[+45\ -45]_S$	$[+45\ -45]_S$	$[+45\ -45]_S$

Evaluating Table 6.2, the variations of the geometric characteristics of the cylindrical shells are within a tolerable range for equivalent specimens. Additionally, Table 6.3 shows the mechanical material properties of the unidirectional lamina, considering 0.125 mm as the nominal ply thickness and 60.5% as the fiber volume fraction. These material properties were obtained from previous material characterization tests performed at DLR, available in [111, 112].

Table 6.3: Mechanical material properties of IM7/8552 [111, 112].

E_{11} [GPa]	E_{22} [GPa]	ν_{12}	G_{12} [GPa]	G_{13} [GPa]	$G_{23}{}^{*}$ [GPa]
150.0	9.08	0.32	5.29	5.29	3.41

* Calculated G_{23} using the approximation formula from [113].

Concerning the boundary conditions, equally to Z38, circular steel end plates with 20 mm in height were potted on both edges using the resin mixture. After that, the DIC ATOS® was employed for measuring the outer surface deviations. Figure 6.5 presents these measurements for each one of the specimens as related to the best-fit radii of Table 6.2. The middle surface best-fit radii of Table 6.2 are calculated considering the respective outer surface best-fit radii and average total thicknesses of Table 6.2.

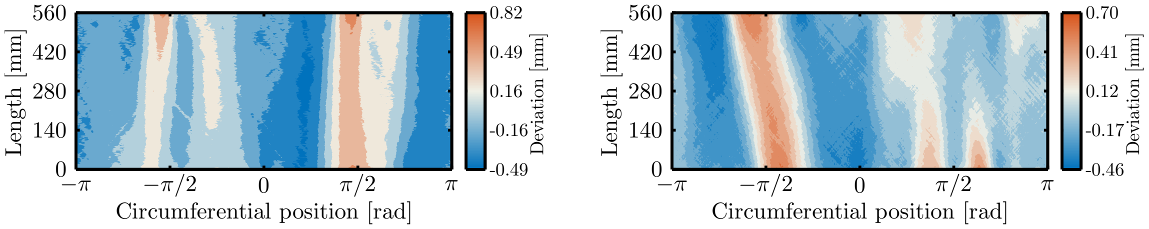

(a) Cylinder ZD27. **(b)** Cylinder ZD28.

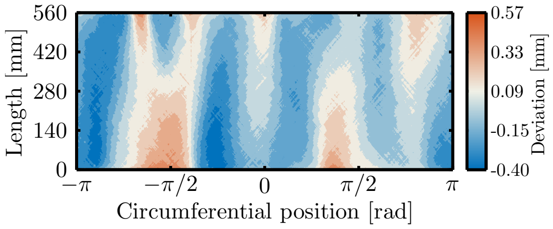

(c) Cylinder ZD29.

Figure 6.5: Measured mid-surface imperfection of ZD27, ZD28, and ZD29.

The manufacturing quality of the composite cylindrical shells was also assessed regarding their thickness variation. The ultrasonic scan employing a 10 MHz probe, which gives a good balance between thickness range and resolution, covered the total surface of the cylinders. The thickness measurements were taken before the described potting procedure. Figure 6.6 shows the ultrasonic scan of each structure, from which the corresponding average total thicknesses were given in Table 6.2.

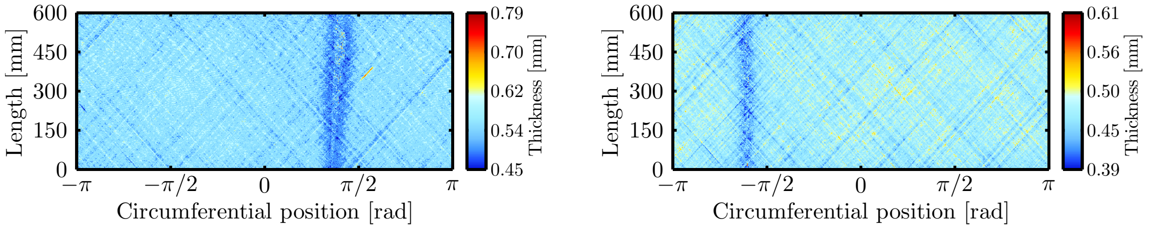

(a) Cylinder ZD27.

(b) Cylinder ZD28.

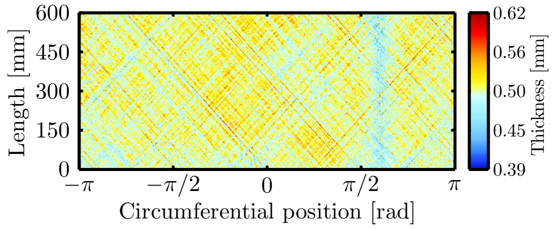

(c) Cylinder ZD29.

Figure 6.6: Measured thickness variation of ZD27, ZD28, and ZD29.

The mechanical material properties of composite materials are calculated based on the fiber volume ratio [114]. Khakimova et al. [115] assumed that the thickness variation is associated with the amount of matrix variation while the amount of fibers remains constant, and recalculated the material properties through composite composition rules. Two equations were deduced for calculating a given material property of the composite material X_{C}:

$$X_{\mathrm{C}} = \frac{h_{\mathrm{NOM}}}{h} X_{\mathrm{C,NOM}} + \left(1 - \frac{h_{\mathrm{NOM}}}{h}\right) X_{\mathrm{M}} \tag{6.1}$$

$$X_{\mathrm{C}} = \frac{X_{\mathrm{M}}}{1 - \sqrt{\frac{h_{\mathrm{NOM}}}{h}} \left(1 - \frac{X_{\mathrm{M}}}{X_{\mathrm{C,NOM}}}\right)} \tag{6.2}$$

where h_{NOM} is the nominal thickness of the laminate, $X_{\mathrm{C,NOM}}$ is the nominal magnitude of the composite material property X_{C}, and X_{M} is the corresponding material property of the matrix. In the study, the authors specified that Equation (6.1) should be used for calculating E_{11} and ν_{12}, while Equation (6.2) should be used for calculating E_{22}, G_{12}, G_{13}, and G_{23}.

Note that Equations (6.1) and (6.2) depend on the thickness ratio and the matrix and nominal composite material properties. The elastic modulus of the matrix, available in [116], is 4,670 MPa, and the Poisson's ratio is assumed 0.30, as suggested in [115]. Moreover, the nominal and average total thicknesses presented in Table 6.2 are considered. Table 6.4 shows the modified material properties, which are used to calculate the linear buckling loads of ZD27, ZD28, and ZD29 in Section 6.4.

Table 6.4: Modified mechanical material properties of IM7/8552.

Cylinder	E_{11} **[GPa]**	E_{22} **[GPa]**	ν_{12}	G_{12} **[GPa]**	G_{13} **[GPa]**	G_{23} **[GPa]**
ZD27	130.82	8.53	0.32	4.67	4.67	3.21
ZD28	155.93	9.26	0.32	5.51	5.51	3.47
ZD29	144.84	8.93	0.32	5.11	5.11	3.36

6.1.3 Cylinder Z42

The specimen Z42 consists of an unstiffened cylinder fabricated by hand-layup using six layers of the unidirectional prepreg 135/HS40/67g NTPT™ [117]. The design based on such thin layers allows the investigation of cylindrical shells that are closer to real launch vehicle structures in terms of the R/h ratio (approximately 1025 for Z42). Figure 6.7 shows the described cylinder, while Table 6.5 presents the measured geometric characteristics and the corresponding nominal values.

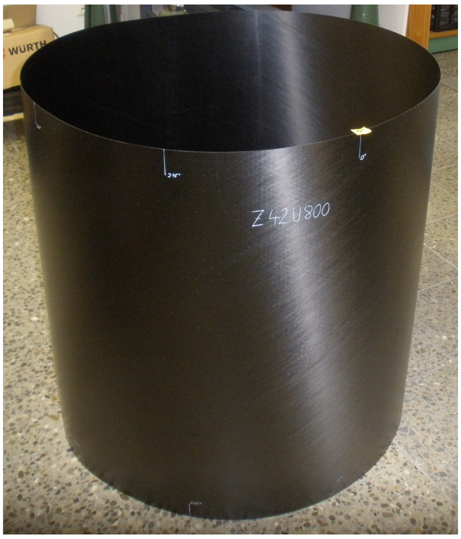

Figure 6.7: Specimen Z42 [117].

Table 6.5: Geometric characteristics of Z42 [117].

Description	**Nominal**	**Z42**
Free length (total length) [mm]	800 (850)	800 (850)
Middle surface best-fit radius [mm]	400.00	400.93
Average total thickness [mm]	0.39	0.36
Layup [°]	[+60 0 -60]$_S$	[+60 0 -60]$_S$

Furthermore, Table 6.6 summarizes the mechanical material properties obtained from a test campaign according to DIN EN 14126, 2561, and 2597 for a specimen with 0.065 mm as nominal ply thickness.

Table 6.6: Mechanical material properties of 135/HS40/67g [117].

$\boldsymbol{E_{11}}$ **[GPa]**	$\boldsymbol{E_{22}}$ **[GPa]**	$\boldsymbol{\nu_{12}}$	$\boldsymbol{G_{12}}$ **[GPa]**	$\boldsymbol{G_{13}}$ **[GPa]**	$\boldsymbol{G_{23}}^*$ **[GPa]**
196.0	7.80	0.25	5.09	5.09	3.20

[*] Calculated G_{23} using the approximation formula from [113].

Analyzing Table 6.5, the average total thickness of Z42 is 7.69% smaller than the nominal magnitude. Assuming that this discrepancy is due to the variation of the amount of matrix, the obtained material properties of Table 6.6 are modified through Equations (6.1) and (6.2). The elastic modulus from [116] and 0.30 as Poisson's ratio are considered once specific information for the resin of the prepreg 135/HS40/67g is not available in [118]. Table 6.7 shows the recalculated material properties.

Table 6.7: Modified mechanical material properties of 135/HS40/67g.

$\boldsymbol{E_{11}}$ **[GPa]**	$\boldsymbol{E_{22}}$ **[GPa]**	$\boldsymbol{\nu_{12}}$	$\boldsymbol{G_{12}}$ **[GPa]**	$\boldsymbol{G_{13}}$ **[GPa]**	$\boldsymbol{G_{23}}$ **[GPa]**
211.94	8.02	0.25	5.50	5.50	3.31

Analogous to Subsection 6.1.2, the thickness measurement, shown in Figure 6.8, was performed through the same ultrasonic scan taking into account the already delineated configuration. As described for the other specimens, the cylinder Z42 was also potted into metallic rings using the same resin mixture. However, as in-plane imperfections were prescribed during its experimental campaign, the upper ring, which is split into two parts, has 30 mm in height while the bottom one has 20 mm.

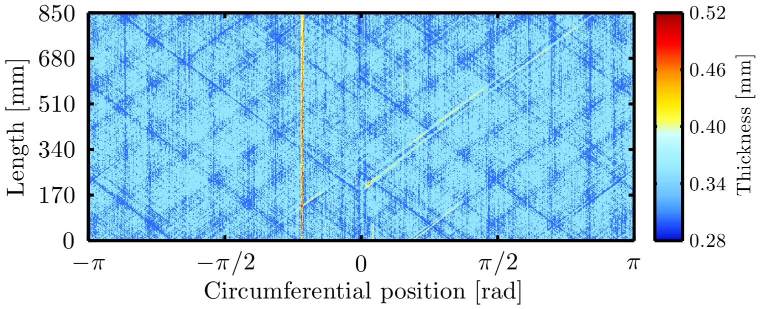

Figure 6.8: Measured thickness variation of Z42.

The two mentioned parts of the upper ring are connected by top flanges through 64 bolts like schematically depicted in Figure 6.9. This design permits including shims between these flanges, forming a desired pattern of in-plane imperfections through the circumference. In Figure 6.10, a top view of the described shim is presented, which has 0.05 or 0.10 mm of thickness, while Figure 6.11 shows the in-plane imperfection pattern implemented during the experimental campaign of Z42.

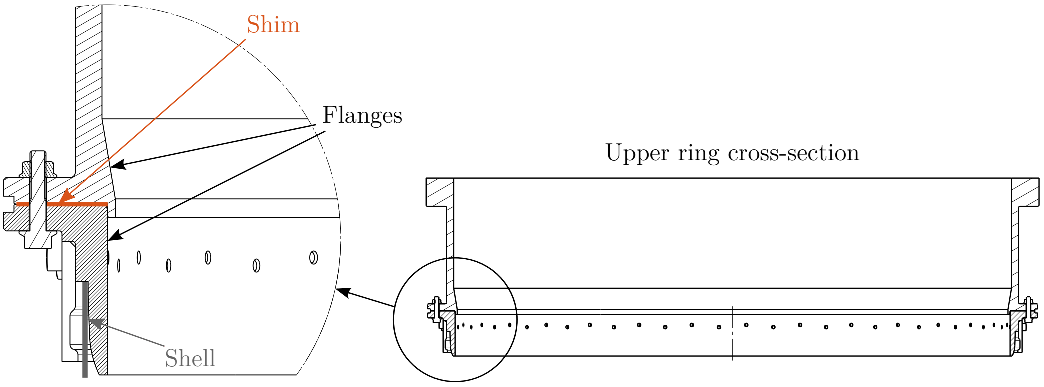

Figure 6.9: Schematic view of the upper ring.

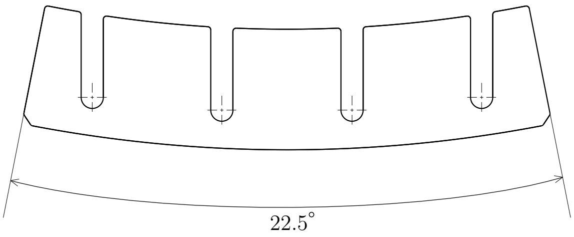

Figure 6.10: Top view of the shim.

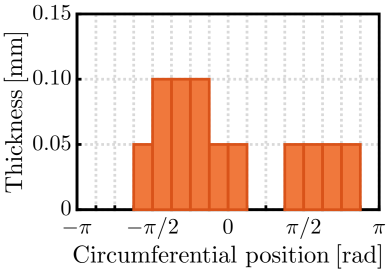

Figure 6.11: Implemented in-plane imperfection of Z42 [117].

For potting the cylindrical shell into the metallic rings, the flanges were firstly tightened in the reference position, i.e., without any shim configuration. This procedure ensured that the expected misalignment between the parts does not affect the desired in-plane imperfection. Subsequently, as performed for the other cylinders, the out-of-plane deviations of the outer surface of the specimen were measured through the DIC ATOS®. Figure 6.12 presents the measured imperfection signature.

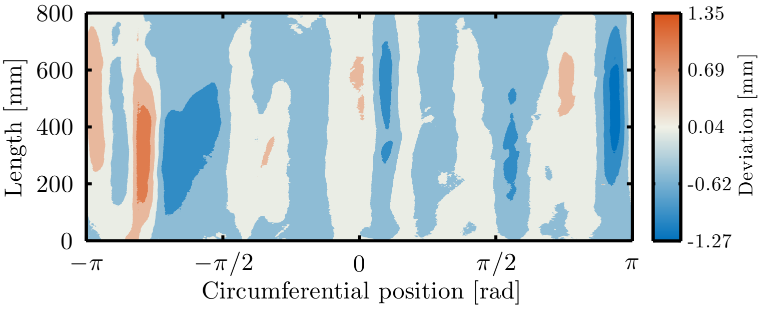

Figure 6.12: Measured mid-surface imperfection of Z42.

6.2 Linear numerical analyses

As itemized in Section 4.4, the implementation of the VCT analytically verified in Chapter 4 requires the first linear buckling load for calculating the load ratio p. Consequently, simplified FE models are determined for obtaining the linear buckling load of the cylindrical shells presented in Section 6.1. The numerical models are pre- and postprocessed through the commercial FE solver Abaqus Standard 6.16® using the default Lanczos algorithm.

The simplified FE models are based on the free length and best-fit radius of the cylinders given in Tables 6.1, 6.2, and 6.5; besides, they assume clamped boundary conditions on both edges. The FE model of Z38 contains linear quadrilateral elements with four nodes, six degrees of freedom per node, and reduced integration (S4R). Differently, the FE models of ZD27, ZD28, ZD29, and Z42 use parabolic shell elements with eight nodes, six degrees of freedom per node, and reduced integration (S8R).

Besides the unpressurized condition, the cylinder Z38 was also tested for three internal pressure levels, i.e., 0.01, 0.02, and 0.03 bar. Thus, a convergence analysis with 126, 252, 378, and 504 elements over the circumference associated with 1, 2, 3, and 4 elements within the stiffener's height, respectively, is performed for each loading condition. The FE models employ the material properties from Table 5.2. Finally, Figure 6.13 shows the convergence of the first buckling load (as related to the finest mesh).

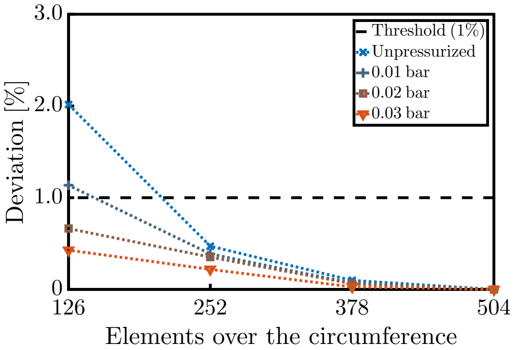

Figure 6.13: Convergence of the first buckling load of Z38.

As presented in Figure 6.13, the mesh with 252 elements over the circumference has an appropriate convergence, that is, the deviation to the finest mesh is below 1%. Figure 6.14(a) depicts the resultant FE model, which contains 36,288 S4R elements associated with 36,792 nodes. Additionally, the inner surface of the cylinder is taken as a reference; hence, the elements associated with the skin include offset avoiding a superposition of the skin and stiffeners cross-section areas as illustrated in Figure 6.14(b).

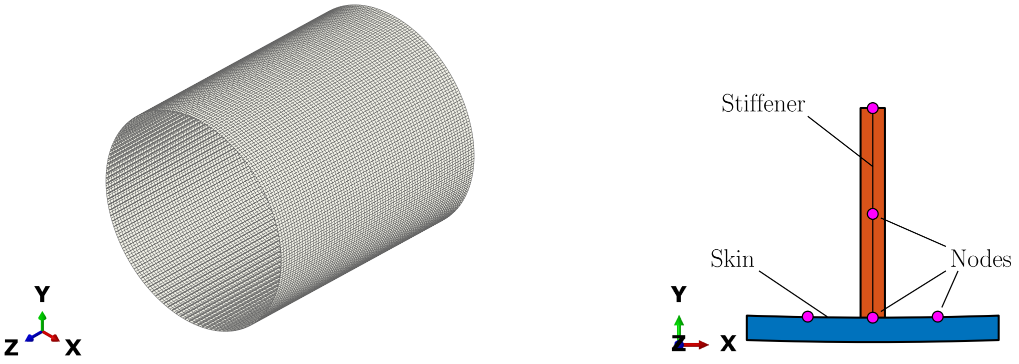

(a) Isometric view of the FE mesh. **(b)** Cross-section area of the shell elements.

Figure 6.14: FE mesh and cross-section area of the shell elements of Z38.

For the composite shells, the FE models are based on the average total thickness and the recalculated material properties from Tables 6.4 and 6.7. The convergence analysis of Z42 investigates 75, 150, 300, and 600 elements through the circumference, whereas the analyses of ZD27, ZD28, and ZD29 investigate 60, 120, 240, and 480. Besides, as Z42 was tested with 0.01 bar of internal pressure, this configuration is also evaluated. Figure 6.15 shows the convergence of the first linear buckling load of the CFRP cylinders.

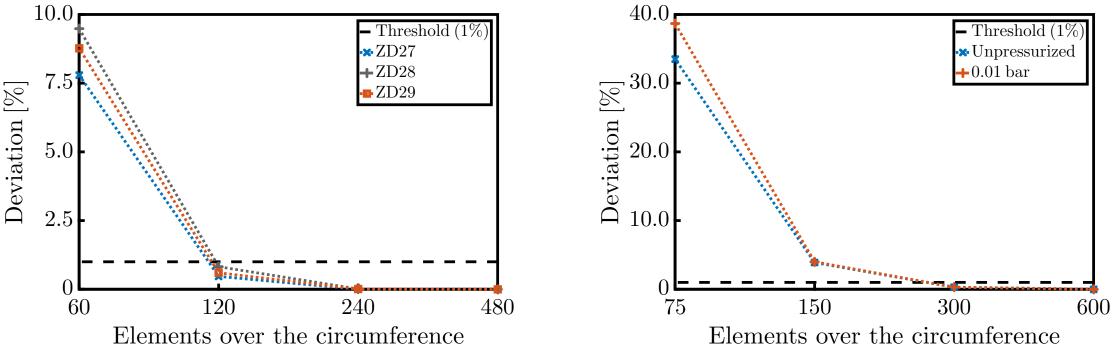

(a) Cylinders ZD27, ZD28, and ZD29. **(b)** Cylinder Z42.

Figure 6.15: Convergence of the first buckling load of the CFRP cylinders.

From Figure 6.15(a) and (b), converged buckling loads (with a deviation to the finest mesh below 1%) are achieved for 120 and 300 elements over the circumference for ZD27, ZD28, and ZD29 and Z42, respectively, whereas in other directions the elements are kept square. Thus, the FE models of ZD27, ZD28, and ZD29 have 5,040 S8R shell elements associated with 15,360 nodes, and the FE models of Z42 have 28,800 S8R shell elements associated with 87,000 nodes. Both described FE meshes are depicted in Figure 6.16.

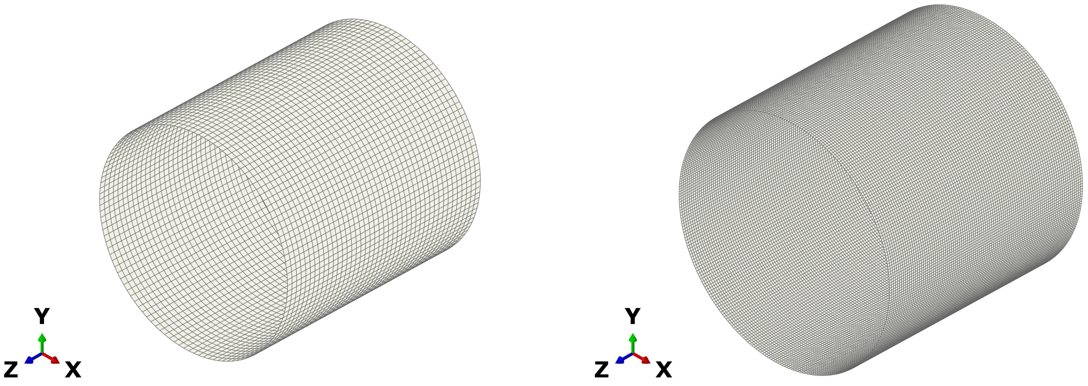

(a) Cylinders ZD27, ZD28, and ZD29. **(b)** Cylinder Z42.

Figure 6.16: FE meshes of the CFRP cylinders.

The above-described FE models are used for calculating the linear buckling loads of the perfect cylindrical shells P_{CR}. The simulations take into account the internal pressure levels p_{INT} when appropriate, i.e., for Z38 and Z42, and fully clamped boundary conditions. Table 6.8 summarizes the linear numerical results for the first buckling load, which are employed in Section 6.5 to calculate the load ratio p for the VCT assessment of the experimental campaigns.

Table 6.8: First linear buckling load of the cylindrical shells.

Cylinder	$\boldsymbol{p_{\mathrm{INT}}}$ **[bar]**	$\boldsymbol{P_{\mathrm{CR}}}$ **[kN]**
Z38	-	109.46
	0.01	120.83
	0.02	130.66
	0.03	139.70
ZD27	-	27.40
ZD28	-	22.46
ZD29	-	24.33
Z42	-	21.58
	0.01	23.32

6.3 Test facilities and test set-ups

This section describes the three buckling test facilities and corresponding test set-ups employed during the experimental campaigns presented in this thesis.

6.3.1 DLR static buckling test facility

The experimental campaigns of the specimens Z38 and Z42 were performed in one of the buckling test facilities at the DLR Institute of Composite Structures and Adaptive Systems. The test rig consists of an axially supported top plate and a lower drive plate activated by a servo-controlled hydraulic cylinder. Between the top plate and the cylindrical shell, a load distributor was placed to ensure an equal force distribution between three load cells, which were used for measuring the applied load.

Moreover, a thin layer of epoxy concrete—epoxy resin reinforced with quartz sand—was added to the interface between the lower drive plate and the specimen. This layer overcomes any further misalignment and encloses the structures' volume for applying the internal pressure. More details of the mentioned test facility and its established procedures for buckling tests are published in [119–121]. Figure 6.17 presents an overview of the cylinders Z38 and Z42 positioned in the test facility.

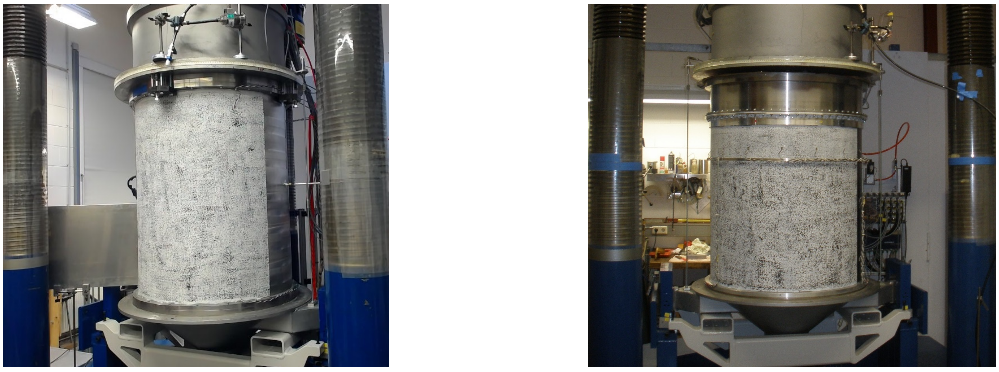

(a) Cylinder Z38. **(b)** Cylinder Z42.

Figure 6.17: Z38 and Z42 positioned in the DLR static buckling test facility.

Considering the loading procedure during the buckling and vibration tests, firstly, when applicable the specimens were loaded with internal pressure, which was applied at a constant rate of 0.03 bar/min from zero to the desired magnitude. A closed-loop control system was used for applying the internal pressure conserving the desired level constant during the axial loading and the vibration tests. Figure 6.18 depicts the schematic representation of the pressure control system.

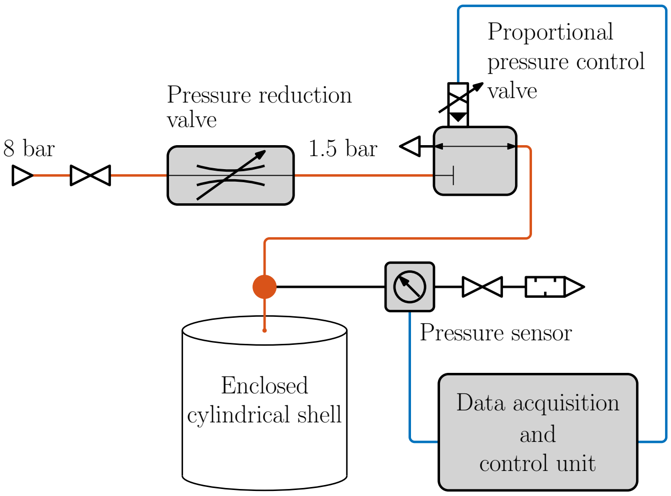
Proportional pressure control valve
Pressure reduction valve
8 bar
1.5 bar
Pressure sensor
Enclosed cylindrical shell
Data acquisition and control unit

Figure 6.18: Schematic representation of the pressure control system [95].

Afterward, the specimens were loaded in compression using displacement control at a constant velocity of 0.12 mm/min. For the buckling tests, the load was applied until buckling took place and smoothly removed after that. Concerning the VCT experiments, the movable lower drive of the machine was held in place at the desired load levels, and the vibration tests were performed through a mechanical shaker connected by a rod and a laser scanning vibrometer.

The cylindrical shells were excited by a pseudo-random signal, and the laser scanning vibrometer, which measures the vibration response in terms of velocity, was positioned covering a segment of the specimen surface. For Z38 and Z42, the segments were defined by an arc length of 459 and 350 mm, a height of 768 and 550 mm, and a mesh with 99 and 77 measured points, respectively. The described grids of measured vibration points are shown in Figure 6.19.

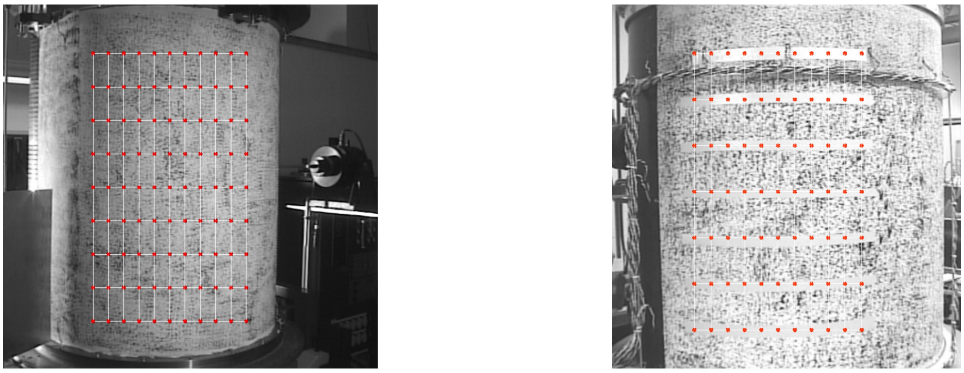

(a) Cylinder Z38. **(b)** Cylinder Z42.

Figure 6.19: Grids of the measured vibration points of Z38 and Z42.

At least three measurements per measured point were taken for averaging the vibration response signals. Furthermore, a frequency band from 0 to 200 Hz and 800 spectral lines were assumed, resulting in a frequency resolution of 250 mHz. The signals were measured and postprocessed through the Polytec® software, in which a modal analysis was performed for characterizing the dynamic behavior of the cylindrical shells, i.e., the vibration modes and respective natural frequencies.

6.3.2 DLR dynamic buckling test facility

The VCT experimental campaigns of ZD28 and ZD29 were performed in the dynamic buckling test facility at DLR [97]. The test rig consists of a lower base plate with a load releasing structure on the bottom of the test rig and a top drive unit activated by a linear electric actuator. This load introduction unit is guided by linear bearings at three positions so that the only possible translation is along the axial direction of the cylinder; additionally, it acts as a load distributor to ensure an equal force distribution.

Below the load releasing structure, three load cells were mounted measuring the applied axial load. The relative displacement of the load introduction unit to the load releasing structure was also measured by three displacement sensors placed equally distributed around the circumference of the cylinder. Furthermore, a thin layer of epoxy concrete was placed between the lower end plate and the load releasing structure and between the top end plate and the load introduction interface.

Identically to the test set-up of Z38, these layers consist of epoxy resin reinforced with quartz sand, and the objective of such a procedure is to reduce any additional misalignment between the test rig and the specimen. Figure 6.20 presents two pictures of the test set-up prepared for ZD28 being (a) the cylindrical shell positioned in the test facility for a buckling test, and (b) a detailed view of the mechanical shaker coupled with the cylinder for a vibration test.

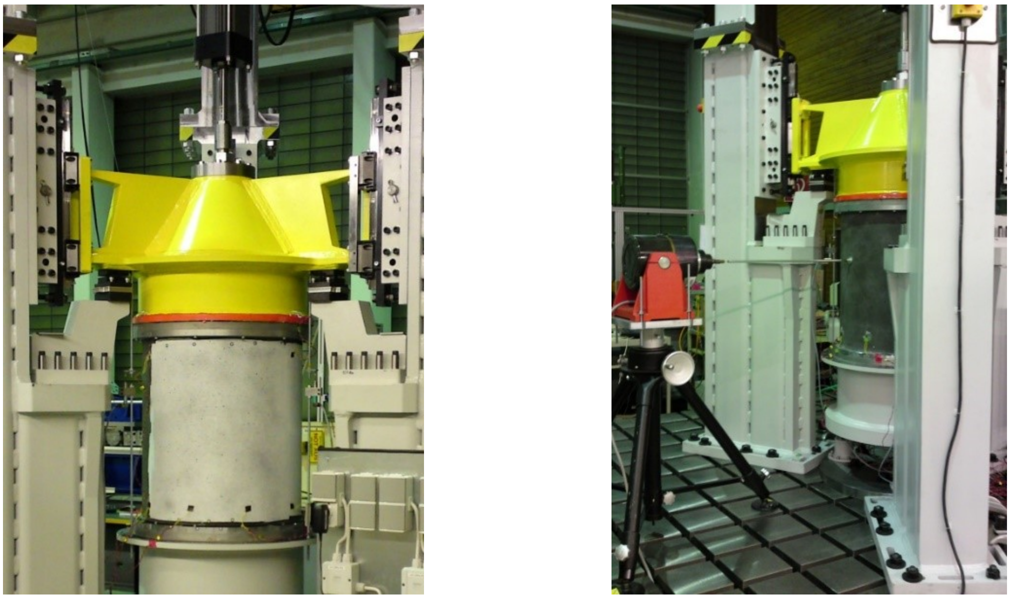

(a) Cylinder positioned in the test facility for a buckling test.

(b) Detailed view of the mechanical shaker coupled with the cylinder.

Figure 6.20: ZD28 positioned in the DLR dynamic buckling test facility.

Besides the mechanical shaker presented in Figure 6.20(b), the test set-up also considered a laser scanning vibrometer; observe that both were also used in the test set-ups described in Subsection 6.3.1. Displacement control was used to apply the axial load at a 0.8 mm/min rate. For the vibration tests of the axially loaded cylinders, the top drive plate was held at each desired load level, whereas for the buckling tests the load was applied until buckling took place.

The cylindrical shells were excited with a pseudo-random signal and two different test configurations were defined for the cylinders ZD28 and ZD29, respectively. For the first, 77 points were designated for measuring the vibration response with a frequency band of 2 kHz and a frequency resolution of 312.5 mHz. For the second, 171 points were considered for measuring the vibration response with a frequency band of 1 kHz and a frequency resolution of 156.25 mHz.

The actual vibration measurements are contaminated by random and bias noises. The random noise is completely filtered out by averaging the signal [109], while bias errors, such as nonlinearities, leakage, and mass loading, are not affected by this procedure. Thus, for both test configurations, at least three measurements were taken for averaging the vibration response signals. Figure 6.21 depicts the grids of measured vibration points of the cylinders ZD28 and ZD29.

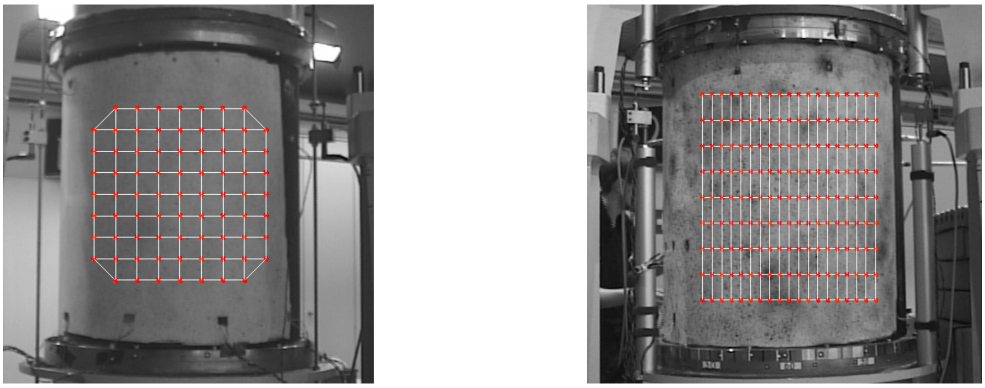

(a) Cylinder ZD28.

(b) Cylinder ZD29.

Figure 6.21: Grids of the measured vibration points of ZD28 and ZD29.

6.3.3 TU Delft buckling test facility

The specimen ZD27 was tested for buckling and vibration at different load levels at the TU Delft Faculty of Aerospace Engineering. The test set-up considers an MTS 3500 servo-hydraulic test machine; moreover, the cylindrical shell was placed between the base plate and the movable plate of the machine. Two linear variable differential transformer (LVDT) sensors measured the axial shortening on both sides of the cylinder [97]. Figure 6.22 shows an overview of ZD27 positioned for the tests.

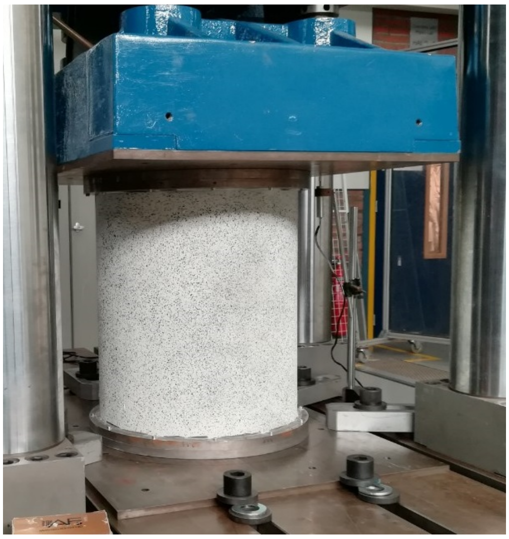

Figure 6.22: ZD27 positioned in the TU Delft buckling test facility.

For the buckling and vibration experiments, the cylinder was loaded in axial compression with displacement driven test mode. The displacement speed was set to 0.2 mm/min with a preload of 1 kN. The load was applied up to the instability of the structure for the buckling test. Concerning the vibration tests, the natural frequencies of the cylindrical shell were measured at various load levels through a test set-up consisting of a laser scanning vibrometer and a loudspeaker.

Over the shaker, the loudspeaker has some advantages as a uniform excitation and not adding a local interference in the structure. A frequency sweep signal was used for exciting the specimen in the range of interest (between 100 and 400 Hz). Thus, the frequency band was adjusted to 400 Hz, while a frequency resolution of 250 mHz was defined. The cylinder was scanned at 143 points, as given in Figure 6.23, considering four measurements for averaging the vibration signals.

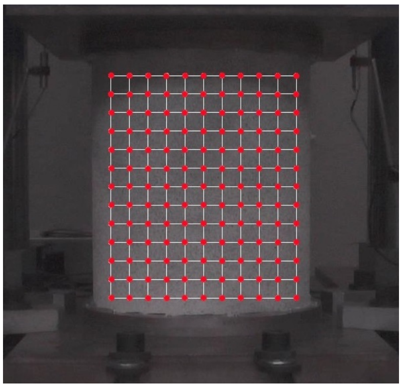

Figure 6.23: Grid of the measured vibration points of ZD27.

6.4 Experimental campaigns

As mentioned before, three main experimental campaigns were performed within the scope of this thesis. A description of the buckling and vibration tests, together with the corresponding experimental results, is provided in the following subsections.

6.4.1 Z38 experimental campaign

The cylinder Z38 was tested for the unpressurized condition and three internal pressure levels p_{INT}, specifically, 0.01, 0.02, and 0.03 bar, which provided a substantial increase in the buckling load within the elastic range. Nevertheless, the vibration tests were conducted before the buckling tests ensuring an intact specimen during all of them [95]. Moreover, before and after each buckling test, measurements of the surface displacements were taken and compared to guarantee no plastic deformations.

Firstly, one buckling test per p_{INT} was performed, and after that, a sequence of ten buckling tests was planned for each p_{INT}. The specimen suddenly failed during the sixth test considering 0.01 bar. Consequently, Table 6.9 shows average buckling loads P_{EXP} for the unpressurized condition and 0.01 bar of p_{INT}, with the respective standard deviations, and the magnitude of a single buckling test for 0.02 and 0.03 bar of p_{INT}. Moreover, the mentioned table also presents the effective KDF γ_{EXP} calculated as $P_{\mathrm{EXP}}/P_{\mathrm{CR}}$.

Table 6.9: Results of the buckling tests of Z38 [95].

p_{INT} [bar]	P_{EXP} [kN]	γ_{EXP}
Unpressurized	86.53±0.083	0.79
0.01	104.36±0.080	0.86
0.02	116.80	0.89
0.03	127.86	0.92

The vibration tests were performed for the unpressurized condition and each p_{INT} at eight compressive load levels P_i. The maximum load level and the number of load steps were chosen based on FE models defined during the planning phase of the experiment. The tests provided the variation of the dynamic behavior, specifically, vibration modes and natural frequencies through the axial loading. Table 6.10 presents the first loaded natural frequency $\bar{F}_1$ at different load steps P_i for each p_{INT}.

Table 6.10: Results of the vibration tests of Z38 [95].

Unpressurized		**p_{INT}: 0.01 bar**		**p_{INT}: 0.02 bar**		**p_{INT}: 0.03 bar**	
P_i [kN]	**$\bar{F}_1$ [Hz]**	**P_i [kN]**	**$\bar{F}_1$ [Hz]**	**P_i [kN]**	**$\bar{F}_1$ [Hz]**	**P_i [kN]**	**$\bar{F}_1$ [Hz]**
14.59	93.50	16.30	105.50	19.24	116.00	20.42	124.25
36.27	86.00	42.84	98.00	46.96	108.50	50.86	117.00
44.29	83.00	65.05	90.50	65.30	103.25	70.54	111.75
62.05	75.50	70.11	88.75	77.38	99.25	85.01	108.00
66.36	73.50	74.18	87.25	82.59	97.25	88.45	106.75
68.04	72.25	76.46	86.50	85.45	96.75	93.43	105.75
70.33	71.25	83.37	83.25	88.47	95.75	96.83	104.25
72.73	69.00	87.30	81.50	92.60	94.50	100.80	103.50

The first vibration mode for all loading conditions of Table 6.10 is associated with one axial half-wave m, directly identified from the measured vibration mode, and nine circumferential waves n, extrapolated from the measurements using the arc length of the grid of the measured points. Figure 6.24 depicts the first vibration mode measured at the first load step for Z38, precisely, 14.59, 16.30, 19.24, and 20.42 kN for the unpressurized condition, and 0.01, 0.02, and 0.03 bar of internal pressure, respectively.

(a) At 14.59 kN unpressurized (93.50 Hz).

(b) At 16.30 kN with 0.01 bar (105.50 Hz).

(c) At 19.24 kN with 0.02 bar (116.00 Hz).

(d) At 20.42 kN with 0.03 bar (124.25 Hz).

Figure 6.24: First vibration mode at the first load step for Z38.

6.4.2 DLR/TU Delft experimental campaign

This experimental campaign comprises buckling and vibration tests performed at two different test facilities. As its first step, ten buckling tests were performed at DLR for validating the nominally identical specimens, i.e., ZD27, ZD28, and ZD29, as equivalent. Table 6.11 gives the results of the ten buckling tests in terms of the average buckling loads P_{EXP} with the corresponding standard deviations and the effective KDFs γ_{EXP} for each cylinder.

Table 6.11: Results of the DLR buckling tests of ZD27, ZD28, and ZD29 [97].

Cylinder	$\boldsymbol{P}_{\text{EXP}}$ **[kN]**	γ_{EXP}
ZD27	20.47±0.007	0.75
ZD28	21.49±0.052	0.96
ZD29	21.86±0.016	0.90

Analyzing Table 6.11, the sets of ten buckling tests were reproducible, and the buckling loads are within an acceptable range of variation corroborating the three specimens as equivalent. Nevertheless, note that ZD28 and ZD29 have greater magnitudes of γ_{EXP} when compared to ZD27. This fact is associated with the modified material properties of the latter mentioned cylindrical shell, which resulted in a greater P_{CR}, for reference, see Table 6.8.

Concerning the VCT tests conducted at DLR, the vibration measurements were performed at six load steps for ZD28 and eleven load steps for ZD29. As a result, the study also experimentally verifies the effectiveness of considering more load steps in the VCT estimations. Figure 6.25 shows the first vibration mode at the first load step for ZD28 and ZD29, while Table 6.12 presents the variation of the first natural frequency $\bar{F}_1$ of each cylinder as related to the respective applied axial load levels P_i.

(a) ZD28 at 0.38 kN (203.13 Hz). **(b)** ZD29 at 0.53 kN (203.75 Hz).

Figure 6.25: First vibration mode at the first load step for ZD28 and ZD29.

Table 6.12: Results of the vibration tests of ZD28 and ZD29 [97].

ZD28		**ZD29**	
$\boldsymbol{P_i}$ **[kN]**	$\boldsymbol{\bar{F}_1}$ **[Hz]**	$\boldsymbol{P_i}$ **[kN]**	$\boldsymbol{\bar{F}_1}$ **[Hz]**
0.38	203.13	0.53	203.75
5.38	194.38	2.96	200.00
10.38	182.81	5.39	195.00
15.38	170.63	7.95	190.00
17.88	165.00	10.41	184.22
20.38	155.31	12.37	180.47
		14.39	175.16
		16.35	170.31
		18.47	164.53
		20.47	157.34
		20.93	153.91

Evaluating Figure 6.25, both vibration modes are similar and associated with one axial half-wave m and nine circumferential waves n—extrapolated from the pictures. Note that the same pair (m, n) was found for the first vibration mode of the other load steps for both cylinders. Furthermore, the magnitudes of the first natural frequency for similar load steps among the specimens are comparable, see Table 6.12. Given these aspects, the different vibration test configurations of ZD28 and ZD29 are equivalent.

The cylinder ZD27 was also tested for buckling at the TU Delft Faculty of Aerospace Engineering to establish a common basis for comparing both test facilities. A sequence of ten buckling tests was planned; however, the specimen failed during the first buckling test. Therefore, Table 6.13 gives the experimental buckling load based on a single buckling test P_{EXP}, the deviation from the DLR equivalent test result δ_{DLR}, and the corresponding effective KDF γ_{EXP}.

Table 6.13: Results of the TU Delft buckling test of ZD27 [97].

Cylinder	$\boldsymbol{P}_{\mathrm{EXP}}$ **[kN]**	$\boldsymbol{\delta}_{\mathrm{DLR}}$ **[%]**	$\boldsymbol{\gamma}_{\mathrm{EXP}}$
ZD27	15.90	-22.33	0.58

Analyzing Table 6.13, the experimental buckling load obtained at the TU Delft is considerably smaller when compared to the DLR average buckling load for the same cylindrical shell, i.e., with a deviation between magnitudes of 22.33%. This discrepancy is likely to be associated with the differences between the test set-ups as, for instance, load asymmetry (reduced in the DLR test arrangement due to the thin layers of epoxy concrete), boundary conditions, among others.

The natural frequencies of the specimen were measured considering a load step of 1 kN starting from 5 kN, except for 12 kN. A lower load level was not measured due to the not completely fixed boundary conditions at low load magnitudes, noticed previously in similar tests. As there was no adhesive paste added between the circular end rings and the support plate of the test machine, the cylinder could not be uniformly pressed without applying a certain load level.

Therefore, this experimental campaign also evaluates if the VCT proposed in [35] is applicable when the natural frequency is not available near the unloaded condition as, e.g., in the experimental campaigns of Z38 and Z42—for the experimental results of Z42, *vide* the next subsection. The first vibration mode is shown at 5 and 6 kN in Figure 6.26 (a) and (b), respectively. Additionally, the variation of the first natural frequency $\bar{F}_1$ with the measured load steps P_i is presented in Table 6.14.

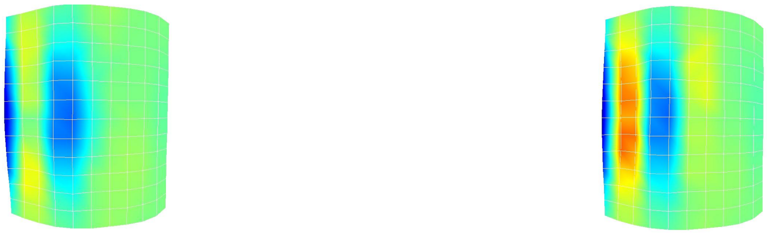

(a) At 5 kN (176.5 Hz). **(b)** At 6 kN (175.0 Hz).

Figure 6.26: First vibration mode at 5 and 6 kN for ZD27.

Table 6.14: Results of the vibration tests of ZD27 [97].

P_i [kN]	$\bar{F}_1$ [Hz]	P_i [kN]	$\bar{F}_1$ [Hz]
5.0	176.5	9.0	167.0
6.0	175.0	10.0	164.0
7.0	171.5	11.0	161.0
8.0	168.5	13.0	153.0

From Figure 6.26, the first vibration mode is slightly different at 5 and 6 kN; note that the first vibration mode resembles Figure 6.26(b) for greater load levels. This discrepancy is most likely associated with the not completely fixed test set-up. Moreover, comparing the frequency magnitudes for similar load levels in Tables 6.12 and 6.14 observe that the results obtained at the TU Delft are much lower, clearly indicating more flexible boundary conditions or non-uniform load distribution.

6.4.3 Z42 experimental campaign

The cylinder Z42 was tested with and without the in-plane imperfection pattern of Figure 6.10; additionally, both test set-ups considered 0.01 bar of internal pressure and the unpressurized condition resulting in four test configurations. Three buckling tests were performed for each described configuration [117]. Table 6.15 presents the results of the three buckling tests in terms of the average buckling loads P_{EXP} with the respective standard deviations and effective KDFs γ_{EXP}.

Table 6.15: Results of the buckling tests of Z42 [117].

Configuration	$\boldsymbol{p}_{\text{INT}}$ **[bar]**	$\boldsymbol{P}_{\text{EXP}}$ **[kN]**	$\boldsymbol{\gamma}_{\text{EXP}}$
Without shims	Unpressurized	12.40±0.058	0.57
Without shims	0.01	15.09±0.135	0.65
With shims	Unpressurized	10.56±0.036	0.49
With shims	0.01	13.25±0.046	0.57

Evaluating Table 6.15, the sets of three buckling tests were reproducible, and the results are within an acceptable range of variation. As expected for a specimen with such an R/h ratio, the KDFs associated with the experimental buckling loads are relatively low. Moreover, note that the effect of the in-plane imperfection on the reference buckling loads (without shims) is a reduction of 14.84% and 12.19% for the unpressurized condition and 0.01 bar of p_{INT}, respectively.

The vibration measurements were performed at six load steps plus the unloaded condition — considering a residual load for keeping the test set-up fixed — for all test configurations. Figure 6.27 presents the first vibration mode at the first load step of each test configuration, being all of them characterized by (m, n) equal to (1, 11), which was also observed for greater load levels. Besides, Table 6.16 shows the variation of the corresponding first natural frequency $\bar{F}_1$ as related to the applied axial load levels P_i.

(a) At 0.76 kN unpressurized without shims (133.50 Hz).

(b) At 1.34 kN with 0.01 bar without shims (170.25 Hz).

(c) At 0.76 kN unpressurized with shims (134.00 Hz).

(d) At 1.23 kN with 0.01 bar with shims (169.50 Hz).

Figure 6.27: First vibration mode at the first load step for Z42.

Table 6.16: Results of the vibration tests of Z42.

Without shims				**With shims**			
Unpressurized		**p_{INT}: 0.01 bar**		**Unpressurized**		**p_{INT}: 0.01 bar**	
P_i [kN]	**$\bar{F}_1$ [Hz]**	**P_i [kN]**	**$\bar{F}_1$ [Hz]**	**P_i [kN]**	**$\bar{F}_1$ [Hz]**	**P_i [kN]**	**$\bar{F}_1$ [Hz]**
0.76	133.50	1.34	170.25	0.76	134.00	1.23	169.50
2.76	132.25	3.76	168.50	2.76	132.25	3.76	167.75
5.76	129.25	6.76	166.25	4.76	130.25	6.76	165.75
6.76	128.00	8.26	165.00	5.76	129.50	8.26	164.50
7.76	126.75	9.76	163.50	6.76	128.00	9.76	163.25
9.76	124.75	11.16	161.75	7.76	126.75	10.76	162.50
10.76	123.00	12.66	160.50	8.76	125.00	11.66	161.00

6.5 VCT applied to the experimental results

Section 6.4 presented the experimental results for the buckling and vibration tests of the cylinders Z38, ZD27, ZD28, ZD29, and Z42. In the present section, these results are evaluated towards extending the applicability of the VCT verified analytically in Chapter 4. The study validates the VCT predictions by comparing them with the corresponding buckling loads obtained from the buckling tests. Furthermore, the steps restated in Chapter 4 are followed as described below:

1. Calculate the first linear buckling load of the perfect structure P_{CR}. This step was carried out through a linear numerical analysis considering clamped boundary conditions. Standard material properties from [107], reproduced in Table 5.2, were employed for Z38, and recalculated ones, presented in Tables 6.4 and 6.7, for ZD27, ZD28, and ZD29 and Z42, respectively. The results for the first linear buckling load are shown in Table 6.8.

2. Assess the first natural frequency variation during axial loading. This step was performed experimentally in different buckling test facilities depending on the specimen, as described in Sections 6.3 and 6.4. The results of the vibration tests are given in Tables 6.10, 6.12, 6.14, and 6.16.

3. Generate the charts $(1-p)^2$ versus $1-f^2$. The load ratio p is calculated as the applied axial load P_i over the first buckling load from the linear numerical models P_{CR} and the frequency ratio f as the first natural frequency at P_i load level $\bar{F}_1$ over the first natural frequency in the unloaded condition. The unloaded condition is not available for the tested specimens; therefore, the corresponding natural frequency at the smallest load level was used.

4. Estimate the second-order best-fit relationship between $(1-p)^2$ and $1-f^2$ through Equation (4.30). The adjusted quadratic equation is then minimized for evaluating the square of the drop of the load-carrying capacity ξ^2, as defined in Equation (4.31).

5. Estimate the buckling load of the structure as established by Souza et al. [87], i.e., using the positive square root of ξ^2 and the first linear buckling load P_{CR} into Equation (2.4).

The experimental data were postprocessed in a Matlab® algorithm and the corresponding characteristic charts are depicted in Figure 6.28. For the sake of simplicity, each chart groups all test results associated with one of the experimental campaigns, for reference, see Section 6.4. Besides the second-order best-fit curves plotted for each test configuration, the legend of the charts contains the respective coefficients of determination R_{S}^2 and minima along the $(1-p)^2$ axis (regarded as ξ^2).

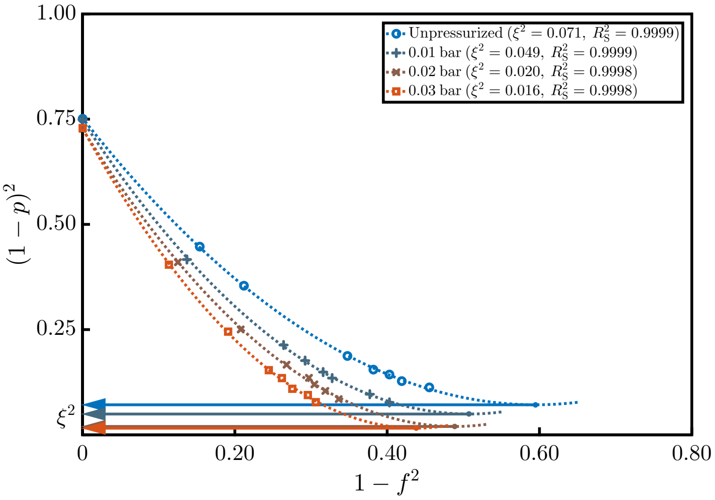

(a) Cylinder Z38.

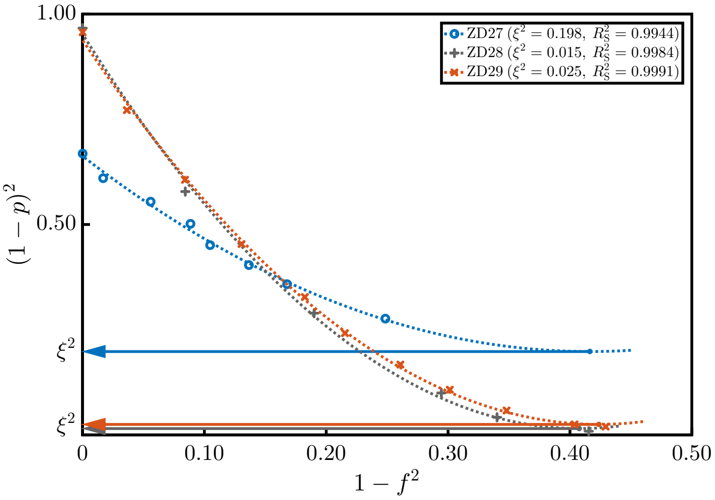

(b) Cylinders ZD27, ZD28, and ZD29.

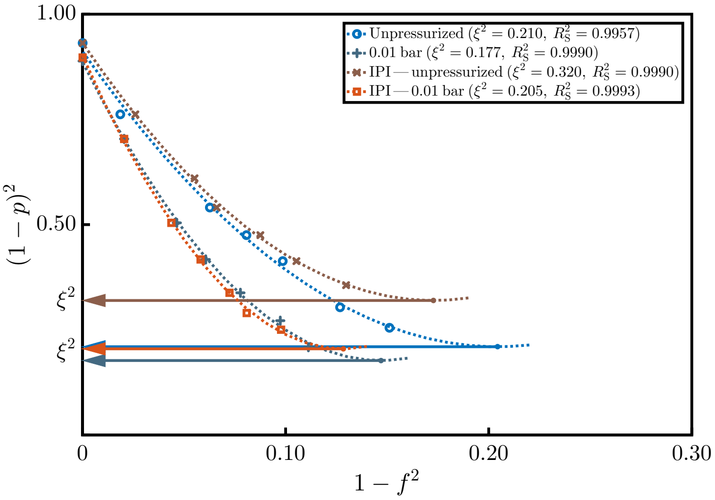

(c) Cylinder Z42.

Figure 6.28: VCT implementation for the experimental campaigns.

Additionally, Table 6.17 presents the estimations of the ξ^2 parameter, the VCT predictions for the experimental buckling loads P_{VCT}, the deviations δ_{EXP} (as related to P_{EXP}), and the maximum load level considered in the VCT estimations P_{MAX} (as a percentage of P_{EXP}). Besides, in the mentioned table, the experimental buckling loads P_{EXP} and their associated KDFs γ_{EXP}, given in Section 6.4, are reproduced for a better assessment of the results.

Table 6.17: Summary of the VCT predictions of the experimental campaigns.

Cylinder	p_{INT} **[bar]**	P_{MAX} **[%]**	P_{EXP} **[kN]**	γ_{EXP}	ξ^2	P_{VCT} **[kN]**	δ_{EXP} **[%]**
Z38	-	84.05	86.53	0.79	0.071	80.23	-7.28
	0.01	83.65	104.36	0.86	0.049	93.99	-9.94
	0.02	79.28	116.80	0.89	0.020	112.28	-3.87
	0.03	78.84	127.86	0.92	0.016	122.22	-4.41
ZD27	-	81.76	15.90	0.58	0.198	15.21	-4.37
ZD28	-	94.85	21.49	0.96	0.015	19.70	-8.33
ZD29	-	95.74	21.86	0.90	0.025	20.48	-6.30
Z42	-	86.77	12.40	0.57	0.210	11.78	-4.99
	0.01	83.90	15.09	0.65	0.177	13.51	-10.49
Z42*	-	82.95	10.56	0.49	0.320	9.45	-10.54
	0.01	88.00	13.25	0.57	0.205	12.76	-3.67

* With the in-plane imperfection presented in Figure 6.11.

From Table 6.17, the VCT is providing consistent estimations for ξ^2 once greater magnitudes are associated with smaller γ_{EXP}. Notably, the adjusted curves are associated with high magnitudes of R_{S}^2 corroborating their goodness of fit, being the smallest 0.9944 for ZD28. These results indicate that the proposed quadratic equation fits the experimental data appropriately. Moreover, as data at 95.74% of P_{EXP} are available for ZD29, the second-order relationship is verified in the vicinity of buckling.

As shown in Table 6.17, the predictions of the VCT are in good agreement with the equivalent experimental results. The smallest and greatest deviation magnitudes, that is, 3.67% and 10.54%, are obtained for Z42 with shims, with 0.01 bar of internal pressure and in the unpressurized condition, respectively. Additionally, for all cylindrical shells, the predicted buckling load is conservative since its magnitude is smaller than the corresponding experimental buckling load.

Particularly, for the experiments of Z38, the smallest deviations, i.e., -3.87% and -4.41%, are associated with the pressurized tests presenting greater KDF magnitudes, with 0.02 and 0.03 bar of p_{INT}, respectively. This aspect indicates that the stabilizing effect of the internal pressure improved the estimations. Furthermore, the method has demonstrated to be truly nondestructive during the mentioned experimental campaign once the maximum applied load level is 84.05% of P_{EXP} for the unpressurized case.

Considering the TU Delft/DLR test campaign, the results provide experimental evidence that the VCT is more suitable for smaller KDF (as numerically verified in Chapter 5). Analyzing the predictions of the three equivalent cylindrical shells, P_{VCT} obtained for ZD27 is in better agreement, although estimated from a relatively smaller maximum load level (81.76% of P_{EXP}). For ZD28 and ZD29, a reliable estimation is associated with a high P_{MAX}, specifically, 94.85% and 95.74% of P_{EXP}, respectively.

Furthermore, the prediction for ZD27 was not affected by the absence of the first natural frequency at a relatively small load level (close to the unloaded condition). Moreover, a significant difference between the estimations of ZD28 and ZD29 is not identified, indicating that the maximum load level—note that the maximum load level for both cylindrical shells is similar—is more effective for reducing the deviation δ_{EXP} than the number of load steps.

Concerning the experimental campaign of Z42, the methodology is first time confirmed for an R/h of approximately 1025 and test conditions closer to real structures (with in-plane induced stresses and internal pressure). The VCT successfully took into account the in-plane imperfections combined with the internal pressure providing a prediction with a deviation of -3.67%. Additionally, as the maximum load level is 88.00% of P_{EXP} for this test condition, the methodology is perceived as truly nondestructive.

6.6 Summary and conclusions

Five cylindrical shells, being one metallic and four composite laminated, were tested towards expanding the practicality of the VCT conceived in [35] and verified analytically herein. For that reason, the experimental campaigns also addressed internal pressure levels and in-plane imperfections, which are often encountered in practical aerospace applications. Moreover, the robustness of the methodology was validated, as three out of the five cylinders were equivalent structures tested in two different test facilities.

The cylindrical shells were manufactured considering processes usually employed in the aerospace industry. Specifically, the composite specimens were fabricated by hand lay-up of the prepreg onto a mandrel and cured in an autoclave, while the metallic one consisted of a milled panel bent to form the cylinder with the joint edge welded by an electron beam based process. Before testing, the structures were potted into circular end plates with a resin mixture ensuring circular cross-sections.

State-of-the-art techniques were used for assessing the initial imperfections of the specimens. The study employed these measurements in the definition of the linear FE models used to calculate the first linear buckling load P_{CR} of each cylinder. The experimental campaigns were performed considering quasi-static loading. For the vibration tests, the axial load was applied up to the desired load levels, whereas for the buckling tests, up to the instability of the structure.

During the experimental campaigns, the first vibration mode was measured at different axial load levels for different test configurations, *vide* Section 6.4. All VCT estimations presented a good correlation when compared to their respective experimental buckling loads once the magnitudes of the deviations are between 3.67% and 10.54%. The results corroborate the nondestructive nature of the approach as the predictions are conservative, i.e., below the corresponding buckling loads.

7 Final remarks

In this final chapter, the main achievements of this thesis are discussed in Section 7.1, whereas Section 7.2 provides a critical assessment, and Section 7.3 gives a perspective for future researches.

7.1 Main conclusions

The most prominent contribution of this thesis is the analytical foundation for the empirical VCT published in [35]. In Chapter 4, the anticipated second-order equation between the parametric forms $(1-p)^2$ and $1-f^2$ was demonstrated by rearranging the well-known linear relationship from Equation (4.28). The study also devised a novel VCT definition substantiated on the typical static behavior of an imperfect cylinder, in which the minimum magnitude of $(1-p)^2$ is related to the effective KDF.

These findings were first challenged through a numerical assessment, verifying the second-order relationship despite more realistic boundary conditions, geometric nonlinearities, and initial imperfections. Following this, three experimental campaigns further validated the applicability and robustness of the methodology addressing design details and loading conditions, such as closely spaced stiffeners, internal pressure, realistic R/h, and in-plane induced stresses.

Concerning the second-order equation expressing $(1-p)^2$ in terms of $1-f^2$ and the VCT definition provided in Chapter 4, the following conclusions are drawn:

- Over the methodology from [87], the quadratic nature of the relationship between $(1-p)^2$ and $1-f^2$ permits evaluating an extreme point for estimating ξ^2 instead of relying on the zero natural frequency assumption.
- For the typical static behavior of an unstiffened cylinder in the prebuckling regime, the parametric form of the axially applied load $(1-p)^2$ has a nonlinear variation reaching its minimum magnitude exactly at the buckling load.
- The development of the equations, even though based on a linear theory of shells, improves the understanding of the effectiveness of the methodology conceived empirically in [35].

Regarding the numerical assessment supplied in Chapter 5, the subsequent outcomes are pointed out:

- A nonlinear relationship between $(1-p)^2$ and $1-f^2$, which decreases as the load level increases, is observed in the nonlinear numerical results investigating SS4 boundary conditions and initial mid-surface imperfections.
- The corroborated second-order equation resembles the relationship obtained in the modified characteristic chart; for instance, see Figure 5.16, where the coefficient of determination R_{S}^2 is 1.0000 for all evaluated results.
- The methodology is verified as truly nondestructive even for the study case considering the maximum load level P_{MAX} up to 50% of the corresponding P_{NL}, for which the deviation magnitudes are below 9.9%.
- The estimations obtained increasing the number of load steps and the maximum load level simultaneously are conservative for the entire analyzed range of load levels, i.e., associated with negative deviation magnitudes, see Figure 5.15.
- The algorithm developed based on the MAC index for tracking the vibration modes consists of a reliable tool for fast postprocessing of the results facilitating a thorough evaluation of the variation of the natural frequencies.

As related to experimental campaigns, the applicability and the robustness of the method were notoriously extended as:

- The cylinder Z38 was designed as a simplified downscaled model of a launcher propellant tank [95]; furthermore, internal pressure levels are commonly found in operational conditions.
- The cylinder Z42 was fabricated with an R/h ratio of approximately 1025; moreover, its experimental campaign, including internal pressure and in-plane induced stresses, is closer to real applications.
- The cylinders ZD28 and ZD29 were tested up to 94.85% and 95.74% of their corresponding P_{EXP}, respectively, verifying the second-order relationship in the surroundings of the instability point.
- Different test facilities result in different test conditions; consequently, the experimental campaign presented in Subsection 6.4.2 endorses the robustness of the VCT by testing equivalent specimens in different locations.

All things considered, as introduced in Chapter 1, the aerospace industry would benefit from a reliable nondestructive experimental procedure to predict the buckling load of imperfection-sensitive structures, reducing time and budget spent in projects. In this context, given the nine experimental campaigns [81, 90−97] and the analytical foundation, developed in this thesis and published in [104], the VCT conceived in [35] emerges as a promising method for tackling practical applications.

7.2 Critical assessment

The analytical, numerical, and experimental results of this thesis add substantially to the prospect of the VCT applied to cylindrical shells; nevertheless, the study has some limitations that should be highlighted:

- The analytical verification of $(1-p)^2$ as a quadratic function of $1-f^2$ is deduced from a linearized theory of shells for an unstiffened isotropic cylinder with SS3 boundary conditions. Thus, the assumption that this equation holds for a given structure with initial imperfections, different boundary conditions, and other degrees of anisotropy needs to be verified before the test.
- The numerical evaluation based on two theoretical isotropic cylindrical shells is associated with conservative estimations for the complete range of load levels, *vide* Figure 5.15. Nonetheless, this tendency was not corroborated in the experimental campaign presented in [91], where the authors found non-conservative estimations for one out of three nominally identical specimens.
- The experimental work confirmed that P_{MAX} has more influence on the prediction than the number of load steps and that a P_{MAX} closer to P_{EXP} is needed for experiments associated with a high effective KDF. Accordingly, to plan the VCT experiment, ensuring a nondestructive procedure in the context of imperfection-sensitive structures, remains an open question.

7.3 Future works

On developing the presented research, additional topics that may potentially improve the relevance of the VCT applied to imperfection-sensitive structures were recognized, which are itemized in the following:

- One immediate extension of this thesis would concern the applicability of the methodology. A broader range of realistic design solutions and loading conditions frequently found in aerospace applications could be investigated experimentally and numerically. Among these are other geometries, like conical and double-curved shells; other composite materials, such as sandwich structures; some design details as stiffeners, holes, and complex boundary conditions; and axial load cases combined with bending or external pressure, or both.

- To investigate real-scale barrel structures and to include the VCT in the qualification test of real launch vehicle components are still, to the best of the author's knowledge, unexplored. Such experiments could guide the development of the methodology identifying the barriers that must be overcome to implement the technique in the above-mentioned industrial applications. Besides, experimental data to correlate the available results of sub-scale cylinders to full-scale ones would be provided.

- The analytical work presented in Chapter 4 is based on the linearized Flügge-Lurie-Byrne's shell theory and assumes SS3 boundary conditions. An exploratory research project could tackle both aspects, improving the practicality of the equations. Different boundary conditions would require more complex displacement functions than the ones provided in Equations (4.8) – (4.10). Concerning shell theories, the study could retain different terms, include other phenomena, or eliminate some assumptions.

Appendix A - Publications

The research work performed during the development of this doctoral thesis led to two papers published in conferences:

- Franzoni, F., Arbelo, M. A., and Degenhardt, R., Numerical assessment of existing vibration correlation techniques, in *Proceedings of the 15th European Conference on Spacecraft Structures, Materials and Environmental Testing* (Noordwijk, NL, 2018);
- Franzoni, F., Albus, J., Arbelo, M. A., and Degenhardt, R., Analytical, numerical, and experimental predictions for free vibrations and buckling of pressurized orthotropic cylindrical shells, in *Proceedings of the 69th International Astronautical Congress* (Bremen, DE, 2018);

and three articles published in peer-reviewed scientific journals:

- Franzoni, F., Odermann, F., Wilckens, D., Skuķis, E., Kalniņš, K., Arbelo, M. A., and Degenhardt, R., Assessing the axial buckling load of a pressurized orthotropic cylindrical shell through vibration correlation technique, *Thin-Walled Structures* **137**, 353–366 (2019);
- Franzoni, F., Degenhardt, R., Albus, J., and Arbelo, M. A., Vibration correlation technique for predicting the buckling load of imperfection-sensitive isotropic cylindrical shells: An analytical and numerical verification, *Thin-Walled Structures* **140**, 236–247 (2019);
- Franzoni, F., Odermann, F., Labans, E., Bisagni, C., Arbelo, M. A., and Degenhardt, R., Experimental validation of the vibration correlation technique robustness to predict buckling of unstiffened composite cylindrical shells, *Composite Structures* **224**, 111107 (2019).

References

[1] Hoff, N. J., The Perplexing Behavior of Thin Circular Cylindrical Shells in Axial Compression (AFOSR-66-0155), tech. rep. (Stanford University, Palo Alto, CA, USA, 1966).

[2] Lorenz, R., Achsensymmetrische Verzerrungen in dünnwandigen Hohlzylindern, *Zeitschrift des Vereines Deutscher Ingenieure* **52**(43), 1706–1713 (1908).

[3] Timoshenko, S. P., Einige Stabilitätsprobleme der Elastizitätstheorie, *Zeitschrift für Mathematik und Physik* **58**(4), 337–385 (1910).

[4] Southwell, R. V., V. On the general theory of elastic stability, *Philosophical Transactions of the Royal Society of London. Series A, Containing Papers of a Mathematical or Physical Character* **213**(497-508), 187–244 (1914).

[5] Flügge, W., Die Stabilität der Kreiszylinderschale, *Archive of Applied Mechanics* **3**(5), 463–506 (1932).

[6] Donnell, L. H., A new theory for the buckling of thin cylinders under axial compression and bending, *Transactions of the American Society of Mechanical Engineers* **56**(11), 795–806 (1934).

[7] Koiter, W. T., Over de stabiliteit van het elastisch evenwicht (in Dutch), English translation ''On the Stability of Elastic Equilibrium'' issued as NASA TTF 10833 (1967) and Technical Report AFFDL-TR-70-25 (1970), Ph.D. Thesis (Technische Hooge School at Delft, Delft, NL, 1945).

[8] Hutchinson, J. W. and Koiter, W. T., Postbuckling theory, *Applied Mechanics Reviews* **23**(12), 1353–1366 (1970).

[9] Arbocz, J. and Starnes Jr., J. H., Future directions and challenges in shell stability analysis, *Thin-Walled Structures* **40**, 729–754 (2002).

[10] Elishakoff, I., Probabilistic resolution of the twentieth century conundrum in elastic stability, *Thin-Walled Structures* **59**, 35–57 (2012).

[11] Koiter, W. T., Current trends in the theory of buckling in *Buckling of Structures* (ed. Budiansky, B.), International Union of Theoretical and Applied Mechanics, 1–16 (Springer, Berlin, DE, 1976).

[12] Weingarten, V. I., Seide, P., and Peterson, J. P., Buckling of Thin-Walled Circular Cylinders (NASA SP-8007), tech. rep. (NASA Space Vehicle Design Criteria—Structures, Washington, DC, USA, 1968).

[13] Gerasimidis, S., Virot, E., Hutchinson, J. W., and Rubinstein, S. M., On establishing buckling knockdowns for imperfection-sensitive shell structures, *Journal of Applied Mechanics* **85**(9), 091010 (2018).

[14] Hühne, C., Rolfes, R., Breitbach, E., and Teßmer, J., Robust design of composite cylindrical shells under axial compression—Simulation and validation, *Thin-walled structures* **46**(7-9), 947–962 (2008).

[15] Degenhardt, R., Kling, A., Bethge, A., Orf, J., Kärger, L., Zimmermann, R., Rohwer, K., and Calvi, A., Investigations on imperfection sensitivity and deduction of improved knock-down factors for unstiffened CFRP cylindrical shells, *Composite Structures* **92**(8), 1939–1946 (2010).

[16] Haynie, W. T. and Hilburger, M. W., Comparison of methods to predict lower bound buckling loads of cylinders under axial compression, in *Proceedings of the 51st AIAA/ASME/ASCE/AHS/ASC Structures, Structural Dynamics and Materials Conference* (Orlando, FL, USA, 2010).

[17] Hilburger, M., Developing the next generation shell buckling design factors and technologies, in *Proceedings of the 53rd AIAA/ASME/ASCE/AHS/ASC Structures, Structural Dynamics and Materials Conference* (Honolulu, HI, USA, 2012).

[18] Castro, S. G. P., Zimmermann, R., Arbelo, M. A., Khakimova, R., Hilburger, M. W., and Degenhardt, R., Geometric imperfections and lower-bound methods used to calculate knock-down factors for axially compressed composite cylindrical shells, *Thin-Walled Structures* **74**, 118–132 (2014).

[19] Wagner, H. N. R., Hühne, C., Niemann, S., and Khakimova, R., Robust design criterion for axially loaded cylindrical shells—Simulation and validation, *Thin-Walled Structures* **115**, 154–162 (2017).

[20] Manevich, L. I., Mossakovskii, V. I., and Prokopalo, E. F., Experimental study of the transcritical behaviour of shells, *Mechanics of Solids* **10**(1), 145–150 (1975).

[21] Mossakovskii, V. I., Manevich, L. I., and Evkin, A. Y., Investigation of postbuckling equilibrium forms of a compressed cylindrical shell, *International Applied Mechanics* **11**(11), 1155–1159 (1975).

[22] Horák, J., Lord, G. J., and Peletier, M. A., Cylinder buckling: The mountain pass as an organizing center, *SIAM Journal on Applied Mathematics* **66**(5), 1793–1824 (2006).

[23] Virot, E., Kreilos, T., Schneider, T. M., and Rubinstein, S. M., Stability landscape of shell buckling, *Physical review letters* **119**(22), 224101 (2017).

[24] Hutchinson, J. W. and Thompson, J. M. T., Imperfections and energy barriers in shell buckling, *International Journal of Solids and Structures* **148**, 157–168 (2018).

[25] Groh, R. and Pirrera, A., Localised post-buckling states of axially compressed cylinders and their energy barriers, in *AIAA Science and Technology Forum and Exposition (SciTech)* (San Diego, CA, USA, 2019).

[26] Evkin, A. Y., Local buckling of cylindrical shells. Pogorelov's geometrical method in *Problems of Nonlinear Mechanics and Physics of Materials* (eds. Andrianov, I. V., Manevich, A. I., Mikhlin, Y. V., and Gendelman, O. V.), 369–391 (Springer, Cham, CH, 2019).

[27] Singer, J., The status of experimental buckling investigations of shells in *Buckling of Shells* (ed. Budiansky, B.), 501–533 (Springer, Berlin, DE, 1982).

[28] Singer, J., Arbocz, J., and Weller, T., *Buckling Experiments: Experimental Methods in Buckling of Thin-Walled Structures, Basic Concepts, Columns, Beams and Plates* Vol. 1 (John Wiley & Sons, New York, NY, USA, 2002).

[29] DESICOS, Shell Buckling Knockdown Factor project by NASA. Available: `<https://s.dlr.de/index.php/sbkf-by-nasa>` (Accessed: 07/19/2019).

[30] NASA Has a Crush on You, NASA's Shell Buckling Knockdown Factor (SBKF) project. Available: `<https://www.nasa.gov/topics/technology/features/sbkf.html>` (Accessed: 03/05/2019).

[31] Space in images, ESA's family of launch vehicles. Available: `<https://www.esa.int/spaceinimages/Images>` (Accessed: 02/26/2019).

[32] Singer, J., Arbocz, J., and Weller, T., *Buckling Experiments: Experimental Methods in Buckling of Thin-Walled Structures, Shells, Built-up Structures, Composites and Additional Topics* Vol. 2 (John Wiley & Sons, New York, NY, USA, 2002).

[33] Southwell, R. V., On the analysis of experimental observations in problems of elastic stability, *Proceedings of the Royal Society of London. Series A, Containing Papers of a Mathematical and Physical Character* **135**(828), 601–616 (1932).

[34] Thompson, J. M. T., Hutchinson, J. W., and Sieber, J., Probing shells against buckling: A nondestructive technique for laboratory testing, *International Journal of Bifurcation and Chaos* **27**(14), 1730048 (2017).

[35] Arbelo, M. A., de Almeida, S. F. M., Donadon, M. V., Rett, S. R., Degenhardt, R., Castro, S. G. P., Kalnins, K., and Ozoliņš, O., Vibration correlation technique for the estimation of real boundary conditions and buckling load of unstiffened plates and cylindrical shells, *Thin-Walled Structures* **79**, 119–128 (2014).

[36] Sommerfeld, A., Eine einfache Vorrichtung zur Veranschaulichung des Knickungsvorganges, *Zeitschrift des Vereines Deutscher Ingenieure* **49**, 1320–1323 (1905).

[37] Massonnet, C. E., *Les Relations entre les Modes Normaux de Vibration et la Stabilité des Systèmes Élastiques* (Goemaere, Brussels, BE, 1940).

[38] Massonnet, C. E., Le voilement des plaques planes sollicitées dans leur plan, in *Final Report of the 3rd Congress of the International Association for Bridge and Structural Engineering* (Brussels, BE, 1948).

[39] Lurie, H., Lateral Vibrations as Related to Structural Stability, Ph.D. Thesis (California Institute of Technology, Pasadena, CA, USA, 1950).

[40] Virgin, L. N., *Vibration of Axially-Loaded Structures* (Cambridge University Press, Cambridge, UK, 2007).

[41] Franzoni, F., de Almeida, S. F. M., and Ferreira, C. A. E., Numerical and experimental dynamic analyses of a post-buckled box-beam, *AIAA Journal* **54**(6), 1987–2003 (2016).

[42] Abramovich, H., *Stability and Vibrations of Thin-Walled Composite Structures* (Woodhead Publishing, Sawston, Cambridge, UK, 2017).

[43] Thompson, J. M. T., Advances in shell buckling: Theory and experiments, *International Journal of Bifurcation and Chaos* **25**(01), 1530001 (2015).

[44] Singer, J. and Abramovich, H., Vibration techniques for definition of practical boundary conditions in stiffened shells, *AIAA Journal* **17**(7), 762–769 (1979).

[45] Fan, H., Critical buckling load prediction of axially compressed cylindrical shell based on non-destructive probing method, *Thin-Walled Structures* **139**, 91–104 (2019).

[46] Franzoni, F., Arbelo, M. A., and Degenhardt, R., Numerical assessment of existing vibration correlation techniques, in *Proceedings of the 15th European Conference on Spacecraft Structures, Materials and Environmental Testing* (Noordwijk, NL, 2018).

[47] von Kármán, T., Untersuchungen über Knickfestigkeit in *Mitteilungen über Forschungsarbeiten* (ed. Verein Deutscher Ingenieure), auf dem Gebiet des Ingenieurwesens insbesondere aus den Laboratorien der Technischen Hochschulen Vol. 81, 1–44 (Springer, Berlin, DE, 1910).

[48] Donnell, L. H., On the application of Southwell's method for the analysis of buckling tests in *Stephan Timoshenko 60th Anniversary Volume* 27–38 (The Macmillan Company, New York, USA, 1938).

[49] Fisher, H. R., An extension of Southwell's method of analyzing experimental observations in problems of elastic stability, *Proceedings of the Royal Society of London. Series A, Containing Papers of a Mathematical and Physical Character* **144**, 609–630 (1934).

[50] Ramberg, W., McPherson, A. E., and Levy, S., Experimental Study of Deformation and of Effective Width in Axially Loaded Sheet-Stringer Panels (NACA TN-684), tech. rep. (National Advisory Committee for Aeronautics, Washington, DC, USA, 1939).

[51] Lundquist, E. E., Generalized Analysis of Experimental Observations in Problems of Elastic Stability (NACA TN-658), tech. rep. (National Advisory Committee for Aeronautics, Washington, DC, USA, 1938).

[52] Tsai, W. T., Note on Southwell's method for buckling tests of struts, *Journal of Applied Mechanics* **53**, 953–954 (1986).

[53] Singer, J., On the applicability of the Southwell plot to plastic buckling, *Experimental Mechanics* **29**(2), 205–208 (1989).

[54] Wang, C., Inelastic column theories and an analysis of experimental observations, *Journal of the Aeronautical Sciences* **15**(5), 283–292 (1948).

[55] Stratford, T. J., Burgoyne, C. J., and Taylor, H. P. J., Stability design of long precast concrete beams, *Proceedings of the Institution of Civil Engineers: Structures and Buildings* **134**(2), 159–168 (1999).

[56] Stratford, T. J. and Burgoyne, C. J., Lateral stability of long precast concrete beams, *Proceedings of the Institution of Civil Engineers: Structures and Buildings* **134**(2), 169–180 (1999).

[57] Mandal, P. and Calladine, C. R., Lateral-torsional buckling of beams and the Southwell plot, *International Journal of Mechanical Sciences* **44**(12), 2557–2571 (2002).

[58] Walker, A. C., Local instability in plates and channel struts, *Journal of the Structural Division* **92**(3), 39–56 (1966).

[59] Horton, W. H., Cundari, F. L., and Johnson, R. W., The analysis of experimental data obtained from stability studies on elastic column and plate structures, *Israel Journal of Technology* **5**(1–2), 104–113 (1967).

[60] Datta, P. K. and Carlson, R. L., Buckling and vibration of a thin tensioned sheet with an elliptical hole, *Experimental Mechanics* **13**(7), 280–286 (1973).

[61] Spencer, H. H. and Walker, A. C., Critique of Southwell plots with proposals for alternative methods, *Experimental Mechanics* **15**(8), 303–310 (1975).

[62] Datta, P. K., Static stability behaviour of plate elements with non-uniform, in-plane stress distribution, *Journal of Mechanical Engineering Science* **21**(5), 363–365 (1979).

[63] Weller, T., Singer, J., and Nachmani, S., Recent Experimental Studies on the Buckling of Stringer-Stiffened Cylindrical Shells (Eng. Report TAE No 100), tech. rep. (Israel Institute of Technology, Haifa, IL, 1970).

[64] Weller, T. and Singer, J., Experimental studies on buckling of ring-stiffened conical shells under axial compression, *Experimental Mechanics* **10**(11), 449–457 (1970).

[65] Wang, L. R. L., Rodriquez-Agrait, L., and Little, W. A., Effect of boundary conditions on shell buckling, *Journal of the Engineering Mechanics Division* **92**(6), 101–116 (1966).

[66] Craig, J. I. and Duggan, M. F., Nondestructive shell-stability estimation by a combined-loading technique, *Experimental Mechanics* **13**(9), 381–388 (1973).

[67] Horton, W. H., Nassar, E. M., and Singhal, M. K., Determination of the critical loads of shells by nondestructive methods, *Experimental Mechanics* **17**(4), 154–160 (1977).

[68] Ghazijahani, T. G. and Zirakian, T., Determination of buckling loads of conical shells using extrapolation techniques, *Thin-Walled Structures* **74**, 292–299 (2014).

[69] Chu, T. H., Determination of Buckling Loads by Frequency Measurements, Ph.D. Thesis (California Institute of Technology, Pasadena, CA, USA, 1949).

[70] Lurie, H., Effective end restraint of columns by frequency measurements, *Journal of the Aeronautical Sciences* **18**(8), 566–567 (1951).

[71] Lurie, H., Lateral vibrations as related to structural stability, *Journal of Applied Mechanics* **19**(2), 195–204 (1952).

[72] Galef, A. E., Bending frequencies of compressed beams, *The Journal of the Acoustical Society of America* **44**(2), 643–643 (1968).

[73] Johnson, E. E. and Goldhammer, B. F., The determination of the critical load of a column or stiffened panel in compression by the vibration method, *Proceedings of the Society for Experimental Stress Analysis* **11**(1), 221–232 (1953).

[74] Burgreen, D., End-fixity effect on vibration and instability, *Journal of the Engineering Mechanics Division* **86**(6), 13–28 (1960).

[75] Jacobson, M. J. and Wenner, M. L., Predicting buckling loads from vibration data, *Experimental Mechanics* **8**(10), 35N–38N (1968).

[76] Chailleux, A., Hans, Y., and Verchery, G., Experimental study of the buckling of laminated composite columns and plates, *International Journal of Mechanical Sciences* **17**(8), 489–498 (1975).

[77] Jubb, J. E. M., Phillips, I. G., and Becker, H., Interrelation of structural stability, stiffness, residual stress and natural frequency, *Journal of Sound and Vibration* **39**(1), 121–134 (1975).

[78] Mandal, P., Prediction of buckling load from vibration measurements in *New Approaches to Structural Mechanics, Shells and Biological Structures* (eds. Drew, H. and Pellegrino, S.), Solid Mechanics and Its Applications Vol. 104, 175–188 (Springer, Dordrecht, NL, 2002).

[79] Chaves-Vargas, M., Dafnis, A., Reimerdes, H.-G., and Schröder, K.-U., Modal parameter identification of a compression-loaded CFRP stiffened plate and correlation with its buckling behaviour, *Progress in Aerospace Sciences* **78**, 39–49 (2015).

[80] Kennedy, D. and Lo, K. I., Critical buckling predictions for plates and stiffened panels from natural frequency measurements, *Journal of Physics: Conference Series* **1106**, 012018 (2018).

[81] Shahgholian-Ghahfarokhi, D., Aghaei-Ruzbahani, M., and Rahimi, G., Vibration correlation technique for the buckling load prediction of composite sandwich plates with iso-grid cores, *Thin-Walled Structures* **142**, 392–404 (2019).

[82] Abramovich, H., Govich, D., and Grunwald, A., Buckling prediction of panels using the vibration correlation technique, *Progress in Aerospace Sciences* **78**, 62–73 (2015).

[83] Okubo, S. and Whittier, J. S., A note on buckling and vibrations of an externally pressurized shallow spherical shell, *Journal of Applied Mechanics* **34**(4), 1032–1034 (1967).

[84] Radhakrishnan, R., Prediction of buckling strengths of cylindrical shells from their natural frequencies, *Earthquake Engineering & Structural Dynamics* **2**(2), 107–115 (1973).

[85] Segal, Y., Prediction of Buckling Load and Loading Conditions of Stiffened Shells from Vibration Tests, M.Sc. Thesis (Israel Institute of Technology, Haifa, IL, 1980).

[86] Plaut, R. H. and Virgin, L. N., Use of frequency data to predict buckling, *Journal of engineering mechanics* **116**(10), 2330–2335 (1990).

[87] Souza, M. A., Fok, W. C., and Walker, A. C., Review of experimental techniques for thin-walled structures liable to buckling: neutral and unstable buckling, *Experimental Techniques* **7**(9), 21–25 (1983).

[88] Souza, M. A. and Assaid, L. M. B., A new technique for the prediction of buckling loads from nondestructive vibration tests, *Experimental Mechanics* **31**(2), 93–97 (1991).

[89] Singer, J., Buckling Experiments on Shells: A Review of Recent Developments (Eng. Report TAE No 403), tech. rep. (Israel Institute of Technology, Haifa, IL, 1980).

[90] Kalnins, K., Arbelo, M. A., Ozolins, O., Skukis, E., Castro, S. G. P., and Degenhardt, R., Experimental nondestructive test for estimation of buckling load on unstiffened cylindrical shells using vibration correlation technique, *Shock and Vibration* **2015**, 1–8 (2015).

[91] Arbelo, M. A., Kalnins, K., Ozolins, O., Skukis, E., Castro, S. G. P., and Degenhardt, R., Experimental and numerical estimation of buckling load on unstiffened cylindrical shells using a vibration correlation technique, *Thin-Walled Structures* **94**, 273–279 (2015).

[92] Skukis, E., Ozolins, O., Kalnins, K., and Arbelo, M. A., Experimental test for estimation of buckling load on unstiffened cylindrical shells by vibration correlation technique, *Procedia Engineering* **172**, 1023–1030 (2017).

[93] Skukis, E., Ozolins, O., Andersons, J., Kalnins, K., and Arbelo, M. A., Applicability of the vibration correlation technique for estimation of the buckling load in axial compression of cylindrical isotropic shells with and without circular cutouts, *Shock and Vibration* **2017**, 1–14 (2017).

[94] Shahgholian-Ghahfarokhi, D. and Rahimi, G., Buckling load prediction of grid-stiffened composite cylindrical shells using the vibration correlation technique, *Composites Science and Technology* **167**, 470–481 (2018).

[95] Franzoni, F., Odermann, F., Wilckens, D., Skuķis, E., Kalniņš, K., Arbelo, M. A., and Degenhardt, R., Assessing the axial buckling load of a pressurized orthotropic cylindrical shell through vibration correlation technique, *Thin-Walled Structures* **137**, 353–366 (2019).

[96] Labans, E., Abramovich, H., and Bisagni, C., An experimental vibration-buckling investigation on classical and variable angle tow composite shells under axial compression, *Journal of Sound and Vibration* **449**, 315–329 (2019).

[97] Franzoni, F., Odermann, F., Labans, E., Bisagni, C., Arbelo, M. A., and Degenhardt, R., Experimental validation of the vibration correlation technique robustness to predict buckling of unstiffened composite cylindrical shells, *Composite Structures* **224**, 111107 (2019).

[98] Evkin, A. Y., Krasovskii, V. L., and Manevich, L. I., Stability of longitudinally compressed cylindrical shells under quasi-static local disturbances, *Mechanics of Solids* **13**(6), 83–88 (1978).

[99] Evkin, A. Y. and Krasovskii, V. K., Post-critical deformation and estimation of the stability of real cylindrical shells under external pressure, *International Applied Mechanics* **27**(3), 290–296 (1991).

[100] Evkin, A. Y. and Lykhachova, O. V., Energy barrier as a criterion for stability estimation of spherical shell under uniform external pressure, *International Journal of Solids and Structures* **118-119**, 14–23 (2017).

[101] Evkin, A., Dynamic energy barrier estimation for spherical shells under external pressure, *International Journal of Mechanical Sciences* **160**, 51–58 (2019).

[102] Evkin, A., Krasovsky, V., Lykhachova, O., and Marchenko, V., Local buckling of axially compressed cylindrical shells with different boundary conditions, *Thin-Walled Structures* **141**, 374–388 (2019).

[103] Franzoni, F., Albus, J., Arbelo, M. A., and Degenhardt, R., Analytical, numerical, and experimental predictions for free vibrations and buckling of pressurized orthotropic cylindrical shells, in *Proceedings of the 69th International Astronautical Congress* (Bremen, DE, 2018).

[104] Franzoni, F., Degenhardt, R., Albus, J., and Arbelo, M. A., Vibration correlation technique for predicting the buckling load of imperfection-sensitive isotropic cylindrical shells: An analytical and numerical verification, *Thin-Walled Structures* **140**, 236–247 (2019).

[105] Leissa, A. W., Vibration of Shells (NASA SP-288), tech. rep. (US Government Printing Office, Washington, DC, USA, 1973).

[106] Amabili, M., *Nonlinear Vibrations and Stability of Shells and Plates* (Cambridge University Press, Cambridge, UK, 2008).

[107] William J. Hughes Technical Center, *MMPDS-07: Metallic Materials Properties Development and Standardization (MMPDS),* (Federal Aviation Administration, Washington, DC, USA, 2012).

[108] Lozano, E., Burau, F., Reichardt, J., Schor, P., and Castro, S. G. P., DESICOS Improved Sofware. Available: `<http://desicos.github.io/desicos/index.html>` (Accessed: 05/05/2019).

[109] LMS International, The LMS Theory and Background Book, tech. rep. (Leuven, BE, 2000).

[110] Zimmermann, R., Buckling research for imperfection tolerant fiber composite structures, in *Proceedings of the International Conference on Spacecraft Structures, Materials and Mechanical Testing* (Noordwijk, NL, 1996).

[111] Bisagni, C., Vescovini, R., and Dávila, C. G., Single-stringer compression specimen for the assessment of damage tolerance of postbuckled structures, *Journal of Aircraft* **48**(2), 495–502 (2011).

[112] Bisagni, C., Composite cylindrical shells under static and dynamic axial loading: An experimental campaign, *Progress in Aerospace Sciences* **78**, 107–115 (2015).

[113] Hühn, D., Versagensprognose von Faser-Kunststoff-Verbunden basierend auf einer Mehrskalenbetrachtung (in German), Ph.D. Thesis (Universität Dresden, Dresden, DE, 2016).

[114] Daniel, I. M. and Ishai, O., *Engineering Mechanics of Composite Materials* (Oxford University Press, New York, NY, USA, 2006).

[115] Khakimova, R., Wilckens, D., Reichardt, J., Zimmermann, R., and Degenhardt, R., Buckling of axially compressed CFRP truncated cones: Experimental and numerical investigation, *Composite Structures* **146**, 232–247 (2016).

[116] Hexcel Composites, *HexPly® 8552 Product Data* (2013).

[117] Wilckens, D., Buckling tests on unstiffened cylindrical shells (ITOBUCK WP 3), tech. rep. (Deutsches Zentrum für Luft- und Raumfahrt, Braunschweig, DE, 2020).

[118] North Thin Ply Technology, *ThinPreg™ 135 Data Sheet* (2017).

[119] Zimmermann, R., Klein, H., and Kling, A., Buckling and postbuckling of stringer stiffened fibre composite curved panels — Tests and computations, *Composite Structures* **73**, 150–161 (2006).

[120] Degenhardt, R., Kling, A., Klein, H., Hillger, W., Goetting, H. C., Zimmermann, R., Rohwer, K., and Gleiter, A., Experiments on buckling and postbuckling of thin-walled CFRP structures using advanced measurement systems, *International Journal of Structural Stability and Dynamics* **7**(02), 337–358 (2007).

[121] Wilckens, D., Odermann, F., and Kling, A., Buckling and post buckling of stiffened CFRP panels under compression and shear-test and numerical analysis, in *Proceedings of the 54th AIAA/ASME/ASCE/AHS/ASC Structures, Structural Dynamics, and Materials Conference* (Boston, MA, USA, 2013).